공학박사 학위논문

Application of mesenchymal stem cells as a tumor-targeting carrier of gold nanoparticles in photothermal cancer therapy

광열 암 치료에서 금 나노입자의 종양 표적 전달체로서 중간엽 줄기세포의 응용

2017 년 8 월

서울대학교 대학원
화학생물공학부
강 서 경

Abstract

Application of mesenchymal stem cells as a tumor-targeting carrier of gold nanoparticles in photothermal cancer therapy

Seokyung Kang

School of Chemical and Biological Engineering

The Graduate School

Seoul National University

Cancer is a major health problem and a leading cause of death worldwide. As nanotechnology has made remarkable progress, nanoparticle-based cancer therapies have been extensively studied. Recently, photothermal cancer therapy has emerged as a new strategy for cancer treatment. Among the photothermal agents, gold nanoparticles (AuNPs) have drawn much attention for their application in photothermal therapy because AuNPs exhibit the high light-to-heat conversion efficiency upon near-infrared (NIR) laser irradiation. However, it remains

challenging to improve the tumor-targeting efficiency of AuNPs for the effective photothermal treatment. In this thesis, the application of tumor-tropic mesenchymal stem cells (MSCs) as a carrier for tumor-targeted delivery of AuNPs in photothermal therapy are presented.

First, pH-sensitive gold nanoparticles (PSAuNPs) were delivered to tumors by internalized in MSCs. Tumor-tropic MSCs can aggregate PSAuNPs in mildly acidic endosomes, target tumors, and be used for photothermal therapy. The aggregated PSAuNPs showed a higher cellular retention by preventing exocytosis compared to pH-insensitive, control AuNPs (cAuNPs), which is important for the cell-based delivery process. PSAuNP-laden MSCs (MSC-PSAuNPs) injected intravenously to tumor-bearing mice showed higher efficiency in tumor-targeting and heat generation compared to injections of cAuNPs after irradiation, which results in a significantly enhanced anti-cancer effect.

Second, hybrid sheets composed of AuNPs and graphene oxide (GO) were delivered to tumor tissues by attached to the MSC surface. There are limitations in loading nanoparticles within cells as the internalized nanoparticles cause cytotoxicity and leak out of the cells *via* exocytosis. Therefore, we introduced AuNP/GO sheets which stably adhere to the cell surface and exhibit remarkable photothermal effect. To form AuNP/GO sheets in which GO is sandwiched between two AuNP monolayers, AuNPs were coated with α-synuclein protein and subsequently adsorbed onto GO sheets. Attaching AuNP/GO sheets to tumor-tropic MSC surface enhanced the loading efficiency of AuNPs in MSCs by avoiding the cytotoxicity and exocytosis issues. Furthermore, the tight packing of AuNPs on micro-scaled GO sheets enhanced the photothermal effect *via* strong plasmon coupling between AuNPs. The injection of AuNP/GO sheet-attached MSCs into tumor-bearing mice significantly improved the photothermal

therapeutic efficacy by delivering larger amounts of AuNPs to the tumor and generating higher heat at tumor region compared to injection of AuNP-internalized MSCs.

The cellular Trojan horse strategy may be an effective platform for delivering anti-cancer agents to tumors. Furthermore, therapeutic effect can be maximized through the interaction between materials and cells. This material- and cell-based anti-cancer therapy may be used in the future for successful cancer treatments.

Keywords: gold nanoparticles, mesenchymal stem cells, photothermal therapy, tumor targeting, tumor tropism

Student Number: 2014-30251

Table of Contents

List of Figures

Abbreviations

AFM	atomic force microscope
AuNP	gold nanoparticle
BSA	bovine serum albumin
cAuNP	pH-insensitive, control gold nanoparticle
CCK-8	cell counting kit-8
CT	computer tomography
DAPI	4',6-diamidino-2-phenylindole
DLS	dynamic light scattering
DW	distilled water
EB	ethidium bromide
EDTA	ethylenediaminetetraacetic acid
EPR	enhanced permeability and retention
FDA	fluorescein diacetate
GO	graphene oxide
ICP-MS	inductively coupled plasma-mass spectrometry
ID	injected dose
IGF	insulin-like growth factor
IL	interleukin
LDH	lactate dehydrogenase
MES	2-(N-morpholino)ethanesulfonic acid
MSC	mesenchymal stem cell
MUA	11-mercaptoundecanoic acid

NIR	near-infrared
NSC	neural stem cell
PBS	phosphate buffered saline
PCNA	proliferating cell nuclear antigen
PDGF	platelet-derived growth factor
PSAuNP	pH-sensitive gold nanoparticle
qRT-PCR	quantitative real-time polymerase chain reaction
SDF	stromal cell-derived factor
SEM	scanning electron microscope
SPION	superparamagnetic iron oxide nanoparticle
SPR	surface plasmon resonance
TEM	transmission electron microscopy
UV	ultraviolet
VEGF	vascular endothelial growth factor
ATPase	adenosinetriphosphatase
Arg	arginine
Gly	glycine
Asp	aspartic acid
Asn	asparagine
CTLA-4	cytotoxic T-lymphocyte-associated protein 4
PD-1	programmed cell death protein 1
PD-L1	programmed death-ligand 1

Chapter 1.

Research background and objectives

1.1. Photothermal cancer therapy

Plasmonic photothermal therapy is a spatiotemporally controllable heat shock strategy for cancer treatment.[1] The localized heat is generated by photothermal agents, such as gold nanoparticles (AuNPs), reduced graphene oxide, and carbon nanotube, that can convert light to heat.[2] Among various light sources, near-infrared (NIR) light is generally used as an energy source due to its tissue penetrating capability. NIR light can reach deep tissues because hemoglobin and water minimally absorb the light at NIR wavelengths.[3] In photothermal treatment, tumor tissues are exposed to hyperthermia and undergo irreversible cell-damage depending on the magnitude of the temperature and the exposure time (Figure 1.1). Conventional hyperthermia (43 – 48 °C) treatment increases the rate of biochemical reactions, which induces the generation of reactive oxygen species. This oxidative stress gradually leads to the destruction of plasma membranes, proteins, and nucleic acid.[2,4] For direct cell necrosis, long-term exposures (> 60 min) to temperatures in this range are required.[2,5] On the other hand, temperatures above 48 °C instantaneously cause irreversible protein coagulation and DNA damage that lead to cell death even for short exposure times (4 – 6 min).[2]

The photothermal ablation approach has several advantages over chemotherapy and surgical resection, such as spatiotemporal controllability, minimal invasiveness, and independence of tumor type.[6] The localized irradiation of NIR laser at low intensity facilitates high heat generation in the tumor region with minimal damage in the surrounding normal tissues.[7] In addition, all cancerous cells including radioresistant and chemoresistant cells can be treated with photothermal therapy.[6,8]

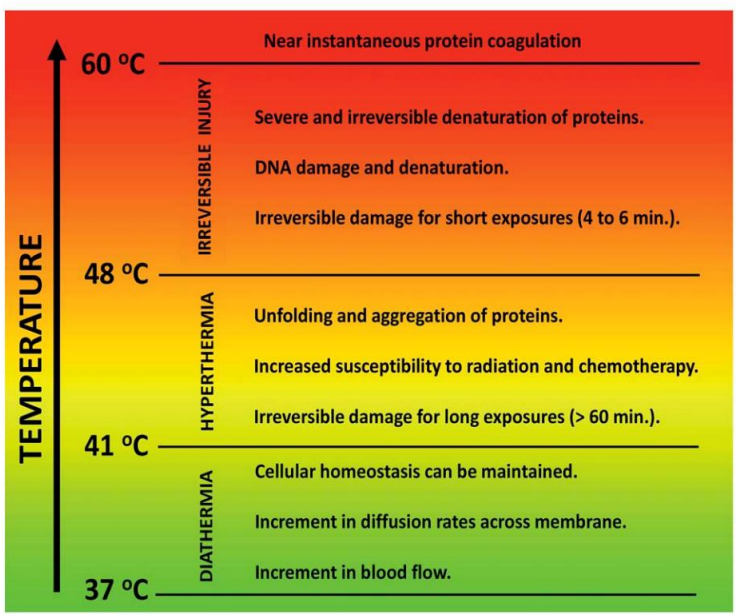

Figure 1.1. Schematic diagram presenting the effects of various thermal treatment as classified by temperature ranges on cells[2]

1.2. Gold nanoparticles as a photothermal agent

The therapeutic efficacy of photothermal therapy depends on the light-to-heat conversion capability of photothermal agents. AuNPs have been extensively studied as photothermal agents for cancer therapy due to their superior photophysical properties.[9-12] Gold nanostructures efficiently generate heat by absorbing the extrinsic light energy at the plasmonic resonant wavelength. More specifically, when electromagnetic radiation of an appropriate wavelength is irradiated to AuNPs, the electrons on AuNP surface are collectively oscillated and cause a surface plasmon resonance (SPR) (Figure 1.2).[13-15] In this phenomenon, there are two types of interactions: scattering and absorption. Some of the incoming light is scattered in all directions at the same wavelength. The absorbed energy is released by the emission of phonons, which typically generates heat.[2,13] The AuNPs strongly absorb light energy at plasmonic resonant wavelength and effectively generate heat *via* light-to-heat conversion.

The photothermal properties of gold nanostructures depend on their shape and size.[16-17] The SPR frequency of spherical AuNPs broadens and shifts into the NIR window when the diameter of AuNPs increases.[17-18] Furthermore, assembling or clustering of spherical AuNPs red-shifts the absorption spectrum *via* plasmon coupling between adjacent AuNPs.[11] Meanwhile, the absorption spectrum of gold nanorods varies with the aspect ratio. When the aspect ratio of gold nanorods is increased, the SPR wavelength is significantly red-shifted.[17] The optical resonance of gold nanoshells, which consist of a silica core nanoparticle and a thin outer layer of gold nanoparticles, varies with the ratio of the thickness of gold layer to the diameter of silica core. When this ratio is decreased, the absorption spectrum is shifted into NIR region.[17]

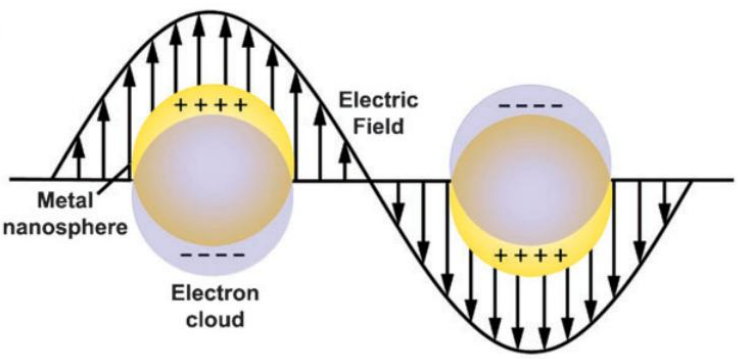

Figure 1.2. Surface plasmon resonance (SPR) effect of AuNPs, resulted from the collective oscillation of delocalized electron upon laser irradiation[13]

1.3. Nanoparticle delivery to tumors

Photothermal therapeutic efficacy depends on the tumor-targeting efficiency of photothermal agents as well as the photothermal property upon NIR laser irradiation. The systemically administered nanoparticles are severely accumulated in the reticuloendothelial (spleen and liver) and renal (kidney) systems. The phagocytic cells in reticuloendothelial system actively take up the nanoparticles.[19-20] The renal system, meanwhile, excretes nanoparticles smaller than the kidney filtration threshold (5.5 nm).[19-21] The nanoparticles that deviate from those biological barriers have the opportunity to reach the tumor tissues and can be delivered into tumors *via* passive and active targeting mechanisms.[22]

In passive targeting, nanoparticles cross the tumor vascular barrier through intercellular gaps and remain in the tumor region due to interstitial pressure generated by poor lymphatic drainage. This process is termed enhanced permeability and retention (EPR) effect (Figure 1.3). The tumor vessels show abnormal hyperpermeability, which is attributed to their incomplete structure such as a monolayer of endothelial cells without pericyte coverage and disrupted basement membranes.[23-26] Furthermore, the endothelial cells of the tumor vasculature less tightly adhere to each other and form intercellular gaps of 100 nm – 2 μm.[27-28] Therefore, nanoparticles smaller than the size of these gaps are extravasated and passively transported into the tumor microenvironment.

In active targeting, the surface of nanoparticle is functionalized with targeting moieties that complementarily interact with the target sites such as peritumoral blood vessels, tumor cells, and tumor microenvironment.[22,29-34] The specific targeting is regarded as a promising strategy for improving tumor-targeting effect of anti-cancer agents. Some previous studies, however, demonstrated that the

targeting ligands have no effect on tumor localization of nanoparticles, but enhance their internalization into target cells *via* receptor-mediated endocytosis.[35-36]

A previous study has surveyed the papers regarding tumor-targeted delivery of nanoparticles from the past 10 years, statistically revealing that only 0.7 % of the injected nanoparticle dose (ID) is delivered into solid tumors.[22] Specifically, delivery efficiencies of passive and active targeting strategies are 0.6 and 0.9 %ID, respectively. The extremely low tumor-targeting efficiency of intravenously administered gold nanostructures in tumor-bearing animals still remains a challenge.

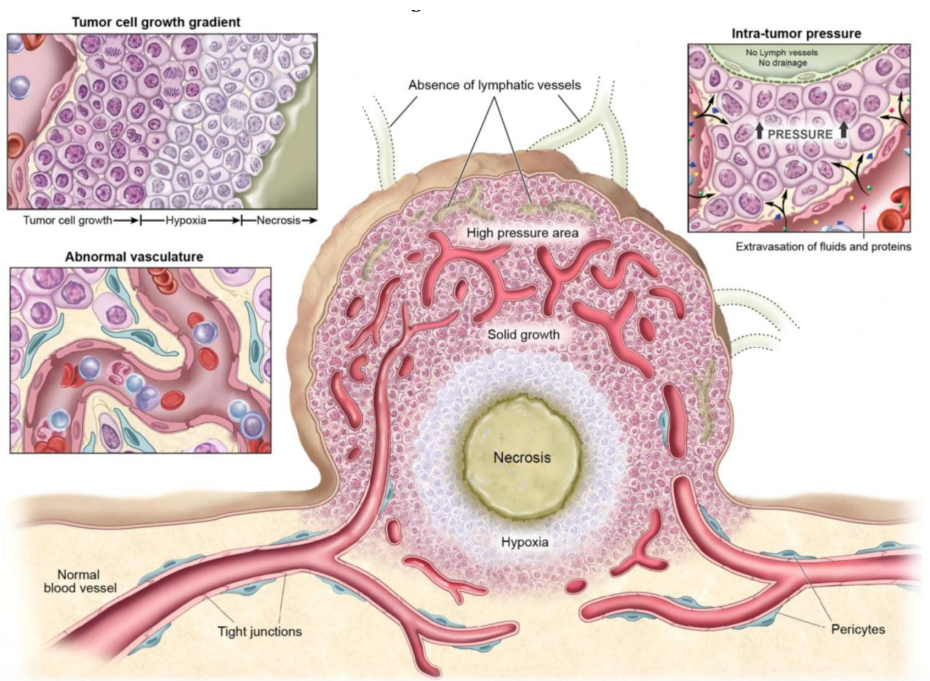

1.3. Characteristics of tumor tissue and vasculatures that affect tumor-targeting effect of nanoparticles[24]

1.4. Tumor-tropism of mesenchymal stem cells

Tumor-tropic cell-mediated nanoparticle delivery has been investigated to improve the tumor-targeting efficiency of anti-cancer nanostructures. Tumor-tropic cells including macrophages,[37-39] neural stem cells (NSCs),[40] and mesenchymal stem cells (MSCs)[41] actively migrate into tumor regions *via* a paracrine signaling loop between tumor tissues and tumor-tropic cells. The tumor tropism of those cells involves interactions between the chemokines released from tumor tissues and the chemokine receptors expressed on the surfaces of tumor-tropic cells. Tumor-secreted factors enhance the expression of CXC and CC receptors in a positive-feedback manner and activate growth factor receptors or toll-like receptors of cells.[42-46] The tumor-tropic cells then become more sensitized to chemoattractants, including CCL2,[42] CXCL8,[43] RANTES (CCL5),[44] platelet-derived growth factor (PDGF)-bb,[45] insulin-like growth factor (IGF)-1,[44] and vascular endothelial growth factor (VEGF)[46], which are released from tumor tissues.

Macrophages loaded with gold nanoshells migrated within glioma spheroids *in vitro* and generated heat upon laser irradiation.[37-38] Tumor-tropic properties of macrophages were demonstrated in a brain tumor-bearing mouse model.[39] Gold nanoshell-laden macrophages migrated into brain tumors by traversing the blood-brain barrier.[39] Intratumoral injection of gold nanorod-loaded NSCs improved the intratumoral distribution of the nanorods and consequently enhanced the photothermal therapeutic efficacy.[40] The tumor-tropic properties of MSCs that incorporated mesoporous silica nanoparticles were demonstrated *via in vivo* multimodal imaging.[41] Among aforementioned tumor-tropic cells, MSCs have several distinct features. MSCs preferentially migrate to tumor regions regardless of the tumor type.[47-49] Furthermore, MSCs can be easily isolated from the patients

and extensively expanded *in vitro*.[50] MSCs also exhibit minimal immunogenicity and even immunosuppressive property upon transplantation.[50-51] Therefore, nanoparticle-laden MSCs can serve as a stealth vehicle to deliver nanoparticles to tumors, as they can avoid the surveillance of immune cells to safely arrive at the target tumor tissues.

1.5. Cell-nanoparticle interactions

When nanoparticles are incubated with cells, the particles first meet the plasma membrane of cells and are internalized into cells *via* endocytosis process (Figure 1.4).[52-53] Some of the endocytosed nanoparticles escape from cells *via* exocytosis process (Figure 1.4).[53] Cellular responses to nanoscale-materials depend on both physicochemical properties of materials and cell types.[53-57] The size and shape of nanostructures have effect on the efficiency of endocytosis and exocytosis. Furthermore, the materials rarely taken up by nonphagocytic cells can be internalized into phagocytic cells. The cell-nanoparticle interactions depending on material properties and cell types are discussed in the following.

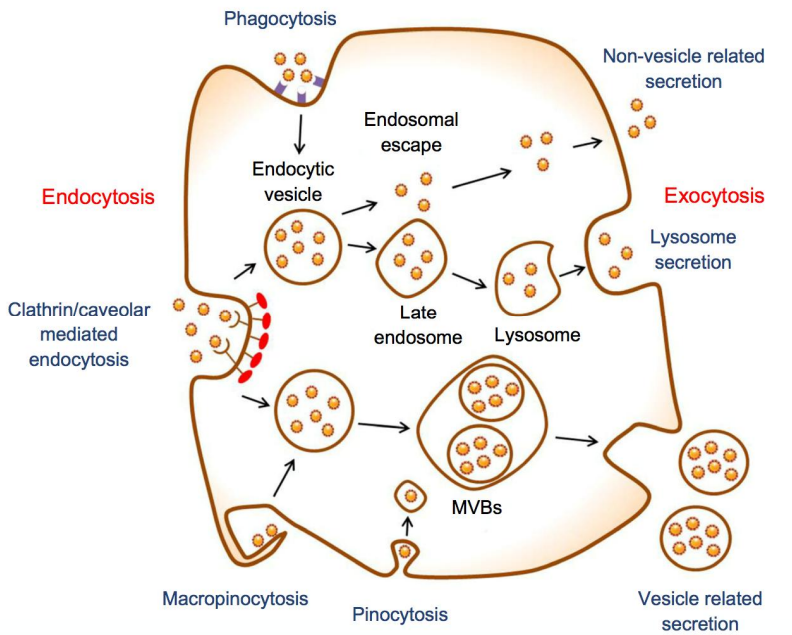

Figure 1.4. Schematic illustration of endocytosis and exocytosis of nanoparticles.[53] MVBs mean multivesicular bodies.

1.5.1. Nanoparticle endocytosis

Cells actively transport signaling molecules into cells *via* endocytosis process to communicate with biological environments. This endocytosis process is an energy-using process and typically classified into receptor-mediated endocytosis, phagocytosis, and macropinocytosis.[52-53,58] The receptor-mediated endocytosis is subdivided into clathrin- and caveolae-mediated endocytosis, in which clathrin and caveolae are a cytosolic protein and a type of lipid raft containing caveloin protein, respectively.[59] The receptor-mediated endocytosis pathways are important for the internalization of nanoparticles into cells.[53] When the nanoparticles are exposed to biological fluid including serum-containing medium and plasma, the proteins are adsorbed to the surface of nanoparticles and interact with the membrane receptors.[53] The receptor-ligand complexes are then incorporated into intracellular transport vesicles. The phagocytosis is an actin-dependent pathway and restricted to phagocytic cells such as macrophages, dendritic cells, and neutrophils.[60] These phagocytic cells take up materials larger than 0.5 μm in size *via* phagocytosis. The macropinocytosis is a non-specific process, by which cells internalize both biological fluids and particles into the cells.[61]

Previous studies demonstrated that endocytosis efficiency of nanoparticles highly depends on their physicochemical properties such as size and shape. For spherical AuNPs, the 50 nm nanoparticles entered cells more efficiently than AuNPs with diameters of 14 nm and 74 nm *via* the receptor-mediated endocytosis pathway.[54] The rod-shaped AuNPs, meanwhile, were more dependent on the width of the nanoparticles than the length.[55] Interestingly, the rod-shaped AuNPs exhibited lower uptake efficiency compared to the counterpart spherical AuNPs. For example, the cells internalized 5.0- and 3.7-fold larger amount of 74 nm and 14

nm spherical AuNPs than 74 × 14 nm rod-shaped AuNPs, respectively.[54] Graphene oxide (GO), a two-dimensional nanosheet, shows unique cell-nanoparticle interactions depending upon their lateral dimensions.[57,62] Whereas nano-sized GO (20 – 500 nm) was internalized into cells,[57] the micro-scaled GO flakes (1 – 6 μm) were rarely incorporated into cells, but rather anchored on the cell surface.[62]

1.5.2. Nanoparticle exocytosis

Endocytosed nanoparticles can escape from cells *via* exocytosis process. There are three types of exocytosis pathway: lysosome secretion, vesicle-related secretion, and non-vesicle-related secretion.[63] A previous study showed a series of exocytosis process of transferrin-coated AuNPs using transmission electron microscopy (TEM).[55] The transferrin-coated AuNPs were internalized into cells *via* receptor-mediated endocytosis and then localized in lysosomes and late endosomes before exocytosis.[55] The vesicles containing nanoparticles moved toward the cell membrane, eventually docked, and released the contents by fusing with the plasma membrane.[55]

The exocytosis is dependent on the size of nanoparticles. The amount and rate of nanoparticle exocytosis appear to increase as nanoparticle size decreases.[53,55,64-66] For example, the amount of exocytosed superparamagnetic iron oxide nanoparticles (SPIONs) with a diameter of 15 nm were significantly larger than that 30 nm SPIONs at same concentration.[64] Furthermore, the exocytosis rate of 14 nm AuNPs were 2- and 5-fold faster than that of 74 nm and 100 nm AuNPs, respectively.[55] Both endocytosis and exocytosis of nanoparticles highly depend on the size of nanoparticles, but their tendencies are different. In addition to size, nanoparticle shape also affect the exocytosis process. The fraction of gold nanorods released from HeLa and SNB 19 cell line was much higher compared to that of spherical AuNPs.[55] However, in STO cell condition, there was no difference in the fraction of nanoparticle exocytosis for both rod-shaped and spherical AuNPs.[55] These results indicated that the exocytosis pathway also depends upon the cell types.

1.6. Research objectives of the thesis

Photothermal cancer therapy has emerged as a new cancer treatment strategy. As effective photothermal agents, AuNPs have attracted much attention because AuNPs effectively generate heat upon NIR irradiation. However, the tumor-targeting efficiency of intravenously administered AuNPs needs to be improved for the effective photothermal treatment.

In this thesis, we proposed the application of tumor-tropic MSCs as a carrier for tumor-targeted delivery of AuNPs in photothermal therapy. The research objectives of this thesis are summarized as follows: 1) Applying MSCs as a carrier for tumor-targeted delivery of AuNPs. 2) Functionalizing AuNPs to simultaneously enhance cell loading efficiency and photothermal conversion capability. 3) Ultimately, improving efficacy of photothermal cancer therapy.

In chapter 3, the photothermal therapeutic effect of MSCs internalizing pH-sensitive gold nanoparticles (PSAuNPs) was reported. We investigated whether PSAuNPs could improve the cellular retention of AuNPs by preventing exocytosis process through aggregates formation in mildly acidic endosomes. Furthermore, the tumor-targeting effect of PSAuNP-laden MSCs was examined after intravenously injecting these cells to tumor-bearing mice. The photothermal therapeutic effect of intravenously administered PSAuNP-laden MSCs also evaluated for 21 days.

In chapter 4, we reported the plasmonic photothermal therapy using MSCs attaching AuNP/GO hybrid sheets on the surface (MSC-AuNP/GO sheets). The adhering properties of AuNP/GO sheets on the cell surface were assessed. The photothermal capability and AuNP-loading efficiency in cells of MSC-AuNP/GO sheets system were also evaluated. We investigated whether the injection of

AuNP/GO sheet-attached MSCs into tumor-bearing mice could improve the photothermal therapeutic efficacy by delivering larger amounts of AuNPs to the tumor and generating higher heat at tumor region compared to injection of AuNP-internalized MSCs.

Chapter 2.

Experimental procedures

2.1. Cell culture

Human mesenchymal stem cells (hMSCs) and human fibrosarcoma cell line (HT-1080) were purchased from Lonza (USA) and American Type Culture Collection (ATCC, USA), respectively. MSCs and HT-1080 cells were cultured in Dulbecco's Modified Eagle's Medium (Gibco BRL, USA) supplemented with 10 % (v/v) fetal bovine serum (Gibco BRL) and 1 % (v/v) penicillin/streptomycin (Gibco BRL). The cells were incubated at 37 °C with 5 % CO_2 saturation. The medium was changed every 2 days. MSCs at passage 6 were used for this study.

2.2. Preparation and characterization of materials

2.2.1. Synthesis of pH-insensitive, control AuNPs (cAuNPs) and pH-sensitive AuNPs (PSAuNPs)

To synthesize the pH-insensitive, control AuNPs (cAuNPs), 5 mL of a 60 nM 10 nm-sized citrate AuNP solution was adjusted to pH 10.5 using a 1 M NaOH aqueous solution (Sigma Aldrich, USA), and 100 mM 11-mercaptoundecanoic acid (MUA) solution (300 μL, 30 μmol, Sigma Aldrich) in methanol was added. The mixture was stirred at room temperature for 19 h and centrifuged at 1400 g for 5 min to remove the excess solid MUA. The reaction solution was dialyzed using Amicon ultracentrifugal filters (100 kDa Mw cutoff) for purification. To prepare the pH-sensitive AuNPs (PSAuNPs), 4-(2-(6,8-dimercaptooctanamido) ethylamino)-3-methyl-4-oxobut-2-enoic acid (pH-sensitive ligand) was synthesized as previously described.[11] (±)-α-Lipoic acid (2.00 g, 9.70 mmol, Sigma Aldrich) was dissolved in 12 mL anhydrous chloroform. Then, 1,1-carbonyldiimidazole (2.00 g, 12.3 mmol, Sigma Aldrich) was added to the lipoic acid solution and stirred for 5 min at room temperature. The resultant solution was added into ethylenediamine (3.5 mL, 48.4 mmol) and stirred for 40 min in ice bath and for another 30 min at room temperature. The crude product was washed three times with 10 %(w/v) NaCl aqueous solution and once with water. It was dried with sodium sulfate and the solvent was removed using a rotary evaporator to obtain N-(2-aminoethyl)-5-(1,2-dithiolan-3-yl)pentanamide. Citraconic anhydride (0. 68 mL, 7.5 mmol) was added dropwise into 15 mL anhydrous chloroform solution of N-(2-aminoethyl)-5-(1,2-dithiolan-3-yl)pentanamide (5.0 mmol). The solution was stirred overnight at room temperature. The precipitate was filtered and washed with anhydrous chloroform. The synthesized product (0.26 g, 0.72 mmol) was dissolved

in 5 mL water and the pH was adjusted to 10 using 2 M NaOH aqueous solution. Equal molar amount of sodium borohydride was added to the solution and stirred at room temperature for 30 min. Then, the pH-sensitive ligands were eventually obtained and directly used for surface exchange of the 10 nm-sized, citrate-capped AuNPs that were synthesized *via* the conventional Turkevich method.[67] After 10 h, the reaction solution was dialyzed using the Amicon ultracentrifugal filters (100 kDa Mw cutoff) three times for purification.

2.2.2. Characterization of cAuNPs and PSAuNPs

The UV-visible absorption spectra were obtained using an Agilent 8453 UV-visible spectrophotometer (Agilent Technologies). Transmission electron microscopy (TEM) images were obtained using a JEM-2100 (JEOL Ltd.). Surface charges and hydrodynamic sizes were measured using a Zetasizer Nano Z and a Zetasizer Nano S (Malvern Instruments Ltd.), respectively.

2.2.3. Preparation of α-synuclein

Wild-type human α-synuclein protein was prepared according to the procedure reported in a previous study.[68] Alpha-synuclein gene cloned in pRK172 vector was transformed into *Escherichia coli* BL21 (DE3) for α-synuclein overexpression. The boiled cell lysate was subjected to successive purifications using DEAE-Sephacel anion-exchange and Sephacryl S-200 size-exclusion. The purified α-synuclein was dialyzed against a total of 5 L of fresh 20 mM MES at pH 6.5 with two changes, and stored in aliquots at a concentration of 70 μM at − 80 ℃.

2.2.4. Preparation of AuNP/GO hybrid sheets

Sodium citrate tribasic dihydrate (≥ 99 %), gold (III) chloride trihydrate ($HAuCl_4 \cdot 3H_2O$, ≥ 99.9 %) and graphite (< 20 μm) were purchased from Sigma Aldrich and used without further purification. First, the citrate-capped AuNPs were synthesized according to the method developed by Bastús et al.[69] Seed AuNPs were prepared by boiling 150 mL of 2.2 mM sodium citrate under a condenser. Soon after, 1 mL of 25 mM $HAuCl_4$ was added into the boiling solution with continuous stirring. After 10 min, the seed solution was cooled down to 90 ºC. To obtain larger AuNPs, 1 mL of 25 mM $HAuCl_4$ was injected into the seed solution. The reaction was terminated after 30 min. This process was repeated twice. The sample was then diluted by adding 53 mL of deionized water and 2 mL of 60 mM sodium citrate to 55 mL of the sample. This solution was then used as a seed solution, and the process was repeated. The AuNP size was controlled by the number of repeats. Next, GO flakes were synthesized using Hummers' method.[70] The prepared GO was suspended in water (0.05 wt %) and exfoliated using ultrasonication for 3 h. For purification, the solution was dialyzed for 6 h to remove residual acids and salts. Then, the obtained solution was centrifuged at 3000 rpm for 20 min to remove any unexfoliated GO.

The α-synuclein-coated $AuNP_{30nm}$ was prepared by incubating the mixture of 70 μM α-synuclein solution and 0.2 mg/mL $AuNP_{30nm}$ colloidal solution at a volume ratio of 1 : 8 for 12 h at 4 ºC. The α-synuclein-coated $AuNP_{20nm}$ was synthesized by reacting a mixture of 70 μM α-synuclein solution and 0.05 mg/mL $AuNP_{20nm}$ colloidal solution at a volume ratio of 1 : 6 for 12 h at 4 ºC. Unbound α-synuclein molecules were subsequently removed by successive centrifugation and

resuspension with fresh buffer solution. Prepared α-synuclein-coated AuNPs were stored as pellets at 4 ºC.

2.2.5. Characterization of AuNP/GO hybrid sheets

Hydrodynamic diameters of α-synuclein-coated AuNPs were assessed using a dynamic light scattering (DLS) spectrophotometer (Zetasizer Nano ZS90, Malvern Instruments Ltd., UK) with a 10 mW He-Ne laser emitting light at a wavelength of 633 nm and a detection angle of 90 °. For AuNP/GO hybrid sheet, α-synuclein-coated $AuNP_{30nm}$ (0.15 mg) suspended in 50 mM citrate (pH 4.5) was reacted with 1.75 μg of GO for 2 h at 40 ℃. Short bath sonication was applied before the adsorption to fabricate the homogeneous complex. After the first adsorption, 0.03 mg of α-synuclein-coated $AuNP_{20nm}$ was added to the solution and another bath sonication was performed. The mixture was then incubated for 2 h at 40 ℃ and the unreacted AuNPs were removed by centrifugation followed by resuspension with distilled water (DW). An identical procedure was applied to fabricate composites consisting of different protein-coated AuNPs and GO sheets. □κ-Casein, □β-lactoglobulin, bovine serum albumin (BSA) and elastin were purchased from Sigma Aldrich.

AuNP/GO sheets were characterized by SEM, TEM, atomic force microscope (AFM), Raman spectroscopy, and UV-visible spectrophotometry. The AuNP/GO sheets on the copper grid were examined with FE-SEM (SUPRA 55VP, Carl Zeiss, Germany) at 2.0 kV after coating the air-dried samples with a 2-nm-thick layer of platinum (BAL-TEC/SCD 005 sputter coater, Switzerland). The top-viewed TEM image was obtained by examining the AuNP/GO sheets on a carbon-coated 200-mesh copper grid (Ted Pella Inc. CA) with TEM (JEM 1010, JEOL, Japan). The side-viewed TEM image was investigated after sectioning the AuNP/GO sheets embedded in Spurr's resin. The surface morphology and height profile of the sample on poly-L-lysine treated mica surface was examined using an

Innova AFM (Veeco, Plainview, USA). Raman spectra of GO and AuNP/GO sheet on glass surface were measured with Raman spectroscopy (LabRam 300, HORIBA Jobin Yvon, USA). Absorption spectra were obtained by measuring the optical density of a 10-fold diluted solution of the samples using the wavescan mode of UV-visible spectrophotometer (Ultrospec 2100 pro, Amersham Biosciences, Uppsala, Sweden).

2.3. *In vitro* assays

2.3.1. TEM analysis

To investigate intracellular distributions of cAuNPs and PSAuNPs as well as adhesion of AuNP/GO sheets on the MSC surface, TEM analysis was performed. The MSCs were cultured on a 150 mm dish (1 x 10^6 cells/well) and incubated with cAuNPs (100 μg/mL), PSAuNPs (100 μg/mL), AuNPs (50 μg/mL), or AuNP/GO sheets (50 μg AuNP/mL) for 24 h. The cells were then fixed using Karnovsky's fixative for 4 h at 4 °C and rinsed three times with cold 0.05 M cacodylate buffer. The cells were fixed with 1% osmium tetraoxide for 2 h at 4 °C and washed twice with cold DW. The samples were treated with 0.5 % uranyl acetate overnight at 4 °C, dehydrated using graded concentrations of ethanol (30, 50, 70, 80, 90, 95, and 100 %), rinsed with propylene oxide, and finally embedded in Spurr's resin, which were then polymerized at 70 °C for 24 h. Thin sections with thicknesses of 100 nm were obtained using an ultramicrotome (Leica), collected on 200-mesh copper grids, and observed using a TEM (JEM-1010, JEOL Ltd.).

2.3.2. Analyses of adhesion stability of AuNP/GO sheets

We investigated whether the fluid shear stress could affect the adhesion of AuNP/GO sheets on MSC surface. MSCs were labeled with PKH67 (Sigma Aldrich) according to the manufacturer's instructions. The labeled MSCs were cultured on 150 mm dishes and treated with AuNP/GO sheets (50 μg AuNP/mL) for 24 h. The cells were detached *via* 10 mM ethylenediaminetetraacetic acid (EDTA) treatment, and then resuspended in serum-free media. The cell suspension was then exposed to shear stress (30 dyn/cm^2) for 3 min *via* a speed-controllable peristaltic pump (Masterflex L/S Tubing Pump, Cole-Parmer, USA). These cells were then subjected to immunocytochemical staining with antibodies against α-synuclein (Santa Cruz Biotechnology, USA). The immunoreactivity was visualized using rhodamine-conjugated secondary antibodies (Jackson Immuno Research Laboratories Inc., USA). The samples were counterstained with 4',6-diamidino-2-phenylindole (DAPI; Vector Lbt., USA) and imaged using a fluorescence microscope (IX71 inverted microscope, Olympus). For SEM analysis, the MSC-AuNP/GO sheets exposed to the shear stress were fixed overnight using 2.5 % glutaraldehyde at 4 °C. After rinsing in phosphate buffer, the samples were dehydrated using graded concentrations of ethanol and gold sputtered at 30 mA for 200 min under an argon atmosphere. SEM images were obtained with a JSM-6701F (JEOL, Japan).

2.3.3. Quantification of gold amount using ICP-MS

MSCs were treated with materials (cAuNPs, PSAuNPs, AuNPs, or AuNP/GO sheets) for 24 h and rinsed with phosphate buffered saline (PBS) three times to remove unloaded particles. The samples were collected *via* EDTA treatment and lysed with aqua regia. Then, the gold amount was determined *via* inductively coupled plasma-mass spectrometry (ICP-MS; Thermo Electron Co.).

2.3.4. AuNP removal analysis

MSCs were treated with materials (100 μg/mL cAuNPs, 100 μg/mL PSAuNPs, 50 μg/mL AuNPs, or 50 μg AuNP/mL AuNP/GO sheets) for 24 h, rinsed thrice with PBS, and cultured in fresh medium. The cells were washed and collected at various time points (0, 0.5, 1.0, 1.5, 2.5, 4.5, 8, 24, 48, and 72 h). The amount of gold loaded to the MSCs was determined *via* ICP-MS. The fraction of AuNPs removed from the AuNP-MSC complexes (F_{rem}) was calculated using the equation $F_{rem} = (N_0 - N_t) / N_{0,}$ where N_0 is the amount of gold in the cells at t = 0, and N_t is the gold amount remaining in the cells at each time point.[55]

2.3.5. *In vitro* laser irradiation and photothermal imaging

To evaluate the *in vitro* photothermal effect of the MSC-cAuNPs and MSC-PSAuNPs, the MSCs were cultured on 6-well plates (1 x 10^5 cells/well) and incubated with cAuNP 90 μg/mL, PSAuNP 30 μg/mL, or PSAuNP 90 μg/mL for 24 h. After rinsing three times with PBS, MSC-cAuNPs or MSC-PSAuNPs were collected *via* trypsinization and suspended in 20 μL DW. The samples (1 x 10^5 cells in 20 μL DW) loaded in 200 μL microcentrifuge tubes were then irradiated using a 660 nm cw laser beam for 100 sec at a power density of 0.5 W/cm^2. The temperature variations and photothermal images of the AuNP-laden MSCs during laser irradiation were recorded every 20 sec using an infrared thermal imaging system (FLIR i2, FLIR Systems Inc.).

To examine the photothermal effect MSC-AuNPs and MSC-AuNP/GO sheets, the cells were treated with AuNPs or Au/GO sheets for 24 h. After washing thrice with PBS, the MSC-AuNPs or MSC-Au/GO sheets were collected and suspended in 100 μL DW. The samples (5.0×10^4 cells in 100 μL DW) were loaded in 1.5 μL microcentrifuge tubes, and irradiated using an 808 nm cw laser beam for 5 min at a power density of 1.0 W/cm^2. The temperature variations and photothermal images during laser irradiation were recorded every 1 min using an infrared thermal imaging system (FLIR i2).

2.3.6. Intracellular loading of PSAuNPs and in vitro photothermal effect *via* multiple treatments of MSCs with PSAuNPs

After the MSCs were treated either with PSAuNP 50 μg/mL three times or a single treatment of PSAuNP 150 μg/mL, the intracellular loading of the PSAuNPs was examined using TEM, as previously described. To quantify the amount of AuNPs loaded into the MSCs, the MSCs were incubated with a single treatment of 30, 50, or 150 μg/mL PSAuNPs, or with three consecutive treatments of 10 or 50 μg/mL PSAuNPs. The intracellular AuNP amount was then quantified *via* ICP-MS. To evaluate the *in vitro* photothermal effect, the MSCs were incubated with a single treatment of 50 μg/mL PSAuNPs or with three consecutive treatments of 50 μg/mL PSAuNPs. After rinsing three times with PBS, the MSC-PSAuNPs were collected *via* trypsinization and irradiated using a 660 nm laser for 100 sec. The temperature and photothermal images of the MSC-PSAuNPs were recorded every 20 sec using an infrared thermal imaging system.

2.3.7. Cytotoxicity analyses

2.3.7.1. Cytotoxicity analyses of PSAuNPs

Cell viability was evaluated using a cell counting kit-8 (CCK-8; Dojindo Molecular Technologies, Inc.). The CCK-8 assay measures the amount of formazan dye that is reduced by the intracellular dehydrogenase activities.[71] The number of living cells is proportional to the amount of the formazan dye. Briefly, the MSCs (1 x 10^4 cells/well) were cultured on 24-well plates with various concentrations of PSAuNPs for 24 h and rinsed with PBS three times. After replenishing the wells with fresh medium, CCK-8 solution was added into each well and incubated for 2 h. Then, the absorbance was measured at 450 nm using a plate reader. The cell viability was calculated as the percentage of viable cells relative to the AuNP-untreated cells (n = 5 per group).

To evaluate apoptotic and proliferation cctivities of the MSCs. The MSCs were cultured on 6 well-plates (1 x 10^5 cells/well) for 1 day and treated with various concentrations of PSAuNPs three times for 2 days incubation for each. The live and dead cells were detected using fluorescein diacetate (FDA, 5 mg/mL) and ethidium bromide (EB, 10 mg/mL), respectively. The MSCs treated with the PSAuNPs at various concentrations three times were incubated in FDA/EB solution for 5 min at 37 °C and rinsed with PBS. The stained cells were examined using a fluorescence microscope. The apoptotic and proliferation activities of the cells treated with the PSAuNPs at various concentrations were evaluated *via* western blot analysis. The western blot analysis was performed to determine the protein expression of proliferation (proliferating cell nuclear antigen; PCNA) and pro-apoptotic (caspase-3) markers. The samples were centrifuged at 4 °C (15,000 g, 10 min) and resuspended in a cold lysis buffer (50 mM Tris-HCl, pH 8.0, 150 mM

NaCl, 1 % Nonidet P-40) containing a protease inhibitor cocktail for 40 min. Protein extracts were then centrifuged at 4 °C (14,000 rpm, 20 min). The protein concentration was determined using a bicinchoninic acid protein assay (Pierce Biotechnology). The protein extracts were loaded onto a 10 % (w/v) SDS-PAGE, and the gels were transferred to a nitrocellulose membrane using an iBLOT system (Invitrogen). The membrane was blocked with 5 % milk in Tris buffered saline with Tween 20 (TBST) at room temperature for 1 h and then incubated with the primary antibody at room temperature for 1 h. The membrane was washed five times for 10 min each and then incubated with either horseradish peroxidase-conjugated anti-mouse or rabbit antibody in TBST for 30 min. The immunoreactivity was visualized using enhanced chemiluminescence (n = 3 per group). The apoptotic activity of the cells was also evaluated using immunocytochemical staining with antibodies against caspase-3 (Abcam, UK). The immunoreactivity was visualized using rhodamine-conjugated secondary antibodies (Jackson Immuno Research Laboratories Inc., West Grove, PA, USA). The samples were counterstained with DAPI (Vector Lbt.) and imaged using a fluorescence microscope (IX71 inverted microscope, Olympus).

2.3.7.2. Cytotoxicity analyses of AuNP/GO sheets

Cell viability was evaluated using the CCK-8 kit after MSCs were cultured with various concentrations of AuNP/GO sheets for 24 h.[72] The mRNA expression of caspase-3, a pro-apoptotic marker, was evaluated using quantitative real-time polymerase chain reaction (qRT-PCR). SYBR green-based qRT-PCR was performed using a Step One Plus real-time PCR system (Applied Biosystems) with TOPreal^{TM} qPCR 2X PreMIX (Enzynomics). Each cycle entailed the following: 95 °C for 10 sec, 60 °C for 15 sec, and 72 °C for 30 sec. The viable and dead cells were detected by calcein-AM and ethidium homodimer-1, respectively, using a two-color fluorescence live/dead assay kit (Molecular Probes, USA). MSCs treated with the AuNP/GO sheets at various concentrations were incubated in calcein-AM/ethidium homodimer-1 solution for 5 min at 37 °C and rinsed with PBS. The stained cells were examined using a fluorescence microscope. The apoptotic cells were analyzed by immunocytochemical staining using anti-caspase-3 antibody (Abcam) and detected with rhodamine isothiocyanate-conjugated secondary antibodies (Jackson ImmunoResearch Laboratories). The samples were counterstained in DAPI (Vector Laboratories) for nuclear staining and imaged using a fluorescence microscope. Cell membrane integrity was evaluated using a lactate dehydrogenase (LDH) assay kit (BioVision, USA). In brief, MSCs were incubated with AuNPs or AuNP/GO sheets for 1 and 3 days. The plate was centrifuged to precipitate the samples and the supernatant (0.1 mL/well) was transferred to new 96-well plate. Then, 0.1 mL of reaction mixture was added to each well and the samples were incubated for 30 min at room temperature. After incubation, the absorbance of solution was recorded at 495 nm. Positive control was prepared by adding lysis solution to the cells. The LDH release (% of lysis

control) is expressed as the percentage of $(OD_{test} - OD_{blank})/(OD_{positive} - OD_{blank})$, where OD_{blank} is an absorbance value of the no treatment group.

2.3.8. Analysis of AuNP/GO sheet adsorption on MSCs

To evaluate the adsorption of fibronectin on AuNP/GO sheets, we incubated AuNP/GO sheets in serum-containing medium or serum-free medium for 1 day at 37 ºC. Furthermore, to investigate the underlying mechanisms by which AuNP/GO sheets are attached to MSC surface, MSCs with or without AuNP/GO sheets were cultured on agar-coated plates in serum-containing medium or serum-free medium for 1 day; the agar coating prevents cell adhesion to the plates. the samples were centrifuged at 4 °C (1,500 rpm, 5 min) and resuspended in a cold lysis buffer containing a protease inhibitor cocktail for 40 min. Then, the samples were analyzed through western blotting.

2.3.9. *In vitro* stability of AuNP/GO sheets in biological fluids

AuNP/GO sheets (20 μg) were incubated in 200 μL of serum-containing medium or human plasma (Sigma Aldrich) at 37 ºC. After 6, 24, and 72 h of incubation, the unleashed AuNPs were collected by centrifugation and quantified using a ICP-MS.

2.3.10. *In vitro* tumor-tropism analysis

The migration of MSC-AuNP/GO sheets toward tumor spheroids was assessed using fluorescence staining. Tumor spheroids were formed by modifying the centrifugation method.[73] DAPI-labeled HT-1080 cells (5×10^4 cells) were centrifuged at 1500 rpm for 10 min and cultured in 15 mL centrifuge tubes for 2 days. Tumor spheroids were then carefully plated on agar-coated plates and cocultured with DiI-labeled dermal fibroblasts, MSCs, MSC-AuNPs or MSC-AuNP/GO sheets (1×10^5 cells) for 1 day. Dermal fibroblasts and MSCs were used as the negative and positive controls, respectively. The samples were analyzed using a confocal microscope (SP8X, Leica).

2.4. *In vivo* assays

2.4.1. *In vivo* tumor model

All animal experiments were performed using six-week-old female BALB/c athymic nude mice (Orient Bio, Korea). Mice were anesthetized with xylazine (10 mg/kg) and ketamine (100 mg/kg), and HT-1080 human fibrosarcoma cells (5×10^6 cells in 100 μL PBS per mouse) were subcutaneously injected into the flank of the mice. The animal studies for MSC-PSAuNPs and MSC-AuNP/GO sheets were approved by the Institutional Animal Care and Use Committee of Seoul National University (SNU-140513-6-1 and SNU-140513-6-2, respectively).

2.4.2. *In vivo* MSC imaging

For tracking the migration of MSCs in tumor-bearing mice, the samples (MSCs, MSC-PSAuNPs, MSC-AuNPs 1×, MSC-AuNP/GO sheets 0.25×, or MSC-AuNP/GO sheets 1×) were labeled with VivoTrack 680 (PerkinElmer, USA). The labeled cells were suspended in PBS (1×10^6 cells in 100 μL PBS) and intravenously injected *via* the tail vein (n = 3 per group). After 3 days, the biodistributions of the samples in the tumor-bearing mice were examined using an eXplore Optix System (ART Advanced Research Technologies Inc., Canada).

2.4.3. Biodistribution of AuNPs in major tissues and tumors

2.4.3.1. Biodistribution analyses of MSC-PSAuNPs

The MSCs (3 x 10^5 cells) were incubated with the same concentration (50 μg/mL) of PSAuNPs or cAuNPS for 2 days, and the AuNP incubation process was repeated three times. The MSC-PSAuNPs or MSC-cAuNPs were rinsed with PBS, suspended in PBS solution, and injected intravenously into the tumor-bearing mice when the tumors reached approximately 7 mm in diameter. Each mouse in the MSC-cAuNP group and MSC-PSAuNP group received 2 x 10^6 cells and 1 x 10^6 cells, respectively, since these numbers of cells contained the same amount (153 μg) of AuNPs. PBS, cAuNPs, or PSAuNPs solutions were also intravenously administered as control groups. The cAuNP, MSC-cAuNP, PSAuNP, and MSC-PSAuNP groups received the same amount (153 μg) of AuNPs per mouse. The gold amount of each group was determined *via* ICP-MS prior to the intravenous administration. For the CT analysis, the tumor tissues were fixed in 4 % paraformaldehyde in PBS for 24 h at 3 days post-intravenous injection. The CT images of the tumor tissues were obtained using a micro-CT system (SkyScan-1076; Skyscan, 40 kV, 250 mA) and CT image processing was performed using CT analyzer software (Skyscan). To quantify the amount of AuNPs in the tumor tissues and major organs (spleen, liver, kidney, lung, heart, and brain), the mice were sacrificed at 3 days post-intravenous injection, and the tissues and organs were retrieved and lysed using aqua regia. The amount of AuNPs in the tissues and organs was determined *via* ICP-MS and expressed as a percentage of the injected dose of AuNPs.

2.4.3.2. Biodistribution analysis of MSC-AuNP/GO sheets

MSCs were incubated with 50 μg/mL AuNPs (1×), 12.5 μg AuNP/mL in AuNP/GO sheets (0.25×), or 50 μg AuNP/mL in AuNP/GO sheets (1×) for 1 day. The samples were rinsed thrice with PBS, collected *via* EDTA treatment, and resuspended in PBS solution. Following this, the samples (1×10^6 cells in 100 μL per mouse) were intravenously administered into the tumor-bearing mice when the tumor size had reached approximately 7 mm in diameter. The solutions of AuNPs or AuNP/GO sheets were also intravenously injected as control groups. The AuNP, AuNP/GO sheet, MSC-AuNP 1×, and MSC-AuNP/GO sheet 0.25× groups were given the same amount (212.6 μg) of AuNPs per mouse. The MSC-AuNP/GO sheet 1× group received 716.5 μg of AuNPs per mouse. To quantify the amount of AuNPs in the major organs (spleen, liver, kidney, lung, heart, and stomach), blood, and tumor tissues, the mice were sacrificed at 3 days post-intravenous injection. The organs and tissues were retrieved and lysed using aqua regia. The amount of AuNPs in the organs and tumor tissues was measured *via* ICP-MS and expressed as a percentage of the injected dose of AuNPs per g tissues.

2.4.4. *In vivo* photothermal therapy

Tumor-bearing mice were randomly sorted for treatments when the tumor size reached approximately 7 mm in diameter. For the MSC-PSAuNP study, PBS, cAuNPs, MSC-cAuNPs (2×10^6 cells), PSAuNPs, or MSC-PSAuNPs (1×10^6 cells) in 100 μL of PBS were intravenously injected into each of the tumor-bearing mice. Each mouse of the cAuNP, MSC-cAuNP, PSAuNP, and MSC-PSAuNP groups received the same amount (153 μg) of AuNPs. In addition, for the MSC-AuNP/GO sheet study, each mouse of the MSC-AuNP/GO sheet 1× group received 716.5 μg of AuNPs, and the other groups (AuNP, AuNP/GO sheet, MSC-AuNP, and MSC-AuNP/GO sheet 0.25×) received 212.6 μg of AuNPs; PBS and MSC groups did not receive any AuNPs. After 3 days post-injection, the tumor tissues of MSC-PSAuNP and MSC-AuNP/GO sheet studies were exposed to the laser (the MSC-PSAuNP study; 660 nm cw diode laser, 0.5 W/cm^2 and the MSC-AuNP/GO sheet study; 808 nm cw diode laser, 1.5 W/cm^2) for 1 and 5 min under anesthesia, respectively. The temperature variations at the tumor regions were recorded using a real-time infrared thermal imaging system (FLIR i2). Tumor sizes were measured using a digital caliper every 3 days, for 21 days. The tumor volume was estimated according to the ellipsoidal calculation, $V = a \times b^2 \times 0.5$, where a is the largest and b is the smallest diameter.[74] For histological analysis, tumor tissues were retrieved at 1 day post-laser irradiation and fixed with 4 % paraformaldehyde in PBS. The samples were embedded in paraffin and sectioned at a thickness of 6 μm. The sections of tumor tissue were stained using hematoxylin and eosin, and analyzed using an optical microscope.

2.5. Statistical analysis

Quantitative data were expressed as the means ± standard deviations. The statistical analysis was performed using one-way analysis of variance (ANOVA) with the Tukey's significant difference post hoc test using SPSS software (SPSS Inc., USA). A value of $p < 0.05$ was considered to denote statistical significance.

Chapter 3.

pH-sensitive gold nanoparticles loaded in mesenchymal stem cells for effective photothermal cancer therapy

3.1. Introduction

Plasmonic photothermal therapy is a spatiotemporally controllable heat shock strategy for cancer treatment.[1] Gold nanoparticles (AuNPs) have been intensively investigated as a photothermal agent for photothermal cancer therapy.[9-11] AuNPs efficiently generate heat by absorbing the extrinsic light energy at the plasmonic resonant wavelength. Previous studies have reported on the efficient photothermal therapy using NIR-responsive gold nanostructures such as nanoshells,[75] nanorods,[76] and nanomatryoshkas.[77] Here, we used previously developed pH-sensitive aggregative AuNPs (PSAuNPs) that selectively aggregate under mild acidic conditions.[11] The PSAuNPs consist of ~ 10 nm gold nanospheres, which can be easily synthesized in large scale,[78] and pH-susceptible surface ligands. Under mild acidic conditions, such as the pH in cellular acidic endosomes/lysosomes, the negatively charged surfaces of PSAuNPs are converted to positive and negative charges, which rapidly causes aggregation of the nanoparticles through electrostatic interactions. As the aggregation of AuNPs induces the absorption red-shift to near-infrared (NIR) region, PSAuNP aggregates exhibit stronger photothermal effects upon the NIR irradiation compared to unmodified AuNPs.[11] Furthermore, PSAuNP aggregates exhibit higher photostability than gold nanorods, which shows the potential of PSAuNPs as the efficient and long-term stable photothermal agents. Although various gold nanostructures that can efficiently generate heat upon NIR-laser irradiation have been developed, it still remains challenging to improve the tumor-targeting efficiency and intratumoral distribution of these nanostructures for the effective photothermal treatment.

Tumor-tropic cells have been used as delivery vehicles that can transport nanoparticle to tumor tissues.[37-40] Here, we used MSCs, which are tumor tropic, as

the nanoparticle-delivery vehicle based on the several distinct features of MSCs. It was demonstrated that the tumor-tropic properties of MSCs are exhibited regardless of the tumor type. Furthermore, MSCs can be easily isolated from the patients and extensively expanded *in vitro*.[50] MSCs also exhibit minimal immunogenicity and even immunosuppressive property upon transplantation.[50-51] Therefore, AuNP-laden MSCs can serve as a stealth vehicle to deliver AuNPs to tumors, as they can avoid the surveillance of immune cells to safely arrive at the target tumor tissues.

In cell-mediated nanoparticle delivery systems, it is important to retain the loaded AuNPs within cells during their migration to the tumor tissues because nanoparticles can easily escape from cells through exocytosis.[55] This lowers the tumor-targeting efficiency of the nanoparticles. The endocytosis and exocytosis of nanoparticles depend on the size and shape of nanoparticles.[54-55] Spherical-shaped PSAuNPs can be efficiently endocytosed into cells and the formation of large-sized PSAuNP aggregates in cells can prevent exocytosis of AuNPs,[54-55] consequently enhancing cellular retention. In this study, we hypothesized that MSCs loaded with PSAuNPs (MSC-PSAuNPs) would enhance the tumor-targeting efficiency and the plasmonic photothermal effect of AuNPs by inducing the aggregation of AuNPs within the MSCs and reducing AuNP exocytosis. First, we investigated whether high loading of PSAuNPs in MSCs could be obtained by efficiently reducing the exocytosis of PSAuNPs *via* PSAuNP aggregation in the MSCs (see mechanism in Figure 3.1). Then, we investigated whether the *in vitro* photothermal capability of the PSAuNP aggregates in MSCs, which were larger in size than pH-insensitive, control AuNPs (cAuNPs) in MSCs, was improved. We also established a method of multiple treatments with AuNPs to maximize AuNP loading in MSCs. Following intravenous injection of MSC-PSAuNPs into tumor-bearing mice, we

demonstrated the high tumor-targeting efficiency of the MSC-PSAuNPs *via* imaging and investigated the biodistributions of AuNPs in the tumor tissues and distant organs. The enhanced photothermal therapeutic efficiency of the MSC-PSAuNP was demonstrated by observing the prognosis for 21 days and performing gene expression and histological analysis.

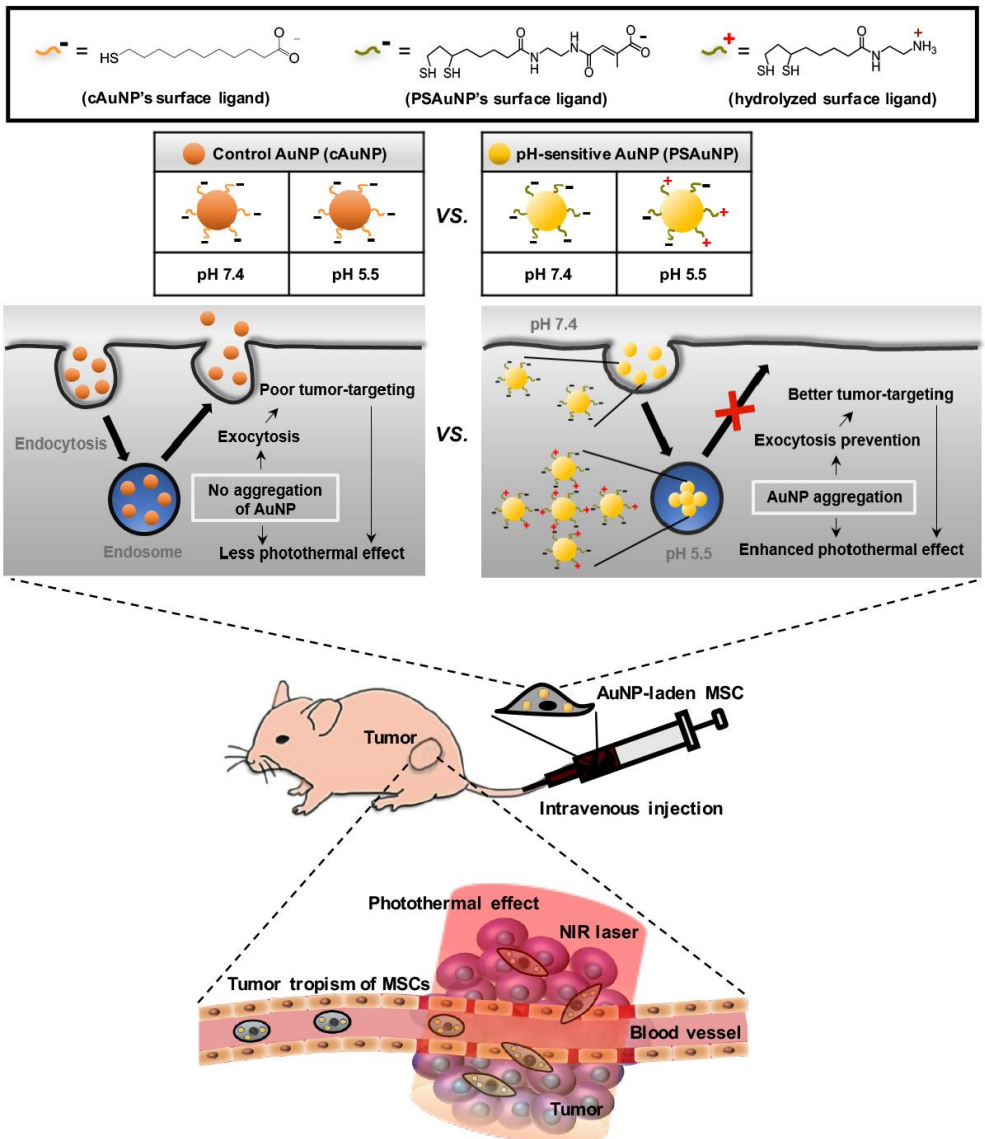

Figure 3.1. Schematic illustration of the working mechanisms of the improved tumor-targeting efficiency and photothermal effect of the AuNPs by employing pH-sensitive aggregative AuNP-laden mesenchymal stem cells (MSC-PSAuNPs). Unlike cAuNPs, PSAuNPs change their surface charge from negative charge to a mixture of negative and positive charges because some of the citraconic amide is hydrolyzed at a mild acidic

condition. This partial hydrolysis of the PSAuNPs' surface ligands causes AuNP aggregation through electrostatic interactions. The AuNPs can be taken up by mesenchymal stem cells (MSCs) and delivered to the target tumor region *via* the tumor-tropic properties of MSCs. pH-insensitive cAuNPs are easily exocytosed from MSCs, which results in low tumor-targeting efficiency, and induce poor photothermal effects due to their small size and low tumor-targeting efficiency. In contrast, the cancer treatment strategy using MSC-PSAuNPs can enhance the anti-cancer therapeutic effects, as the PSAuNPs cluster together in acidic endosomes in the MSCs, which enhances the tumor-targeting efficiency of AuNPs *via* preventing exocytosis and increases the photothermal effect *via* the stronger resonant absorption.

3.2. Results and discussion

3.2.1. Characterization of PSAuNPs

PSAuNPs were prepared using the method described in our previous report.[11] The pH-sensitive aggregation of PSAuNPs was examined in buffer solutions under pH 7.4 or 5.5. We observed the surface plasmon resonance of the AuNPs by monitoring the absorption over time. The cAuNPs exhibited no noticeable absorption change in both the pH 5.5 and pH 7.4 buffer environments (Figure 3.2A). In contrast, the PSAuNPs in the pH 5.5 environment exhibited a continuous absorption red-shift and broadening over time, although in the pH 7.4 environment they exhibited negligible absorption change (Figure 3.2A). These results indicate a pH-sensitive aggregation of the PSAuNPs, as the broadening red-shifted absorption is attributed to the coupled plasmons between closely located AuNPs.[11] The zeta-potential and the hydrodynamic size of the AuNPs were measured over time in the pH 5.5 and pH 7.4 environments. Although the zeta-potential of the cAuNPs was – 30 mV under both pH conditions, the PSAuNPs in the pH 5.5 exhibited significant changes in the zeta-potential from – 30 mV to – 9 mV (Figure 3.2B). This indicates that the surface charge of the PSAuNPs was partially converted from negative to positive under the mild acidic conditions. The hydrodynamic size changes coincided with the zeta-potential. The cAuNPs retained their initial hydrodynamic size (14 nm) throughout the period (Figure 3.2C). In contrast, the PSAuNPs in pH 5.5 exhibited a rapid increase in hydrodynamic size from 14 nm to 90 nm within 30 min, whereas there was no noticeable change in pH 7.4 (Figure 3.2C). The transmission electron microscopy (TEM) analysis further confirmed the aggregation of PSAuNPs under the acidic conditions. In the pH 5.5 environment, the PSAuNPs clustered over time, whereas no noticeable size change was observed

for the cAuNPs (Figure 3.2D). Taken together, these results demonstrate that the PSAuNPs are indeed pH-sensitive aggregative. To compare the properties of PSAuNPs and cAuNPs at the cellular level, PSAuNPs or cAuNPs were added to MSC culture. The TEM analysis revealed PSAuNP aggregates that were > 200 nm in diameter within the intracellular vesicles (Figure 3.2E). The pH-sensitive aggregative property of the PSAuNPs led to the formation of PSAuNP clusters likely in the acidic endosomes of the MSCs. Furthermore, the amount of PSAuNPs in each intracellular vesicle seemed to be greater than that of cAuNPs (Figure 3.2E), which was likely due to proton sponge effect of PSAuNPs. During endosomal maturation, early endosomes (pH = 6.8 – 5.9) accumulate endocytosed molecules by fusion with each other.[79-81] Along with decreasing the endosomal pH by about 0.5 units, early endosomes are converted to late endosomes (pH = 6.0 – 4.9) and subsequently fuse with lysosomes (pH = 5.0 – 4.5).[79-81] Previous studies have demonstrated that bafilomycin, a vacuolar H^+-ATPase inhibitor blocking the pH changes in acidic organelles, slows down the progression of early endosomes to lysosomes.[82-84] Based on those reports, we postulated that the endocytosed PSAuNPs would also hinder the endosomal pH drop as carboxylic acid groups of pH-sensitive ligands have proton-absorbing capability inside the mildly acidic endosomes (Figure 3.2B). Therefore, the endosomes containing PSAuNPs would have more chances to fuse with each other due to the extended time of the endosomal maturation compared to those containing cAuNPs, which was likely to induce more PSAuNPs to be accumulated in each intracellular vesicle.

Next, the cellular uptake of the AuNPs was quantitatively evaluated using ICP-MS after incubating the MSCs with the same concentration of PSAuNPs or cAuNPs for 24 h. The MSCs treated with PSAuNPs exhibited a 4-fold higher accumulation than those treated with cAuNPs (Figure 3.3A). A possible

explanation for the increased content of AuNPs in the MSCs is the suppression of AuNP exocytosis. To examine the dynamics of AuNP exocytosis, the MSCs were cultured with PSAuNPs or cAuNPs for 24 h and washed 3 times to remove the non-internalized AuNPs. After replenishing the culture dish with fresh medium, the quantity of AuNPs in the MSCs was determined *via* ICP-MS at various culture-time points (Figure 3.3B). We calculated the fraction of exocytosed AuNPs (F_{exo}) using the previously described equation:[55]

$$F_{exo} = \frac{N_{out}}{N_0}$$

where N_{out} is the quantity of AuNPs exocytosed from the MSCs at time t, and N_0 is the initial quantity of AuNPs contained in the MSCs. Interestingly, a lower fraction of the PSAuNPs were exocytosed at a slower rate compared to the cAuNPs (Figure 3.3B). At 72 h, the exocytosed fraction of the PSAuNPs (29 %) was only the half of that of the cAuNPs (60 %). From the exocytosis kinetics, we inferred the half-life of the AuNPs, which was defined as the time taken to reach half of the fraction of exocytosed AuNPs at steady state.[55] The half-life values of the cAuNPs and PSAuNPs were 0.58 h and 1.90 h, respectively. This result confirmed that the exocytosis rate of the PSAuNPs was much slower than that of the cAuNPs. Previous studies have demonstrated that both endocytosis and exocytosis of nanoparticles occur in a size-dependent manner.[54-55] Nanoparticles with diameters smaller than 100 nm are not only more easily taken up by cells,[54] but also more easily released from the cells.[55] The PSAuNPs exhibit ambivalent characteristics, which can lead to effective intracellular accumulation of AuNPs. Once the PSAuNPs (14 nm in size) at physiological pH are efficiently endocytosed, the PSAuNPs aggregates (> 100 nm in size) are formed in acidic endosomes and poorly exocytosed.

The *in vitro* photothermal effect of the PSAuNP-laden MSCs was evaluated *via* a real-time infrared thermal imaging system during 660 nm laser irradiation at a power density of 0.5 W/cm^2 (Figure 3.3C). The temperature profiles of the MSCs following treatment with various concentrations of PSAuNP (30 or 90 μg/mL) or cAuNP (90 μg/mL) were observed for 100 sec of laser irradiation. The photothermal effect of the AuNPs depends on the size and amount of AuNPs.[9,17,85] The resonant absorption properties of AuNPs induce heat generation upon laser irradiation.[86] As the diameter of AuNPs increases, the surface plasmon absorption is red-shifted toward the NIR region (Figure 3.2A). Therefore, when NIR laser is irradiated, PSAuNP aggregates with larger diameters yield higher light-to-heat conversion than AuNPs with smaller diameters. The temperatures of the MSCs treated with same concentration (90 μg/mL) of PSAuNP and cAuNP increased to 49.3 and 40.3 °C, respectively, after 100 sec of irradiation (Figure 3.3C). The higher temperature in the MSC-PSAuNP 90 μg/mL group is attributed to the larger intracellular amount and size of the PSAuNPs. In addition, the MSC-PSAuNP 30 μg/mL group exhibited a higher temperature profile compared to the MSC-cAuNP 90 μg/mL group (Figure 3.3C).

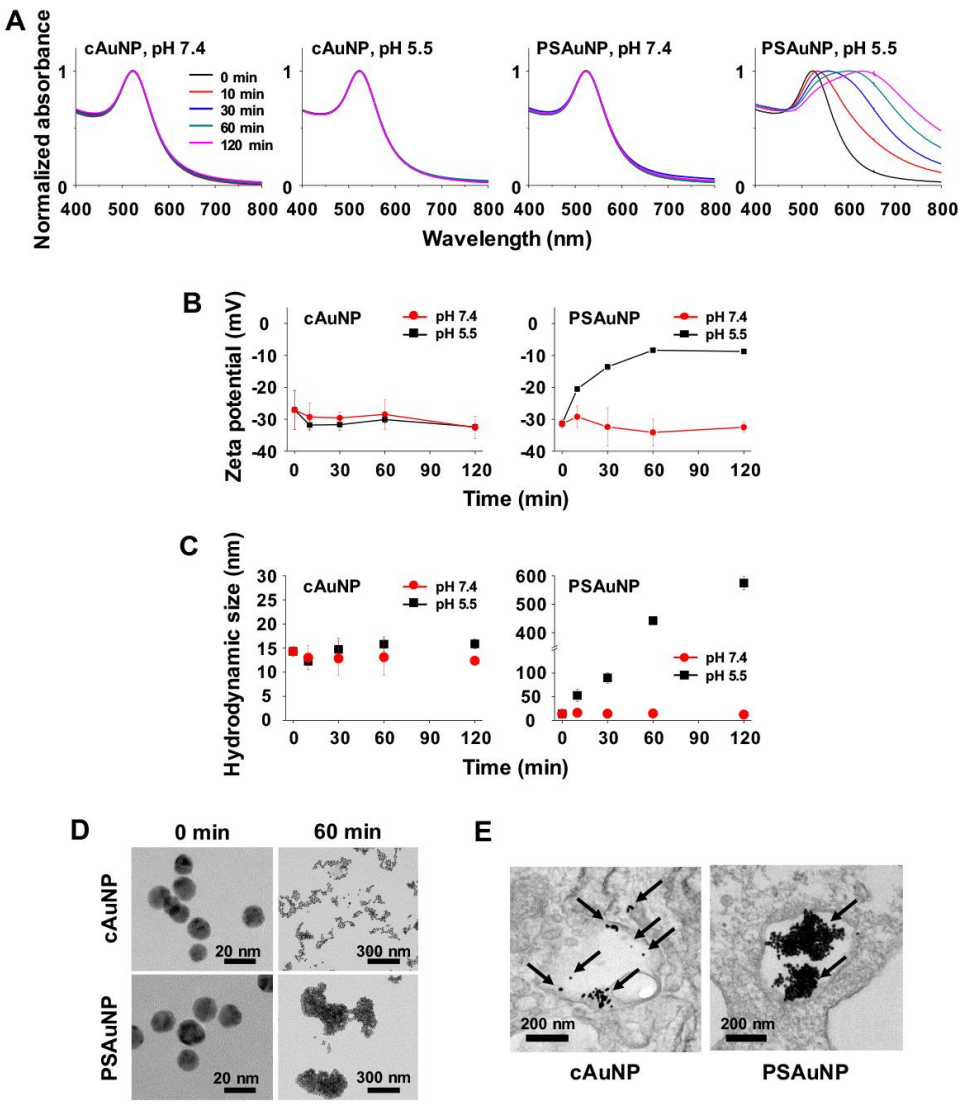

Figure 3.2. pH-dependent aggregation of the PSAuNPs. (A) Time evolution of absorption at pH 7.4 and pH 5.5 for cAuNPs and PSAuNPs. (B) Zeta-potential and (C) hydrodynamic size of the cAuNPs (left) and PSAuNPs (right) at pH 5.5 and pH 7.4. (D) TEM images of the cAuNPs and the PSAuNPs at pH 5.5 for various elapsed times. (E) TEM images showing the intracellular localization of AuNPs (arrows) after incubating the MSCs with the same concentration of cAuNPs or PSAuNPs for 24 h. Scale bars = 200 nm.

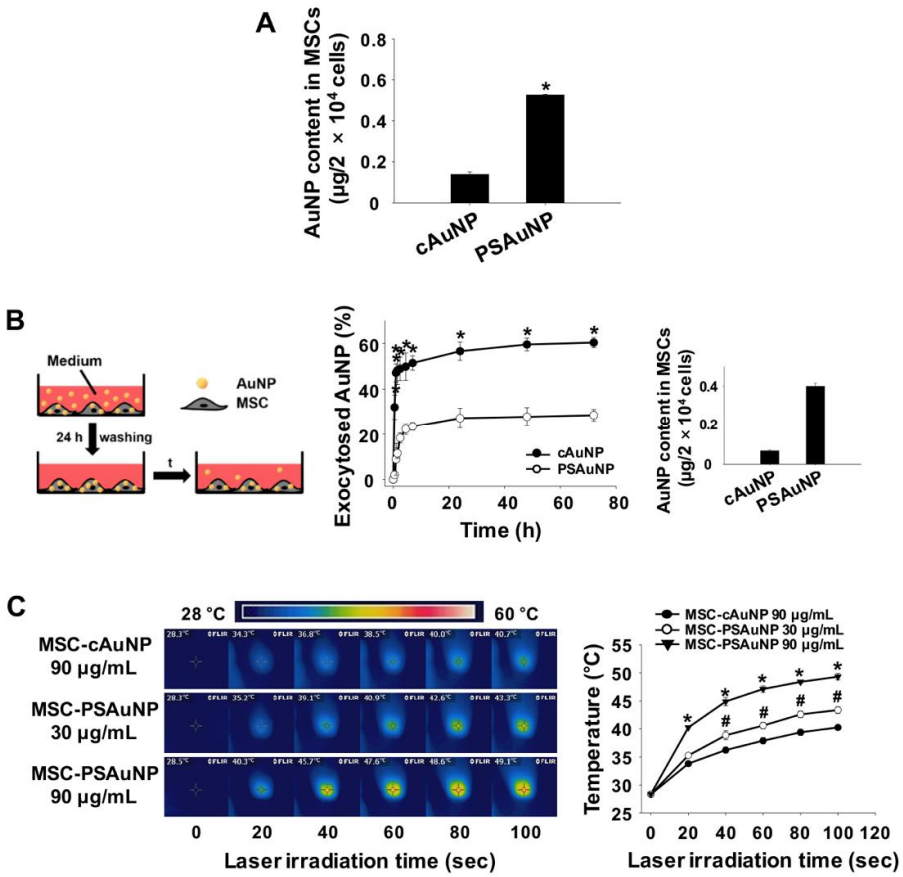

Figure 3.3. Exocytosis and photothermal properties of the PSAuNPs in the MSCs. (A) Intracellular amounts of AuNPs after incubating the MSCs with the same concentration (100 μg/mL) of cAuNPs or PSAuNPs for 24 h, as evaluated *via* ICP-MS (n = 4). * $p < 0.05$. (B) Time profiles of AuNP exocytosis (n = 4) and the intracellular amounts of AuNPs in the MSCs at t = 72 h (n = 4). The MSCs were cultured with the same concentration of PSAuNPs or cAuNPs for 24 h and then washed to eliminate the non-internalized AuNPs. After replenishing the culture dish with fresh medium, the amount of AuNPs in the cells was determined *via* ICP-MS over time to evaluate the exocytosed AuNPs at various time points (t). * $p < 0.05$. (C) Temperature profiles of the AuNP-laden MSCs during the laser irradiations (n = 5). * $p < 0.05$ *versus* any group, $^{\#}$ $p < 0.05$ *versus* MSC-cAuNP 90 μg/mL group.

3.2.2. Optimizing the PSAuNP dose and multiple treatments

To maximize the quantity of PSAuNPs loaded in the MSCs, the PSAuNP dose and the PSAuNP treatment method must be optimized. The MSCs were incubated with various concentrations of PSAuNPs for 24 h. The cell viability was then evaluated using a cell counting kit-8 (CCK-8). Compared to the no treatment group, the MSCs treated with 500 μg/mL PSAuNPs exhibited a significantly reduced cell viability (Figure 3.4A). However, 100 μg/mL PSAuNPs did not cause cytotoxicity. From these results, we determined that 100 μg/mL of PSAuNPs is the maximum concentration that does not cause the cytotoxicity. A previous study has demonstrated that the negatively charged AuNPs, such as cAuNPs and PSAuNPs, can cause a dose-dependent cytotoxicity.[87] When a large amount of the negatively charged AuNPs are internalized into cells, the stressed mitochondria increases the intracellular amount of calcium ions.[87] Consequently, the cells treated with a large amount of the negatively charged AuNPs undergo the calcium-evoked apoptosis.

Next, we investigated whether multiple treatments of MSCs with PSAuNPs increase the intracellular loading of PSAuNPs *in vitro*. In previous studies, cells have been subjected to only a single treatment of nanoparticles for cellular uptake.[37,88-89] For the first time, we incubated the MSCs with PSAuNPs three times for 2 days each. Briefly, the MSCs were incubated with PSAuNPs for 2 days and then replenished with fresh medium containing new PSAuNPs. This procedure was carried out three times. The cell viability and apoptotic activity were assessed using live/dead imaging, western blotting, quantitative real-time PCR (qRT-PCR), and immunocytochemical staining. The live/dead cell staining indicated that the three consecutive treatments with 100 μg/mL PSAuNPs caused cytotoxicity (Figure 3.4B). The western blot analysis for a pro-apoptotic marker

(Caspase-3) and a proliferating cell nuclear antigen (PCNA) also demonstrated that the three consecutive treatments with 100 μg/mL PSAuNPs induced apoptotic activity and decreased the proliferating capability (Figure 3.4C). Furthermore, the number of Caspase-3-positive cells was significantly increased in the 100 μg/mL PSAuNP × 3 group compared to the 50 μg/mL PSAuNP × 3 group (Figure 3.4D). These analyses confirmed that 50 μg/mL of PSAuNPs is a suitable concentration for the three repeated treatments because cell viability, proliferation, and apoptosis of the 50 μg/mL PSAuNP × 3 group were not significantly different compared to the no treatment group (Figure 3.4B-D).

Multiple treatments of MSCs with PSAuNPs increased intracellular loading of the PSAuNPs *in vitro*. The TEM analysis revealed that the intracellular amount of PSAuNP aggregates was increased in the MSC-PSAuNP 50 μg/mL × 3 group compared to the MSC-PSAuNP 150 μg/mL × 1 group (Figure 3.4E). The ICP-MS analysis for quantifying the intracellular PSAuNP content indicated that the MSC-PSAuNP 50 μg/mL × 3 group corresponded to 14.8-fold and 6.0-fold higher intracellular contents of PSAuNPs compared to the MSC-PSAuNP 50 μg/mL × 1 group and the MSC-PSAuNP 150 μg/mL × 1 group, respectively (Figure 3.4F). The PSAuNP content in cells in the 150 μg/mL PSAuNP treatment group was much smaller than that in the 50 μg/mL PSAuNP × 3 group (Figure 3.4F). This was likely due to the higher toxicity of the 150 μg/mL PSAuNP treatment compared to that of the 50 μg/mL PSAuNP × 3 treatment (Figure 3.4C-D). For the determination of intracellular AuNP contents, cells were washed with PBS three times. In this procedure, a large amount of PSAuNPs were likely washed out from the dead cells in the 150 μg/mL PSAuNP treatment group that contains more dead cells than the 50 μg/mL PSAuNP × 3 treatment group. Meanwhile, as

shown in the TEM images (Figure 3.4E), the PSAuNPs in the MSCs were located in vesicles, which indicates that the PSAuNPs were internalized primarily *via* endocytosis.[90] In this pathway of cellular uptake, specific regions of the plasma membrane wrap around the PSAuNPs and then detach to form internalized vesicles. As the surface area and the recovery time of the plasma membrane are restricted,[90] the endocytosis efficiency is limited. Therefore, the cells treated with a low concentration of nanoparticles for a longer time period internalize more nanoparticles than those treated with a high concentration of nanoparticles for a short time period.

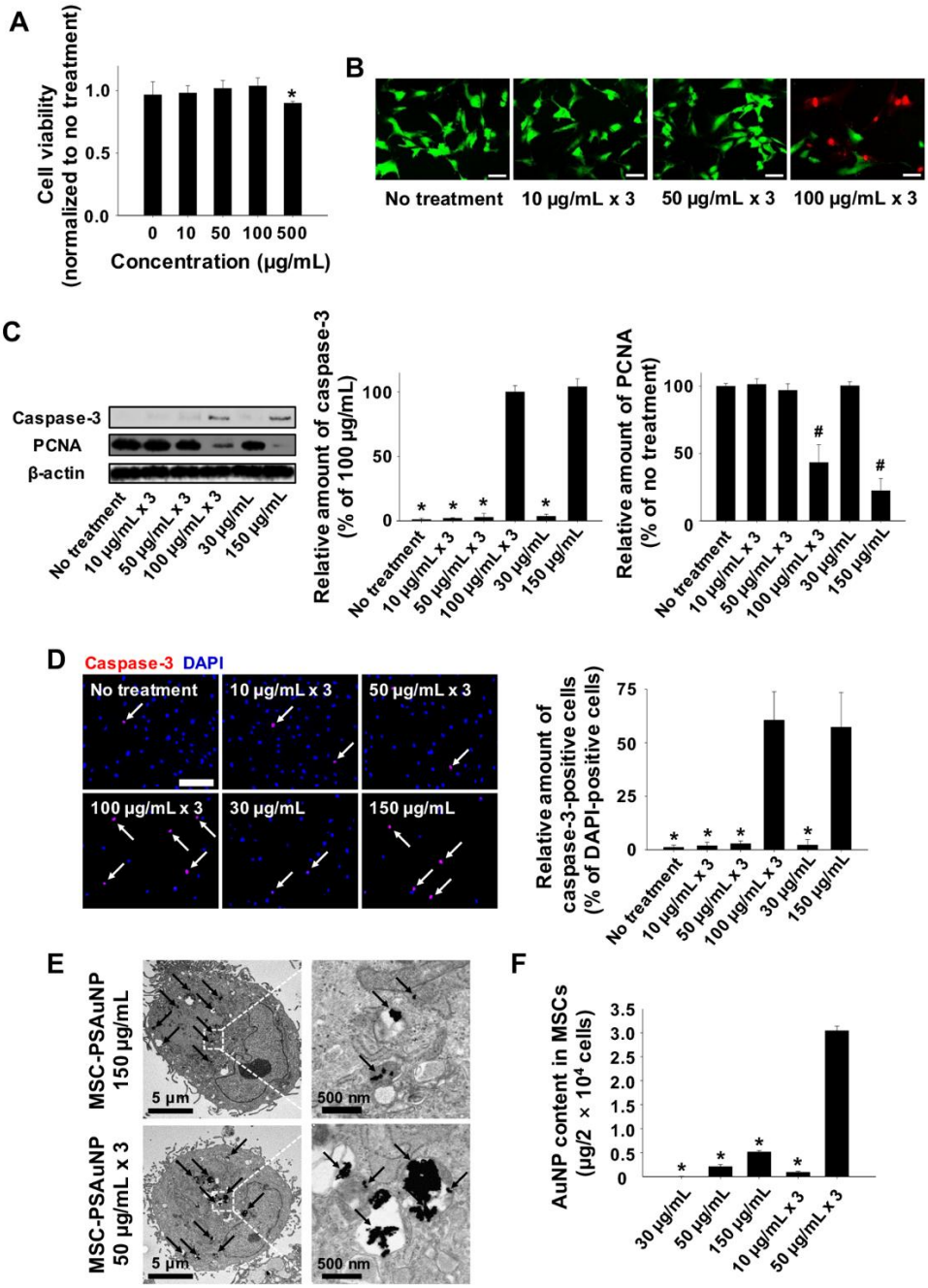
A
Cell viability (normalized to no treatment)
1.0
0.5
0.0
0 10 50 100 500
Concentration (μg/mL)
B
No treatment
10 μg/mL x 3
50 μg/mL x 3
100 μg/mL x 3
C
Caspase-3
PCNA
β-actin
No treatment
10 μg/mL x 3
50 μg/mL x 3
100 μg/mL x 3
30 μg/mL
150 μg/mL
Relative amount of caspase-3 (% of 100 μg/mL)
100
50
0
Relative amount of PCNA (% of no treatment)
100
50
0
#
D
Caspase-3 DAPI
No treatment
10 μg/mL x 3
50 μg/mL x 3
100 μg/mL x 3
30 μg/mL
150 μg/mL
Relative amount of caspase-3-positive cells (% of DAPI-positive cells)
75
50
25
0
E
MSC-PSAuNP 150 μg/mL
MSC-PSAuNP 50 μg/mL x 3
5 μm
500 nm
F
AuNP content in MSCs (μg/2 × 10⁴ cells)
3.5
3.0
2.5
2.0
1.5
1.0
0.5
0
30 μg/mL
50 μg/mL
150 μg/mL
10 μg/mL x 3
50 μg/mL x 3

Figure 3.4. PSAuNP dose optimization and multiple treatments. Cytotoxicity of the PSAuNPs at various concentrations, which was evaluated by determining the viability of the MSCs according to (A) cell counting kit-8 assay following culture for 1 day with various concentrations of PSAuNPs. * $p < 0.05$ *versus* any group. (B) Fluorescence images of the MSCs stained with FDA/EB after three treatments with various concentrations of PSAuNPs. Green and red indicate viable and dead cells, respectively. Scale bars = 100 μm. (C) Apoptotic and proliferation activity of the MSCs after one or three treatments with various concentrations of PSAuNPs, as evaluated *via* western blotting for a pro-apoptotic marker (Caspase-3) and a cell proliferating marker (PCNA). * $p < 0.05$ *versus* the 100 μg/mL × 3 or the 150 μg/mL group. $^{\#}$ $p < 0.05$ *versus* the no treatment group. (D) The apoptotic activity of the MSCs after one or three treatments with various concentrations of PSAuNPs, as evaluated *via* immunocytochemical staining for Caspase-3 (red). The cell nuclei are stained with DAPI (blue). Scale bars = 100 μm. * $p < 0.05$ *versus* the 100 μg/mL × 3 or the 150 μg/mL group. $^{\#}$ $p < 0.05$ *versus* the no treatment group. (E) TEM images showing the intracellular localization of PSAuNPs in the MSCs after a single treatment with 150 μg/mL PSAuNPs or three consecutive treatments with 50 μg/mL PSAuNPs. The magnified images show the representative PSAuNP aggregates. (F) The intracellular amounts of PSAuNPs in the MSCs after a single treatment or three consecutive treatments with various concentrations of PSAuNPs, as evaluated *via* ICP-MS (n = 4). * $p < 0.05$ *versus* the 50 μg/mL × 3 group.

3.2.3. *In vitro* photothermal capability

We next compared the photothermal effects of a single treatment and multiple treatments of MSCs with PSAuNPs by measuring the temperature rise after laser irradiation (660 nm, 0.5 W/cm^2) (Figure 3.5). The MSCs treated with a single dose of 50 μg/mL PSAuNPs exhibited temperature increase of 16 °C, after 100 sec of irradiation. Interestingly, the MSCs treated with 50 μg/mL PSAuNP × 3 exhibited rapid temperature increase of 43 °C. This result demonstrated that the MSC treatments with PSAuNPs three times significantly enhanced the photothermal capability compared to the single treatment, which is attributed to the increased intracellular loading of PSAuNPs due to the multiple treatments.

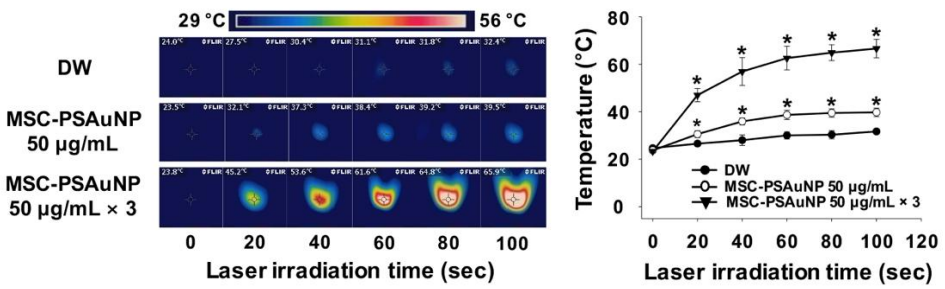

Figure 3.5. The photothermal effects of a single treatment and three consecutive treatments of MSCs with PSAuNPs. Temperatures were measured during laser irradiation (n = 5). * $p < 0.05$ *versus* any other group. DW indicates distilled water.

3.2.4. In vivo tumor-targeting effect and biodistributions of MSC-PSAuNP

We next investigated the tumor-targeting efficiency and the biodistributions of the MSC-PSAuNPs after intravenous administration to tumor-bearing mice. Tumors were generated *via* subcutaneous injection of human fibrosarcoma cell line (HT-1080 cells) to both flanks of athymic mice. After the tumors reached a proper volume, MSCs labeled with fluorescence were intravenously injected through tail vein. First, the biodistributions of MSCs and MSC-PSAuNPs in the tumor-bearing mice was examined using a real-time live imaging system at 1, 3, and 7 days post-injection (Figure 3.6A). No signal was detected in the PBS injection control group. In contrast, the MSC and MSC-PSAuNP injection groups showed clear fluorescent signals and exhibited similar distribution patterns. At 1 day post-injection, the fluorescent signals were detected in both tumor and normal tissues. The signals were strongly detected only in tumor regions at 3 days post-injection, and slightly decreased at 7 days post-injection. This result indicated that the number of MSCs or PSAuNP-laden MSCs in the tumor tissues reached a peak at 3 days post-injection. Furthermore, the tumor-tropic properties of MSCs were maintained even after MSCs were loaded with PSAuNPs.

Previous studies have demonstrated that MSCs preferentially migrate to tumor regions regardless of the tumor type.[47-49] The tumor tropism of MSCs involves interactions between the chemokines released from tumor tissues and the chemokine receptors expressed on the surfaces of MSCs. Tumor-secreted factors enhance the expression of CXC and CC receptors and activate growth factor receptors or toll-like receptors of MSCs.[42-46] MSCs then become more sensitized to chemoattractants, including CCL2,[42] CXCL8,[43] RANTES (CCL5),[44] PDGF-bb,[45]

IGF-1,[44] and VEGF[46], which are released from tumor tissues. These interactions between MSCs and tumor tissues increase the tumor-targeting efficiency of AuNPs in MSC-mediated AuNP delivery system.

Next, to qualitatively investigate the *in vivo* tumor-targeting efficiency, the AuNPs in tumor tissues were imaged using micro-CT at 3 days after intravenous injection of either PBS, cAuNPs, MSC-cAuNPs, PSAuNPs, or MSC-PSAuNPs (Figure 3.6B). The micro-CT analysis showed that the injection of MSC-PSAuNPs resulted in the accumulation of a higher amount of AuNPs in the tumor tissues compared to the other groups. Furthermore, the MSC-PSAuNP group showed even distribution of AuNPs within the tumor tissues. The improved intratumoral distribution of AuNPs facilitates the uniform temperature increases throughout the tumor tissues and consequently enhances the efficacy of photothermal cancer therapy.[40]

To investigate the biodistributions of the MSC-PSAuNPs following intravenous injection into tumor-bearing mice, the amount of AuNPs localized in the tumor tissues and major organs (spleen, liver, kidney, lung, heart, and brain) were determined using ICP-MS at 3 days post-injection (Figure 3.6C). All of the groups exhibited large amounts of AuNPs accumulated in the reticuloendothelial (spleen, liver, and lung) and urinary (kidney) systems, which is in accordance with the results of a previous study.[88] For the AuNP accumulation in the tumors, the MSC-PSAuNP group showed the highest tumor-targeting efficiency of 5.6 ± 2.1 % ID/g tumors, which was a 37-fold higher than that of the cAuNP group. The tumor-targeting efficiency of AuNPs in our MSC-PSAuNP system is even higher than that of a previous study (2 – 3 % ID) in which AuNPs were decorated with a tumor-targeting moiety (transferrin).[29] Furthermore, the tumor-targeting efficiency of the MSC-PSAuNP group was 6.8-fold and 5.7-fold higher than the MSC-cAuNP

group and the PSAuNP group, respectively. This result indicates that the tumor-targeting efficiency of AuNPs can be maximized when PSAuNPs and MSCs are applied together. The highest tumor-targeting efficiency of MSC-PSAuNPs is likely attributed to the tumor-tropic properties of MSCs and the prevention of AuNP exocytosis *via* forming PSAuNP aggregates. Taken together, the MSC-PSAuNP system significantly enhanced the tumor-targeting efficiency of AuNPs.

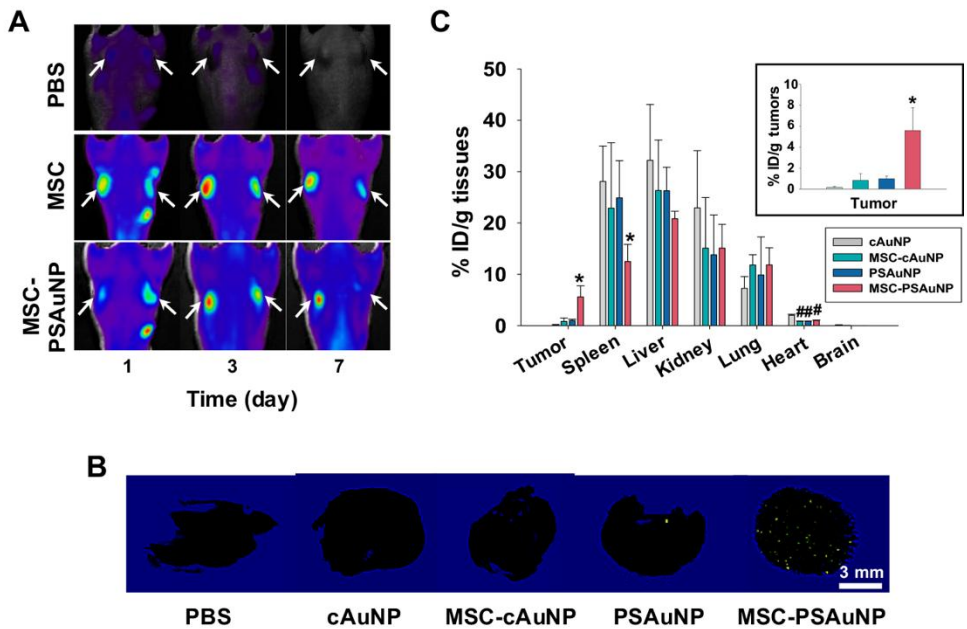

Figure 3.6. *In vivo* tumor-targeting and biodistributions of the AuNPs. (A) *In vivo* distribution of MSCs and MSC-PSAuNPs at various time points following intravenous injection into tumor-bearing mice. (B) Accumulation of AuNPs in the tumor 3 days after the intravenous injection, as evaluated *via* micro-CT imaging. Yellow indicates the AuNPs in the tumor. Scale bar = 3 mm. (C) Biodistributions of the AuNPs in the tumor tissues and major organs 3 days after intravenous injection of cAuNPs, MSC-cAuNPs, PSAuNPs, or MSC-PSAuNPs into tumor-bearing mice, as evaluated *via* ICP-MS (n = 3). * $p < 0.05$ *versus* any other group. $^{\#}$ $p < 0.05$ *versus* the cAuNP group.

3.2.5. *In vivo* photothermal efficiency

The photothermal efficiency of the MSC-PSAuNPs was examined in a tumor-bearing mouse model. As shown in Figure 3.7A, MSCs were treated with medium containing 50 μg/mL PSAuNPs or cAuNPs three times for 2 days each. After the tumor reached a diameter of 7 mm, the PSAuNP-laden MSCs were injected intravenously. As controls, PBS, cAuNPs, MSC-cAuNPs, or PSAuNPs were also injected. At 3 days post-injection, the tumors were irradiated with a 660 nm laser for 60 sec at a power density of 0.5 W/cm^2. Since the real-time infrared thermal imaging system measures the skin temperatures only, the temperatures in the tumor tissues would be higher than the recorded values. As shown in Figure 3.7B, the MSC-PSAuNP group exhibited the largest temperature increase of 23.3 °C. This result is likely attributed to the improved tumor-targeting efficiency and photothermal effect of AuNPs *via* tumor tropism of MSCs, formation of the AuNP aggregates in MSCs, and prevention of the AuNP exocytosis. Meanwhile, although laser irradiation in the PBS, MSC, cAuNP, and MSC-cAuNP groups induced comparable temperature increases of 13.4 – 15.3 °C, the PSAuNP group showed more temperature increase of 17.0 °C (Figure 3.7B). This result is likely attributed to the larger size of the PSAuNP aggregates compared to the cAuNP.

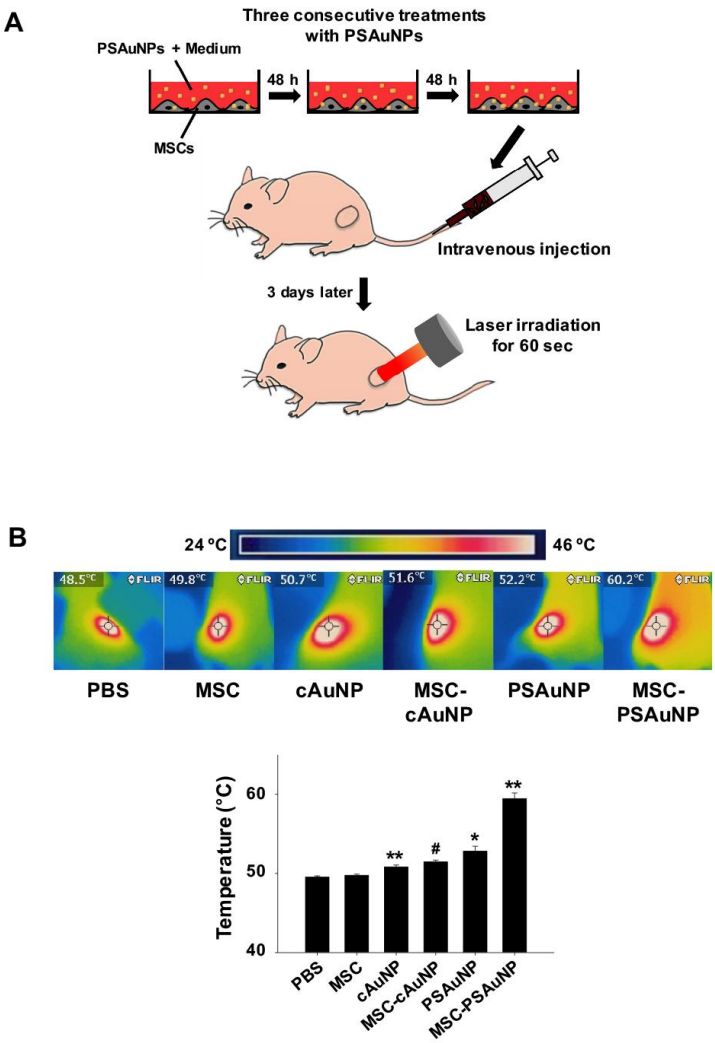

Figure 3.7. ***In vivo*** **photothermal efficiency.** (A) A schematic illustration of the photothermal cancer therapy using the MSC-PSAuNPs. The MSCs were treated three times with 50 μg/mL PSAuNPs for 2 days each and then intravenously injected into tumor-bearing mice. After 3 days, the tumors were exposed to NIR laser light for 60 sec under anesthesia. (B) Real-time infrared thermal images and temperature increases at the tumor sites after irradiation for 60 sec (n = 4). ** $p < 0.05$ *versus* any other group, * $p < 0.05$ *versus* any other group except the MSC-cAuNP group, $^{\#}p < 0.05$ *versus* any other group except the PSAuNP group.

3.2.6. *In vivo* photothermal cancer therapy

We next evaluated the *in vivo* anti-cancer therapeutic efficacy of the MSC-PSAuNPs. The tumor-bearing mice were randomly divided into 12 groups according to the intravenously injected material type (PBS, MSC, cAuNP, MSC-cAuNP, PSAuNP, or MSC-PSAuNP) with or without laser irradiation. At 3 days post-injection, a selection of the mice were exposed to laser irradiation for 60 sec (660 nm, 0.5 W/cm^2), and all of the mice were observed for 21 days (Figure 3.8A). The mice in the MSC-PSAuNP (L+) group exhibited scabs in the tumor region (Figure 3.8A) and an imperceptible tumor size at day 9 (Figure 3.8B). At day 21, no signs of tumor tissues were observed in most of the mice (Figure 3.8B). Compared to the MSC-PSAuNP (L+) group, the other irradiation groups showed 9.4- to 13.7-fold larger tumor volumes at day 21 (Figure 3.8B).

There is a controversy about the function of MSCs in tumor growth.[91] Previous studies have demonstrated that MSCs exhibited the anti-tumor effect by inhibiting angiogenesis[92] and inducing apoptosis of tumor cells in a cell number-dependent manner.[93] In contrast, the pro-tumor effect of MSCs was demonstrated in other studies.[94-95] MSCs promoted proliferation and metastasis of tumor cells in osteosarcoma[94] and colon carcinoma models.[95] In our study, the MSC (L-) group showed the comparable tumor growth to the PBS (L-) group (Figure 3.8B), which indicated that MSCs did not affect the tumor growth.

Histological analysis of the tumor tissues indicated that the PSAuNP (L+) and MSC-PSAuNP (L+) groups exhibited partial and nearly complete destruction of the tumor cells, respectively (Figure 3.8C). In the other group, cytotoxic damage was not observed. Meanwhile, photothermal cancer therapy may not cause tumor cell dispersion that encourages metastatic tumor repopulation at distal sites, as a

previous study reported that photothermal therapy slightly inhibited the metastatic tumor growth by releasing tumor-associated antigens and inducing the immunological responses.[96]

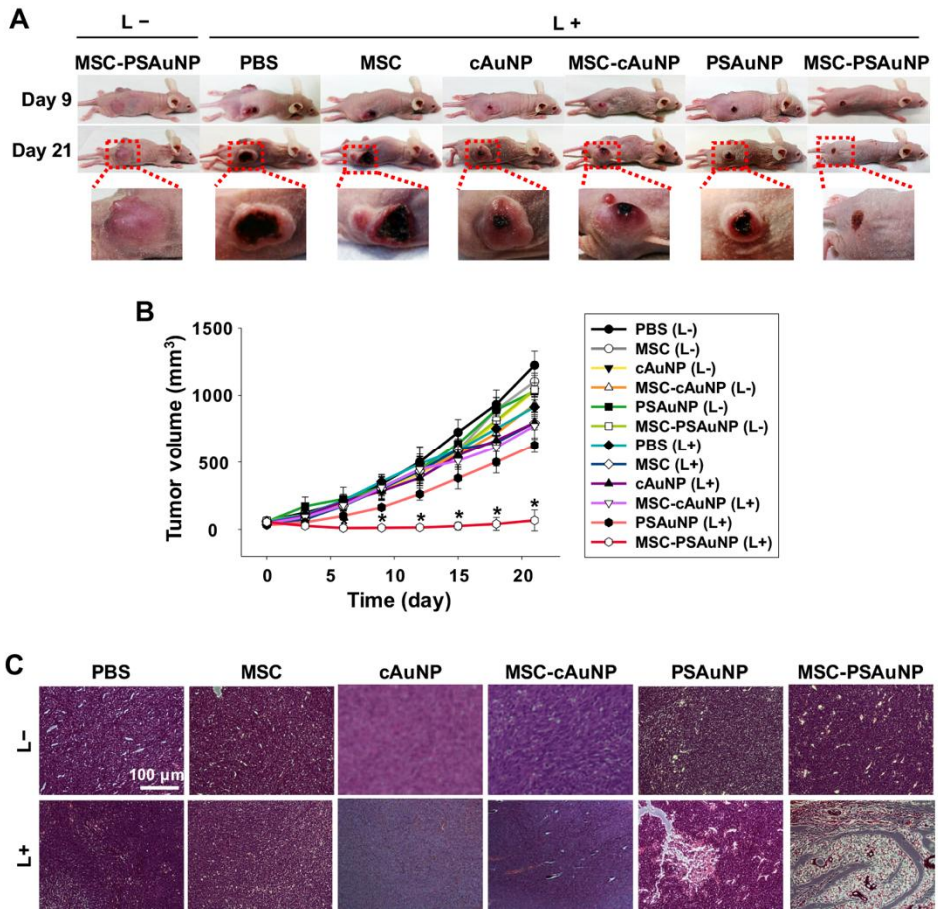

Figure 3.8. ***In vivo*** **photothermal therapeutic effects.** (A) Representative images of the laser irradiation groups and MSC-PSAuNP (L-) group at day 9 and 21. Magnified images indicate the tumor regions. (B) Volume profiles of each tumor tissue over 21 days after laser irradiation (n = 8). * $p < 0.05$ *versus* any other group. (C) Hematoxylin and eosin staining images of thin sections of the tumor tissues with or without irradiation at day 21. Scale bar = 100 μm.

Chapter 4.

Gold nanoparticle/graphene oxide hybrid sheets attached on mesenchymal stem cells for effective photothermal cancer therapy

4.1. Introduction

Tumor-tropic cell-mediated nanoparticle delivery has been investigated to improve the tumor-targeting efficiency of anti-cancer nanostructures. The underlying strategy in previous approaches was to internalize anti-cancer nanoparticles into tumor-tropic cells.[39,41,97-98] However, the intracellular nanoparticles can cause cytotoxicity and escape from the carrier cells *via* exocytosis, which lowers the efficiency of nanoparticle loading within cells.[55,87,99-100] In addition, the enhanced photothermal effect *via* plasmon coupling between AuNPs is hardly expected if the nanoparticles scattered within the cells.

Here, we report the effective photothermal cancer therapy using the tumor-tropic cells attaching AuNP-clustered sheets. MSCs were selected as AuNP delivery vehicles because they can be easily collected from patients and expanded *in vitro*.[50] We fabricated α-synuclein-coated gold nanoparticle and graphene oxide (AuNP/GO) hybrid sheets by adsorbing α-synuclein-coated AuNPs on both sides of micro-sized GO flakes. Alpha-synuclein is a member of intrinsically disordered proteins exerting high structural plasticity upon ligand interaction.[101] In our previous study, we demonstrated that AuNPs can be coated with α-synuclein using the unique interaction between AuNP surface and α-synuclein protein, and that the α-synuclein-coated AuNPs can be adsorbed in a monolayer on any substrates under an acidic condition.[102] Furthermore, there was no difference in the optical absorbance properties between bare AuNPs and α-synuclein-coated AuNPs.[102] Meanwhile, GO possesses hydrophobic domain and several functional groups, and adsorbs proteins *via* hydrophobic interactions, hydrogen bonding, and electrostatic interactions.[103-104] In the present study, AuNPs coated with α-synuclein were therefore effectively adsorbed on GO flakes. Previous studies have reported on the

AuNP/GO nanocomposites fabricated by irradiating the laser on the mixture of $HAuCl_4$ and GO or AuNPs and GO.[105-106] Those AuNP/GO nanocomposites showed improved photothermal capability compared to free $HAuCl_4$ or AuNPs upon the 532 nm laser irradiation. However, the AuNPs were not tightly packed on GO sheets and the absorption spectra of the AuNP/GO nanocomposites were not broadly red-shifted to the NIR region. In our study, by using α-synuclein-coated AuNPs of two different sizes, we were able to form more tightly packed AuNP layer on both sides of GO flakes, which can enhance the photothermal effect *via* strong plasmon coupling between AuNPs.

We hypothesized that dressing up MSCs with a cloak of AuNP-clustered sheet would avoid the cytotoxicity and exocytosis issues associated with intracellular nanoparticles, thereby enhancing the loading efficiency of nanoparticles in the cells, increasing the amount of tumor-targeted nanoparticles, and improving the anti-cancer efficacy (Figure 4.1). Furthermore, the AuNPs tightly arrayed in sheets would exhibit the enhanced photothermal effect by inducing plasmon coupling between the nanoparticles compared to AuNPs scattered within cells (Figure 4.1). To test this hypothesis, we examined the plasmonic photothermal capability of the AuNP/GO sheets upon the NIR laser irradiation. Then, we investigated whether the AuNP/GO sheets were stably attached on the MSC surface under shear stress conditions. The mechanisms involved in the adhesion of AuNP/GO sheets on the MSC membrane were also investigated. Next, we examined whether attaching AuNP/GO sheets on the MSC surface improved AuNP-loading efficiency in cells by attenuating cytotoxicity and removal of AuNPs from AuNP-MSC complexes compared to internalizing AuNPs into MSCs. Following intravenous injection of AuNP/GO sheet-attached MSCs (MSC-AuNP/GO sheet) or AuNP-internalized MSCs (MSC-AuNP) into tumor-

bearing mice, we compared the tumor-targeting efficiency of AuNPs, the photothermal effect, and their cancer ablation efficacy.

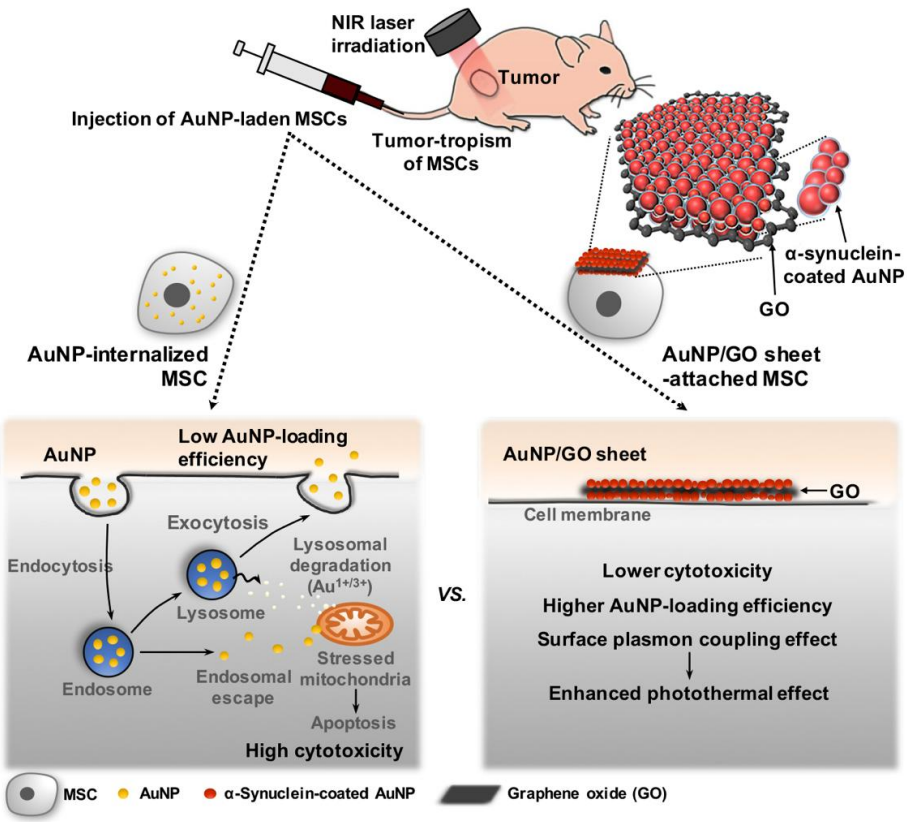

Figure 4.1. Schematic illustration of the improved photothermal therapeutic efficacy in cancer treatment by injection of tumor-tropic MSCs attaching AuNP/GO hybrid sheets. AuNP/GO sheets were prepared by adsorbing and tightly packing α-synuclein-coated AuNPs on both sides of micro-sized GO flakes. AuNP/GO sheets were stably attached to MSC surface. Compared to AuNPs internalized in MSCs, AuNP/GO sheets attached on MSCs exhibited enhanced photothermal capability *via* strong plasmon coupling between AuNPs. Furthermore, AuNP/GO sheets attached on MSC surface showed higher efficiency of AuNP loading in MSCs, which was ascribed to lower cytotoxicity and exocytosis prevention of AuNP/GO sheets. The cancer treatment strategy using MSC-AuNP/GO sheets enhanced the photothermal therapeutic efficacy by delivering larger amounts of AuNPs into tumor tissues and generating more heat upon NIR laser irradiation.

4.2. Results and discussion

4.2.1. Fabrication and characterization of AuNP/GO hybrid sheets

AuNPs coated with α-synuclein were prepared by incubating a mixture of 30 nm or 20 nm colloidal AuNPs and free α-synuclein in 20 mM MES buffer (pH 6.5) at 4 ^{o}C for 12 h.[102,107] After removing the residual α-synuclein by ultracentrifugation, homogeneous colloidal solutions of 20 nm or 30 nm AuNPs coated with α-synuclein were subjected to DLS analysis to verify their individual protein coats (Figure 4.2A). The hydrodynamic diameters of AuNPs increased from 30.2 to 47.1 nm ($AuNP_{30nm}$) and from 19.3 to 37.1 nm ($AuNP_{20nm}$) after coating with α-synuclein. About an 8.5 nm increase in the hydrodynamic radius for both cases indicated stable protein coating on the surfaces of AuNPs. The AuNP/GO sheets were then fabricated *via* two sequential steps of adsorbing α-synuclein-coated 30 nm and 20 nm AuNPs onto GO at pH 4.5. Before each step, sonication was done to produce a homogeneous complex. At the pH 4.5 condition, C-terminus and non-Aβ component (NAC) region of α-synuclein, which have a high plasticity and a pI value of 3.6, are negatively charged. Repulsive interaction between the negatively charged C-terminuses of α-synuclein is likely responsible for the formation of stable monolayer of α-synuclein-coated AuNPs on GO sheets. Scanning electron microscope (SEM) analysis of the resulting AuNP/GO sheet demonstrated that the AuNPs were tightly packed on the GO flake in a monolayer (Figure 4.2B). Transmission electron microscope (TEM) images of the AuNP/GO sheets revealed a trilayered structure with the tightly packed AuNP monolayers sandwiching the GO sheet on both sides (Figure 4.2C). Atomic force microscope (AFM) data showed that the AuNP/GO sheets had a thickness of ~ 60 nm, which is attributed to the two monolayers of α-synuclein-coated $AuNP_{30nm}$ (Figure 4.2D). Raman

spectrum of the AuNP/GO sheets showed clear D peak (~1350 cm^{-1}) and G peak (~1600 cm^{-1}), indicating that GO was successfully intercalated into the complex without any chemical damages or modifications (Figure 4.2E).

In contrast, AuNPs coated with other proteins, such as κ-casein, β-lactoglobulin, bovine serum albumin (BSA), and elastin, did not form a monolayer structure but produced agglomerates of AuNPs on GO sheets at pH 4.5 (Figure 4.3). This result is likely due to the low structural stability of other proteins on AuNPs. We confirmed that the fabrication of AuNP/GO sheet with a sandwich structure is achievable only through the adsorption property of α-synuclein.

AuNP/GO sheets consisting of heterogeneously sized (30 nm + 20 nm) AuNPs showed tighter packing of AuNPs compared to AuNP/GO sheets containing 30 nm AuNPs only (Figure 4.4A). The vacant sites between α-synuclein-coated 30 nm AuNPs on GO flake were occupied by additional adsorption of α-synuclein-coated 20 nm AuNPs. The tight packing of AuNPs on GO caused a significant red-shift in the maximum absorbance wavelength from 528 nm to 600 nm (Figure 4.4B) *via* strong plasmon coupling between AuNPs in AuNP/GO sheets (30 nm + 20 nm). Furthermore, the absorption spectra of AuNP/GO sheets fully expanded up to 900 nm, which made the *in vivo* photothermal treatment more feasible. There was a 41 % increase of the absorbance at 808 nm, the wavelength of NIR laser used in this study, in the AuNP/GO sheet (30 nm + 20 nm) compared to the AuNP/GO sheet (30 nm only) (Figure 4.4B). The photothermal effect of AuNP/GO sheets was evaluated by measuring the temperature rise after NIR laser irradiation (808 nm, 1.0 W/cm^2) for 5 min (Figure 4.4C). The AuNP/GO sheets consisting of heterogeneously sized (30 nm + 20 nm) AuNPs showed the highest temperature increase of 23.2 ℃, which was 3.9 ℃ higher than the AuNP/GO sheets containing 30 nm AuNPs only and 7.8 ℃ higher

than the physical mixture of bare AuNPs and GO. In accordance with the data in Figure 4.4B, the strongly red-shifted absorption spectra of AuNP/GO sheets (30 nm + 20 nm) group induced the highest heat generation upon the NIR laser irradiation. The bare and α-synuclein-coated AuNPs exhibited comparable temperature increases, which confirmed that coating AuNPs with α-synuclein caused negligible changes in the unique optical properties of AuNPs. Laser irradiation on micro-sized GO led to the slight temperature increase of 9.0 ºC.

In addition, we compared the packing density and absorption spectra of the AuNP/GO sheets (30 nm + 20 nm) to AuNP/GO sheets (30 nm + 5 nm or 30 nm + 10 nm). All of the AuNP/GO sheets exhibited the comparable packing density of AuNPs on GO surface (Figure 4.5A). However, the AuNP/GO sheets (30 nm + 20 nm) showed more red-shifted spectra of absorption compared to the other groups (Figure 4.5B). This result may be attributed to the exponential increase in the plasmon coupling intensity by increasing the sizes of AuNPs.[108] Thus, we selected the AuNP/GO sheets (30 nm + 20 nm) as an experimental group.

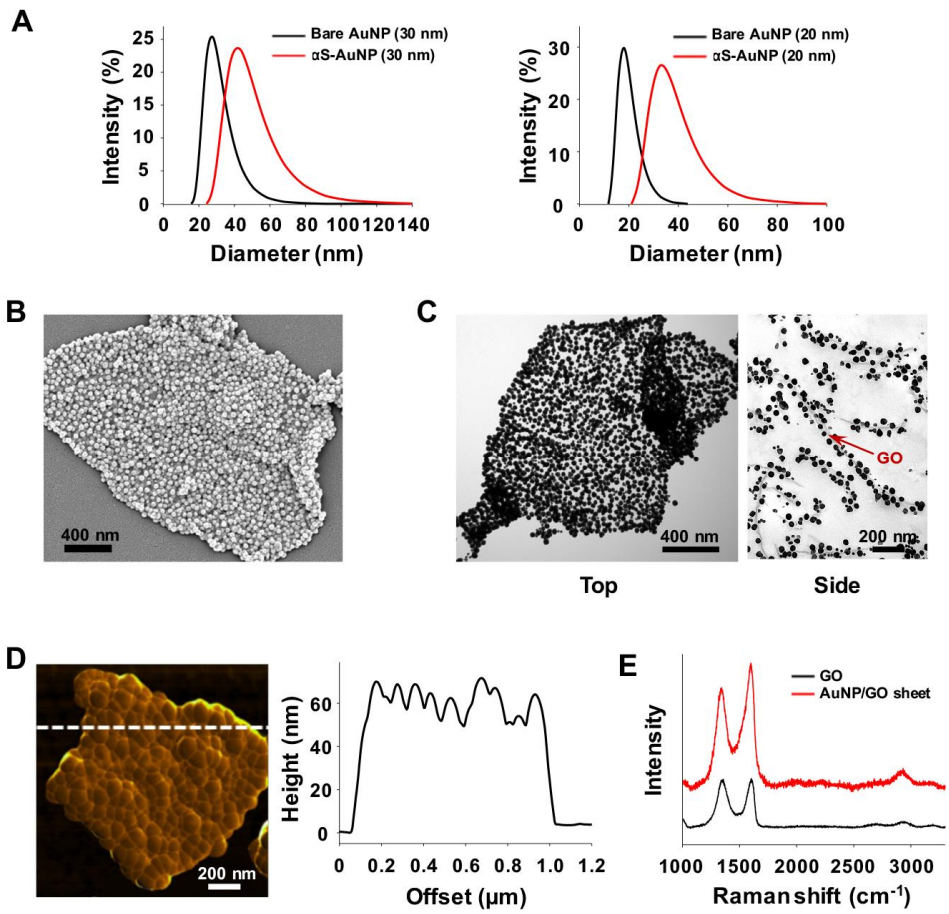

Figure 4.2. Characterization of α-synuclein-coated AuNPs and AuNP/GO hybrid sheets. (A) Hydrodynamic size of 30 nm (left) and 20 nm (right) AuNPs before and after α-synuclein encapsulation. αS-AuNP refers to AuNPs coated with α-synuclein. (B) SEM image of AuNP/GO hybrid sheet. (C) TEM images of the AuNP/GO sheet viewed from top and side. The 30 nm and 20 nm AuNPs coated with α-synuclein were absorbed on both sides of GO flakes. (D) AFM image of the AuNP/GO sheet and the height profile along the line shown in the AFM image. (E) Raman spectra of GO and AuNP/GO sheet.

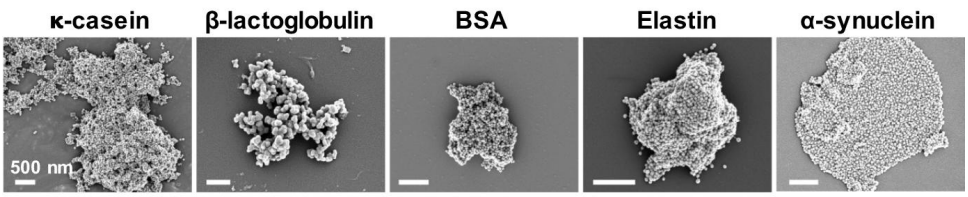

Figure 4.3. SEM images of composites consisting of different protein-coated AuNPs and GO sheet. The AuNPs were coated with κ–casein, β–lactoglobulin, bovine serum albumin (BSA), elastin, or α-synuclein. Scale bars = 500 nm.

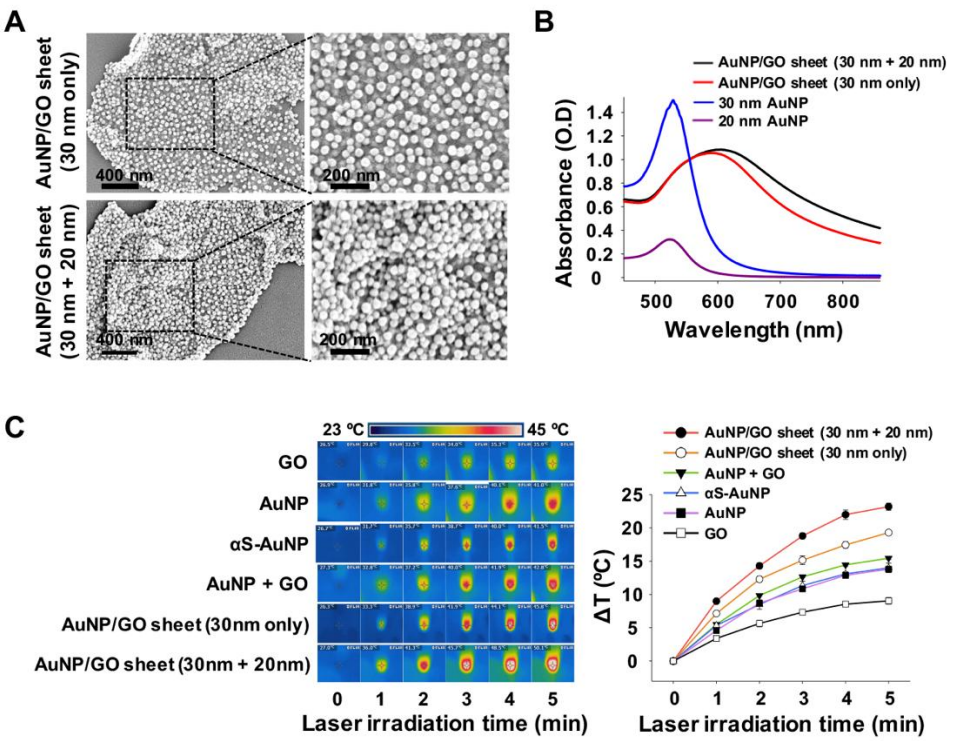

Figure 4.4. Enhanced photothermal effect of AuNP/GO hybrid sheets. (A) SEM images of AuNP/GO sheets consisting of 30 nm AuNPs only (top) and 30 nm + 20 nm AuNPs (bottom). (B) Absorption spectra of the colloidal solutions of bare AuNPs (20 nm and 30 nm) and AuNP/GO sheets (30 nm only and 30 nm + 20 nm). (C) Photothermal effects of GO, AuNP, α-synuclein-coated AuNP (αS-AuNP), AuNP + GO, AuNP/GO sheet (30 nm only), and AuNP/GO sheet (30 nm + 20 nm). Temperatures were monitored during 808 nm laser irradiation (n = 5).

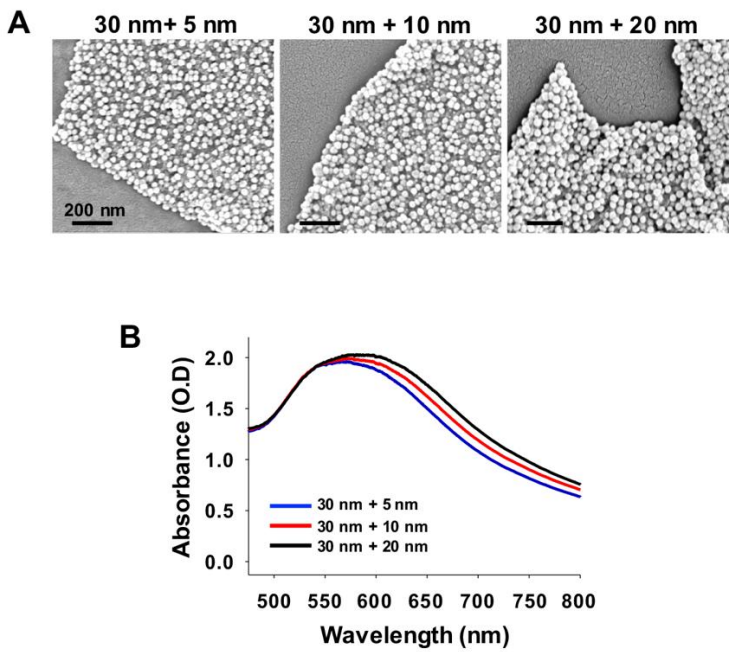

Figure 4.5. The effect of AuNP size on the optical property of AuNP/GO sheets. (A) SEM images and (B) absorption spectra of AuNP/GO sheets consisting of different sizes of AuNPs (30 nm + 5 nm, 30 nm + 10 nm, and 30 nm + 20 nm).

4.2.2. Adhesion of AuNP/GO sheets on the MSC surface

After treating AuNPs or AuNP/GO sheets with MSC culture for 1 day, we investigated the distribution of each material using TEM analysis (Figure 4.6A). When the MSCs were incubated with bare AuNPs (MSC-AuNP), the nanoparticles were internalized and located within the intracellular vesicles. However, in MSCs treated with AuNP/GO sheets (MSC-AuNP/GO sheet), most of the AuNP/GO sheets were detected on the cell surface (Figure 4.6A). The data indicated that AuNP/GO sheets (lateral size = 1.24 ± 0.48 μm) were preferably attached on the MSC surface rather than being internalized. As previously reported, the cellular distribution of GO is determined by its lateral dimensions.[57,62] Whereas nano-sized GO (20 – 500 nm) was internalized into cells,[57] the micro-scaled GO flakes (1 – 6 μm) were rarely incorporated into cells, but rather anchored on the cell surface.[62] We then assessed the stability of adhesion of AuNP/GO sheets on the MSC surface using fluorescence staining and SEM analysis. Cells circulating through blood vessels are subjected to the hemodynamic shear stress at a range of 0.5 ~ 30.0 dyn/cm^2.[109] We therefore exposed the MSC-AuNP/GO sheets to the highest shear force (30.0 dyn/cm^2). PKH67 staining of MSC membrane and rhodamine staining of AuNP/GO sheets demonstrated that the AuNP/GO sheets were still attached on the cell surface under the fluid shear stress (Figure 4.6B). The SEM images also confirmed that AuNP/GO sheets attached on the MSC surface were stable at physiological shear stress (Figure 4.6C).

The underlying mechanisms by which AuNP/GO sheets are attached on the MSC surface were investigated using western blot analysis. We examined the expression of integrin β1, the major adhesion-receptor, and fibronectin, the extracellular matrix (ECM) protein involved in cell adhesion.[110] First, we observed

fibronectin adsorption on AuNP/GO sheets using western blot analysis after incubating AuNP/GO sheets in serum-containing medium for 1 day (Figure 4.6D). Then, MSCs with or without AuNP/GO sheets were cultured on agar-coated plates with serum-free medium or serum-containing medium for 1 day to inhibit MSC adhesion on the culture plate. AuNP/GO sheets increased both integrin β1 expression and fibronectin presence in the MSCs only in serum-containing medium (Figure 4.6E). However, in serum-free medium, MSCs with AuNP/GO sheets did not show a significant increase in expression of integrin β1 and fibronectin (Figure 4.6E). These results indicated that AuNP/GO sheets adsorbed fibronectin from the serum-containing culture medium and were sequentially bound to MSCs *via* integrin β1. As the fibronectin – integrin β1 interactions affect the adhesion of AuNP/GO sheets on the MSC surface, trypsinization could detach the AuNP/GO sheets from MSCs. Therefore, in the following experiments, we detached MSCs, AuNP-internalized MSCs, and AuNP/GO sheet-attached MSCs from the culture plates by EDTA treatment.

Next, we quantitatively evaluated the distributions of AuNP/GO sheets on MSCs. The total and intracellular amounts of AuNPs were determined after collecting the AuNP/GO sheet-treated MSCs *via* EDTA treatment and trypsinization, respectively. The amount of AuNPs on the cell surface was calculated by subtracting the intracellular AuNP content from the total amount. We found that the ratios of cell surface-bound and internalized AuNPs to total content were 69.8 ± 0.10 % and 30.2 ± 0.07 %, respectively (Figure 4.6F). Although a small portion of AuNP/GO sheets was internalized into cells, most of them adhered on the cell surface.

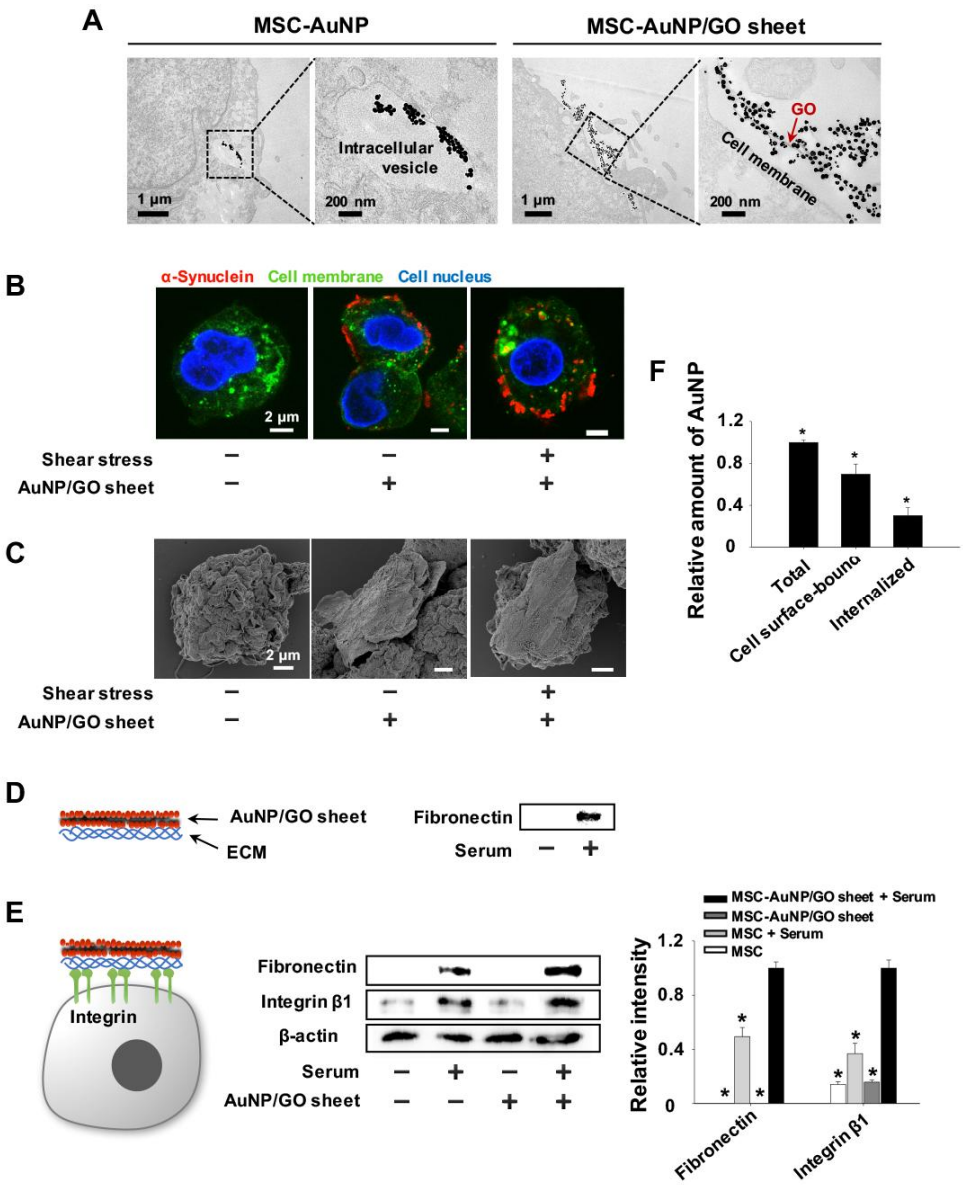

Figure 4.6. Adhesion of AuNP/GO sheets on the MSC surface. (A) TEM images of AuNPs internalized within the MSC and AuNP/GO sheets attached on MSC surface. (B) Stability of AuNP/GO sheets attached on MSCs, as evaluated by exposing the cells to shear stress and immunostaining for α-synuclein (red) in the AuNP/GO sheets. The cell

membrane and nucleus of MSC were stained with PKH67 (green) and DAPI (blue), respectively. (C) Stability of AuNP/GO sheets attached on MSCs, as evaluated by SEM. (D) Fibronectin adsorption on AuNP/GO sheets, as evaluated *via* western blot analysis (n = 4). (E) Molecules involved in the adhesion of AuNP/GO sheets on the MSC surface, as evaluated *via* western blotting for fibronectin and integrin β1 (n = 4). * $p < 0.05$ *versus* MSC-AuNP/GO sheets + Serum. (F) Extracellular and intracellular distributions of AuNP/GO sheets after interaction with MSCs. The total (= extracellular + intracellular) and intracellular amounts of AuNPs were determined using ICP-MS after collecting AuNP/GO sheet-treated MSCs *via* EDTA treatment and trypsinization, respectively (n = 4). * $p < 0.05$.

4.2.3. Cytotoxicity of AuNP/GO sheets

We examined the cytotoxicity of AuNP/GO sheets by evaluating cell viability and apoptotic gene expression after treating various concentrations of AuNP/GO sheets to MSC culture. For precise comparison, we defined the concentration of AuNPs or AuNP/GO sheets as AuNP weight per culture medium volume (w/v) in the following study. First, the cell viability was assessed using cell counting kit-8 (CCK-8). AuNPs at 100 μg/mL exhibited significant cytotoxicity, whereas AuNP/GO sheets at the same concentration did not (Figure 4.7A). The patterns for mRNA expression of caspase-3, a pro-apoptotic factor, were similar to results of the cell viability assay. AuNPs at 100 μg/mL increased caspase-3 expression, whereas AuNP/GO sheets at the same concentration did not (Figure 4.7B). In the live/dead staining, dead cells were readily detected in AuNPs at 100 μg/mL and higher concentrations and AuNP/GO sheets at 200 μg/mL (Figure 4.7C). In addition, we examined the cytotoxicity of AuNPs and AuNP/GO sheets at 50 μg/mL after 1 and 3 days of incubation. The number of caspase-3-positive cells was not significantly increased in both AuNP and AuNP/GO sheet groups compared to the no treatment group (Figure 4.7D). Furthermore, we performed a lactate dehydrogenase (LDH) assay to evaluate the cell membrane integrity. This assay measures the level of LDH, a cytosolic enzyme, released from the damaged cells.[111] MSCs treated with AuNPs or AuNP/GO sheets at 50 μg/mL for 1 and 3 days released negligible amounts of LDH compared to lysis positive control (Figure 4.7E). These results indicated that AuNPs and AuNP/GO sheets at 50 μg/mL caused no cytotoxicity and preserved the cell membrane integrity.

Although AuNP/GO sheets contained more materials (i.e., Au, α-synuclein, and GO) than bare AuNPs, we observed lower cytotoxicity in the AuNP/GO sheets.

This is likely due to the systemic difference between internalizing AuNPs within cells and attaching AuNP/GO sheets on cell surface. Previous studies have reported that the negatively charged AuNPs and gold ions within the cells induce apoptotic cell death in a dose-dependent manner.[87,99] When a large amount of negatively charged AuNPs, similar to the ones used in the present study, are internalized into cells, the stressed mitochondria release calcium ions to restore their membrane potential, causing calcium ion-induced apoptosis (Figure 4.1).[87] Furthermore, AuNPs internalized in the acidic lysosomes are ionized and released. These toxic ions ($Au^{1+/3+}$) inactivate the mitochondrial enzymes, depolarize the mitochondrial membrane potential, increase the reactive oxygen species levels and consequently activate the apoptosis pathway (Figure 4.1).[99] Since the maximum, non-cytotoxic, concentration for both AuNPs and AuNP/GO sheet groups was 50 μg Au/mL, we used the Au concentration of 50 μg/mL as 1× in the following experiments.

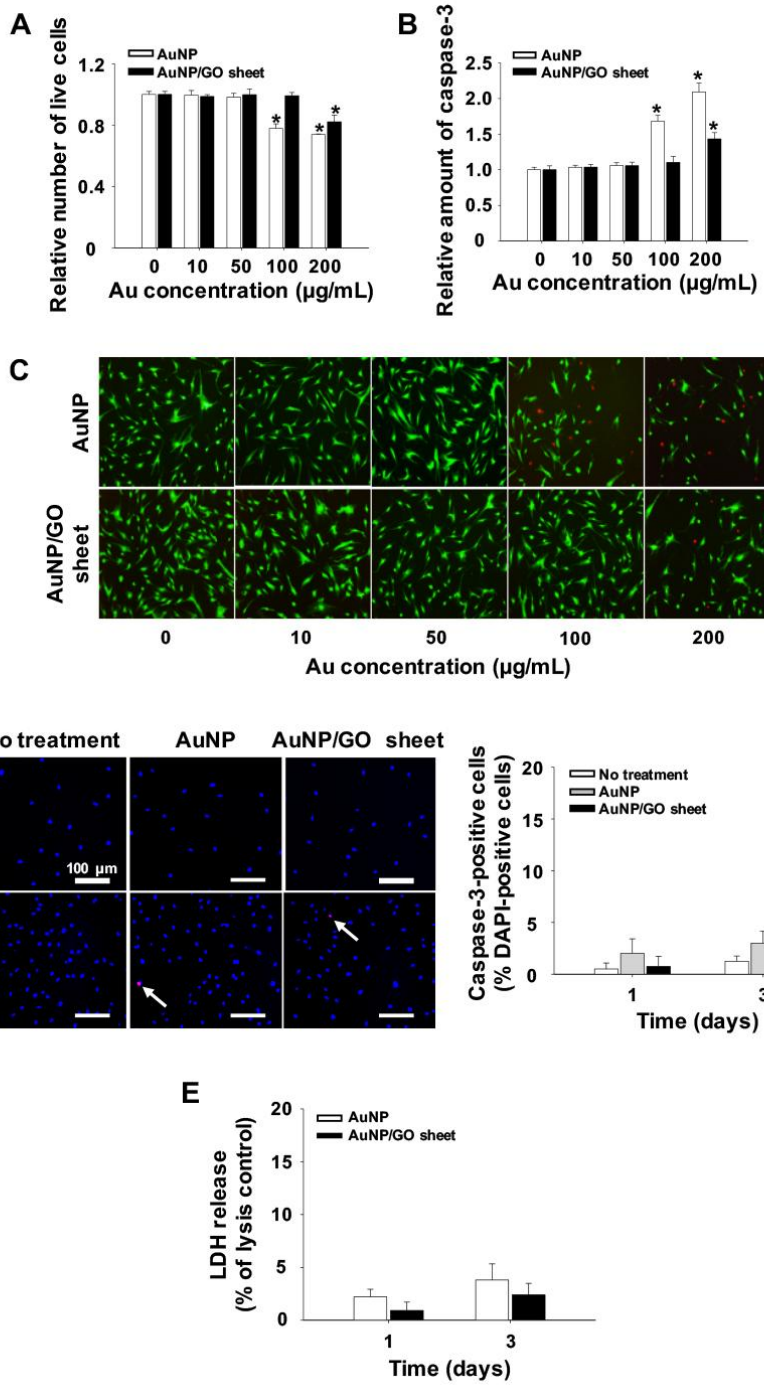
A
Relative number of live cells
AuNP
AuNP/GO sheet
1.2
0.8
0.4
0
0 10 50 100 200
Au concentration (μg/mL)
B
Relative amount of caspase-3
AuNP
AuNP/GO sheet
2.5
2.0
1.5
1.0
0.5
0
0 10 50 100 200
Au concentration (μg/mL)
C
AuNP
AuNP/GO sheet
0 10 50 100 200
Au concentration (μg/mL)
D
No treatment
AuNP
AuNP/GO sheet
Day 1
Day 3
100 μm
Caspase-3-positive cells
(% DAPI-positive cells)
No treatment
AuNP
AuNP/GO sheet
20
15
10
5
0
1 3
Time (days)
E
LDH release
(% of lysis control)
AuNP
AuNP/GO sheet
20
15
10
5
0
1 3
Time (days)

Figure 4.7. Cytotoxicity of AuNP/GO sheets. (A) Viability of MSCs cultured with various Au concentrations of AuNPs or AuNP/GO sheets for 1 day, as evaluated *via* the cell counting kit-8 assay (n = 4). * $p < 0.05$ *versus* no treatment group. (B) Apoptotic activity of MSCs after treatment with various Au concentrations of AuNPs or AuNP/GO sheets for 1 day, as evaluated *via* qRT-PCR for an apoptotic marker, caspase-3 (n = 4). * $p < 0.05$ *versus* no treatment group. (C) Fluorescence images of MSCs stained with a live/dead assay kit after AuNP or AuNP/GO sheet treatment at various Au concentrations for 1 day. Green and red indicate viable and dead cells, respectively. (D) Cytotoxicity of AuNPs or AuNP/GO sheets at 50 μg/mL after 1 and 3 days of incubation, as evaluated *via* immunocytochemical staining against caspase-3 (red). The cell nuclei were stained with DAPI (blue). Scale bars = 100 μm. (E) Cytotoxicity of AuNPs or AuNP/GO sheets at 50 μg/mL after 1 and 3 days of incubation, as evaluated *via* LDH assay (n = 4).

4.2.4. AuNP-loading efficiency and photothermal capability

The loading amount of AuNPs onto cells was quantitatively evaluated using ICP-MS after MSCs were treated with AuNPs or AuNP/GO sheets for 1 day. The MSCs treated with AuNP/GO sheet 1× showed a 3.4-fold higher AuNP-loading efficiency than the AuNP 1× group (Figure 4.8A). The AuNP amount in the AuNP/GO sheet 0.25× group was nearly identical to that of the AuNP 1× group (Figure 4.8A). These results indicate that attaching AuNP/GO sheets on the cell surface is a more efficient approach for AuNP loading than internalizing AuNPs into cells in tumor-tropic cell-mediated nanoparticle delivery. Furthermore, a considerable portion of endocytosed AuNPs escapes from the cells *via* exocytosis, which consequently lowers the intracellular AuNP content.[55] To quantify the AuNPs removed from the AuNP-MSC complexes, we assessed the removal kinetics of AuNPs as described previously.[55] At 72 h, the fraction of removed AuNPs in the AuNP group (27.3 %) was significantly higher than that in the AuNP/GO sheet group (11.7 %) (Figure 4.8B).

Next, we examined the photothermal effect of MSCs treated with AuNPs or AuNP/GO sheets. The temperature rise was monitored after irradiating the samples with an NIR laser (808 nm, 1.0 W/cm^2) for 5 min. MSCs treated with the same concentration (50 μg Au/mL, 1×) of AuNPs and AuNP/GO sheets showed temperature increases of 19.6 ºC and 35.4 ºC, respectively (Figure 4.8C). The higher temperature rise in the MSC-AuNP/GO sheet 1× group was attributed to the larger AuNP content in the cells and the extensive plasmon coupling between AuNPs in the AuNP-clustered sheets. Furthermore, the MSC-AuNP/GO sheet 0.25× group exhibited a 5.5 ºC higher temperature increase than the MSC-AuNP 1× group, although both groups contained the same amount of AuNPs. This result

was ascribed to the enhanced photothermal capability *via* plasmon coupling between AuNPs in the MSC-AuNP/GO sheet 0.25× group as compared to AuNPs scattered within MSCs in the MSC-AuNP 1× group.

We examined the stability of AuNP/GO sheets in serum-containing medium and human plasma. After incubating AuNP/GO sheets in culture medium or plasma at 37 ºC, the amounts of detached AuNPs were quantified using ICP-MS over time. In both serum-containing medium and human plasma, approximately 30 % of AuNPs were released from the GO sheets after 72 h of incubation (Figure 4.9A). Interestingly, a large portion of the detached AuNPs was released during the initial 6 h of incubation, and afterward, the profiles of AuNP detachment reached a steady state (Figure 4.9A). This result is likely due to heterogeneity in the strength of interaction between α-synuclein-coated AuNPs and GO sheets. The AuNPs weakly bound on GO sheets were detached from GO during 1 day of the *in vitro* incubation of MSCs with AuNP/GO sheets, and approximately 70 % of AuNPs remained attached to the GO sheets. Therefore, the AuNPs would be stably attached to the surface of GO sheets after MSC-AuNP/GO sheets were intravenously injected into tumor-bearing mice. In addition, we assessed the photothermal effect of AuNP/GO sheets upon laser irradiation following incubation for 24 h in serum-containing medium or distilled water (DW). AuNP/GO sheets incubated in serum-containing medium showed a slight temperature decrease of 1.8 ºC compared to AuNP/GO sheets in DW (Figure 4.9B), which is likely due to the small amount of AuNPs detached from GO sheets in biological fluids (Figure 4.9A).

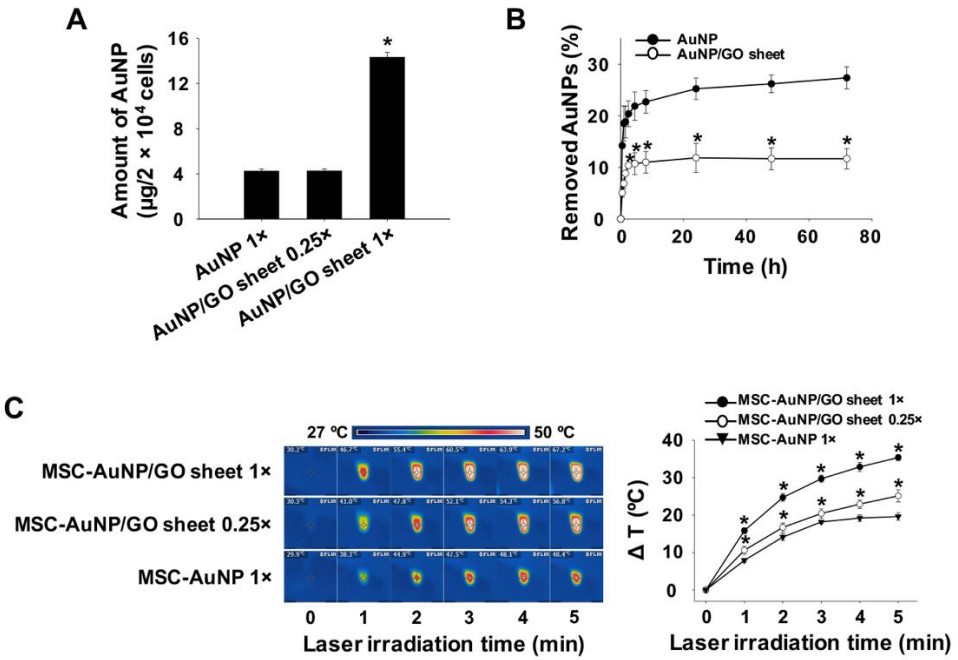

Figure 4.8. AuNP-loading efficiency and photothermal effect of MSC-AuNP/GO sheets. (A) AuNP amounts in MSCs treated with AuNPs (50 μg Au/mL, 1x) or AuNP/GO sheets (50 μg Au/mL, 1x and 12.5 μg Au/mL, 0.25x) for 1 day, as evaluated *via* ICP-MS (n = 4). * $p < 0.05$. (B) Time profiles of AuNP removal from the AuNP-MSC complexes. MSCs were treated with the same concentration of AuNPs or AuNP/GO sheets for 1 day and then washed with PBS to eliminate the unloaded particles. After replenishing with fresh media, the amount of AuNPs loaded in cells was determined with ICP-MS over time to evaluate the removed AuNPs (n = 4). * $p < 0.05$. (C) Temperature profiles of MSCs treated with AuNPs or AuNP/GO sheets during NIR laser irradiations (n = 5). * $p < 0.05$.

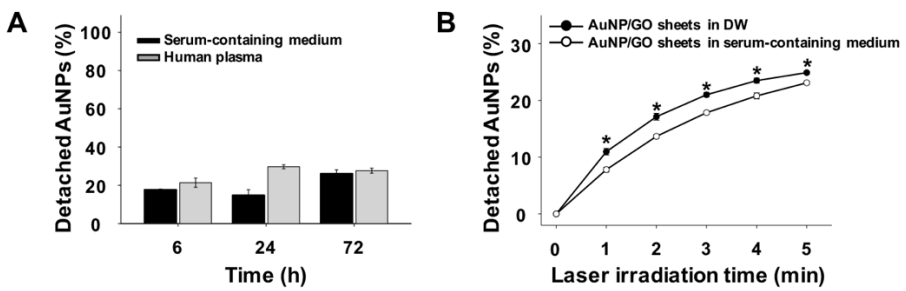

Figure 4.9. Stability of AuNP/GO sheets in biological fluids (serum-containing medium and human plasma). AuNP/GO hybrid sheets were incubated in serum-containing medium or human plasma at 37 ºC. (A) The amount of AuNPs released from the GO sheets was determined with ICP-MS over time (n = 4). (B) Photothermal effect of AuNP/GO sheets after incubation for 24 h in serum-containing medium or distilled water (DW). Temperatures were monitored during laser irradiation (808 nm, 1 W/cm^2) (n = 4). * $p < 0.05$.

4.2.5. *In vitro* tumor-tropism

We investigated whether attaching AuNP/GO sheets on the MSC surface affected the tumor-tropism of the MSCs. Tumor spheroids were formed using 4′-6-diamidino-2-phenylindole (DAPI)-labeled human fibrosarcoma cell line (HT-1080 cells) and cultured for 2 days. Next, human dermal fibroblasts, MSCs, MSC-AuNPs, or MSC-AuNP/GO sheets, in which cells were labeled with DiI, were co-cultured with the tumor spheroids on agar-coated plates. As dermal fibroblasts showed no response to the tumor environments, the cells clustered together and stuck around the spheroids (Figure 4.10). However, the tumor-tropic MSCs extensively infiltrated into the tumor spheroids (Figure 4.10). The AuNP-internalized MSCs and AuNP/GO sheet-attached MSCs also migrated into the spheroids and exhibited homogeneous intratumoral distribution (Figure 4.10). This result indicates that MSCs treated with AuNPs or AuNP/GO sheets still retain their tumor-tropic property.

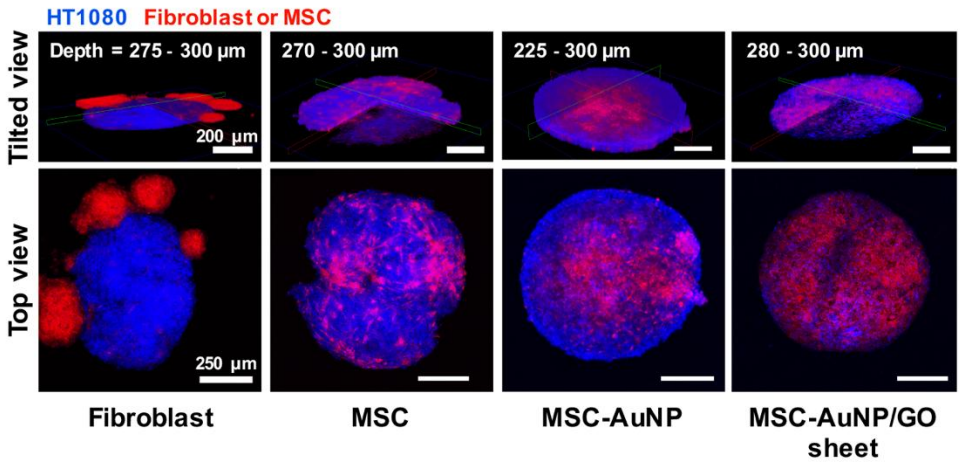

Figure 4.10. ***In vitro*** **tumor-tropic property of AuNP/GO sheet-attached MSCs, as evaluated with fluorescence straining.** DAPI (blue)-labeled tumor spheroids were cocultured with DiI (red)-labeled dermal fibroblasts, MSCs, AuNP-internalized MSCs, or AuNP/GO sheet-attached MSCs on agar-coated plates for 1 day. (Top) Three-dimensionally reconstructed images of samples from confocal z-stack images taken at the indicated distance from the base. The height of samples ≈ 600 μm. (Bottom) Three-dimensionally stacked images of whole samples.

4.2.6. *In vivo* tumor-targeting efficiency of MSC-AuNP/GO sheets

A previous study demonstrated that intravenously injected MSCs are maximally accumulated in the tumor tissues at 3 days post-injection.[98] Thus, the *in vivo* tumor-targeting efficiency and biodistribution of AuNP/GO sheet-attached MSCs were assessed at 3 days post-injection. First, tumor-targeting effect was evaluated using real-time live imaging. Tumors were generated by subcutaneously injecting HT-1080 cells to the right flanks of athymic mice. After the tumors reached the desired volume, fluorescence-labeled MSCs were intravenously administered through the tail vein. At 3 days post-injection, no signals were detected in the phosphate buffered saline (PBS) injection group (Figure 4.11A). However, the MSC, MSC-AuNP 1×, MSC-AuNP/GO sheet 0.25×, and MSC-AuNP/GO sheet 1× injection groups showed strong signals in the tumor regions (Figure 4.11A). We confirmed that the tumor-tropic property of MSC was preserved even after AuNP/GO sheets were attached on the MSC surface.

The tumor-tropism of MSCs involves a paracrine signaling loop between tumor tissues and MSCs.[42-44,46,112] Tumor tissues secrete various cytokines and growth factors to survive. The tumor-secreted factors, such as stromal cell-derived factor-1 (SDF-1),[112] interleukin-8 (IL-8),[43] CCL2,[42] CCL5,[44] and vascular endothelial growth factor (VEGF),[46] stimulate the expression of the corresponding receptors on MSCs in a positive-feedback manner, which sensitizes the MSCs to chemoattractants. These chemotactic responses between tumor tissues and MSCs facilitate the tumor-tropism of MSCs.

To quantitatively evaluate the biodistribution of MSC-AuNP/GO sheets in tumor-bearing mice, the amount of AuNPs localized in major organs (spleen, liver, kidney, lung, heart, and stomach), blood, and tumor tissues were determined at 3

days post-injection. All groups showed a similar biodistribution pattern in that a large amount of AuNPs were detected in the reticuloendothelial system (spleen and liver) (Figure 4.11B), which is in accordance with previous studies.[113-114] In tumor tissues, the MSC-AuNP/GO sheet 1× group exhibited the highest AuNP accumulation of 41.1 μg Au/g tumor, which is 3.6 and 4.5-fold higher than the MSC-AuNP/GO sheet 0.25× group and MSC-AuNP 1× group, respectively (Figure 4.11C). Although MSCs were treated with the same Au concentration (1×) for AuNPs and AuNP/GO sheets, AuNP/GO sheet-attached MSCs delivered much larger amounts of AuNPs into tumor tissues, which was ascribed to the higher AuNP-loading efficiency (Figure 4.8A) and less AuNP removal (Figure 4.8B) compared to AuNP-internalized MSCs.

Regarding the biodistribution of intravenously administered micro-sized AuNP/GO sheets, a previous study reported that intravenously injected, micro-sized GOs exhibited slow clearance from the body and remained in liver, spleen, and kidney.[115] Nevertheless, a low dose (100 μg/mouse) of GO caused no significant cytotoxicity with normal organ functions at 1 month.[115] In our study, the amount of micro-sized GO intravenously administered into a mouse is only 7.6 μg in the MSC-AuNP/GO sheet 1× group. Therefore, the AuNP/GO sheets may stay in liver, spleen and kidney with no toxicity.

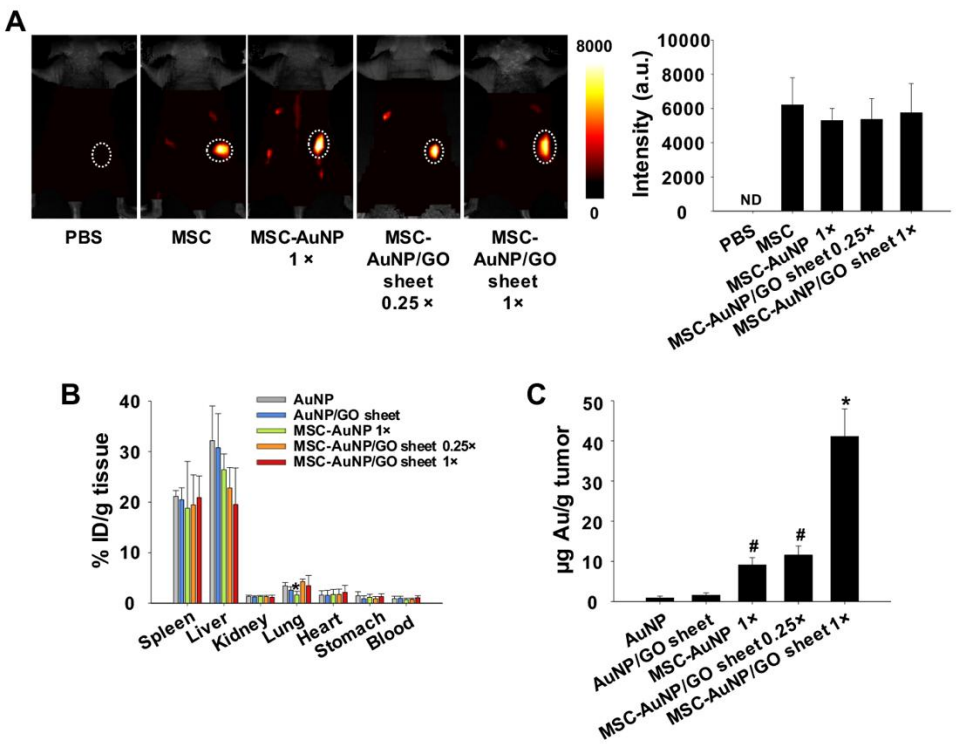

Figure 4.11. ***In vivo*** **tumor-targeting efficiency of MSC-AuNP/GO sheets.** (A) *In vivo* distribution of MSCs, MSC-AuNPs 1×, MSC-AuNP/GO sheets 0.25×, and MSC-AuNP/GO sheets 1× at 3 days after intravenous injection into tumor-bearing mice. Prior to injection, MSCs were fluorescence-labeled. The dotted circles indicate tumors. (B) Biodistributions of AuNPs in major organs and blood, and (C) AuNP content in the tumor tissues 3 days after intravenous injection of AuNP, AuNP/GO sheet, MSC-AuNP 1×, MSC-AuNP/GO sheet 0.25×, and AuNP/GO sheet 1× into tumor-bearing mice, as evaluated *via* ICP-MS (n = 4). * $p < 0.05$ *versus* any other group. # $p < 0.05$ *versus* AuNP and AuNP/GO sheet groups.

4.2.7. *In vivo* photothermal effect

We examined the *in vivo* photothermal efficacy of the MSC-AuNP/GO sheet. MSCs were treated with AuNP/GO sheets for 1 day and collected following EDTA treatment. The samples were then intravenously injected into tumor-bearing mice. At 3 days post-injection, tumors were irradiated with the NIR laser (808 nm, 1.5 W/cm^2) for 5 min and the temperature increases were recorded using a real-time infrared thermal imaging system. The MSC-AuNP/GO sheet 1× group showed the highest temperature increase to 58.0 ºC (Figure 4.12), which is sufficient to cause irreversible cell damage and death.[2] This result was likely due to the largest amount of AuNPs accumulated in tumor tissues and the improved plasmon coupling between AuNPs in AuNP/GO sheets of the MSC-AuNP/GO sheet 1× group. Compared to the MSC-AuNP 1× group, the MSC-AuNP/GO sheet 0.25× group exhibited a 5.4 ºC higher temperature increase (Figure 4.12). Although both groups delivered the comparable amount of AuNPs to tumor tissues, the red-shifted absorption spectrum of AuNP/GO sheets (Figure 4.4B) induced this difference in temperature increase. Meanwhile, laser irradiation in the AuNP/GO sheet, AuNP, MSC, and PBS groups caused moderate temperature increases of 9.5 – 11.9 ºC (Figure 4.12).

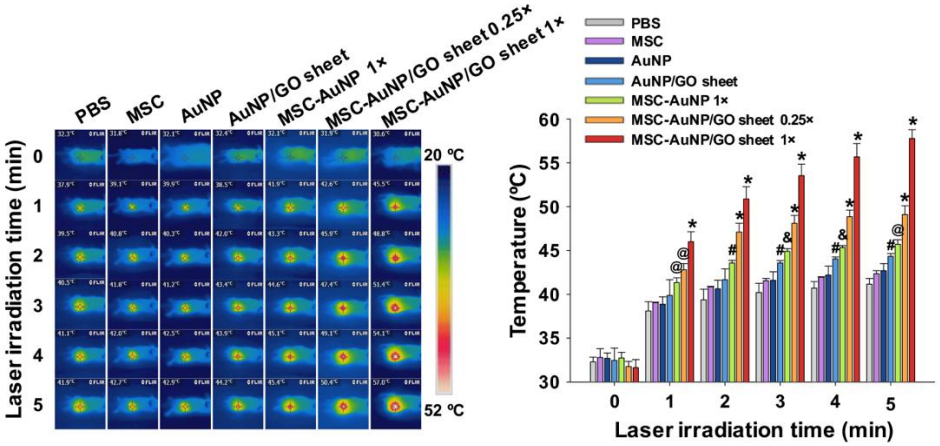

Figure 4.12. ***In vivo*** **photothermal efficiency, as evaluated** ***via*** **real-time infrared thermal images and temperature increases at the tumor sites during laser irradiation for 5 min (n = 4).** Three days after intravenous injection of samples into tumor-bearing mice, the tumors were exposed to NIR laser irradiation for 5 min under anesthesia. * $p < 0.05$ *versus* any other group, # $p < 0.05$ *versus* PBS and MSC groups, $^{@}p < 0.05$ *versus* PBS, MSC, and AuNP groups, and $^{\&}p < 0.05$ *versus* PBS, MSC, AuNP, and AuNP/GO sheet groups.

4.2.8. *In vivo* tumor ablation efficacy

We further examined the *in vivo* photothermal therapeutic efficacy of AuNP/GO sheet-attached MSCs. After randomly dividing the tumor-bearing mice into 8 groups (PBS with or without laser irradiation, MSC, AuNP, AuNP/GO sheet, MSC-AuNP 1×, MSC-AuNP/GO sheet 0.25×, and MSC-AuNP/GO sheet 1× with laser irradiation), we intravenously injected the samples through the tail vein. Three days post-injection, the tumor regions were irradiated with the NIR laser (808 nm, 1.5 W/cm^2) for 5 min except the PBS (L−) group. The anti-cancer effect was evaluated for the following 21 days. As shown in Figure 4.13A, only mice belonging to the MSC-AuNP/GO sheet 1× (L+) group showed a superficial scab in the tumor region and indiscernible tumor volume. In accordance with these images, the MSC-AuNP/GO sheet 1× (L+) group clearly showed the suppression of tumor growth over the 21-day evaluation period (Figure 4.13B). The tumor volume of the MSC-AuNP/GO sheet 0.25× (L+) group was less than a half of that of the PBS (L−) group at 21 days (Figure 4.13B). The other laser irradiated groups, except the MSC-AuNP/GO sheet 1× (L+) and 0.25× (L+) groups, exhibited no significant differences compared to the PBS (L−) group with regards to the tumor volume. For histological analysis, the sections of tumor tissues were stained with hematoxylin and eosin. The MSC-AuNP/GO sheet 1× (L+) group showed extensive coagulative necrosis including karyorrhectic nuclear fragments, whereas the other groups exhibited partial or no destruction of tumor cells (Figure 4.13C).

Clinical trials of photothermal therapy have been progressed in patients with lung, head and neck tumors.[116] These studies employed gold nanoshells and optical fibers as photothermal agents and external light source, respectively. Although the penetration depth of NIR laser is limited, the optical fibers make the

photothermal therapy applicable to deep tumors. As MSC-AuNP/GO sheets exhibit remarkable photo- thermal capability and tumor-targeting effect, MSC-AuNP/GO sheets may provide an effective platform for clinical cancer therapy.

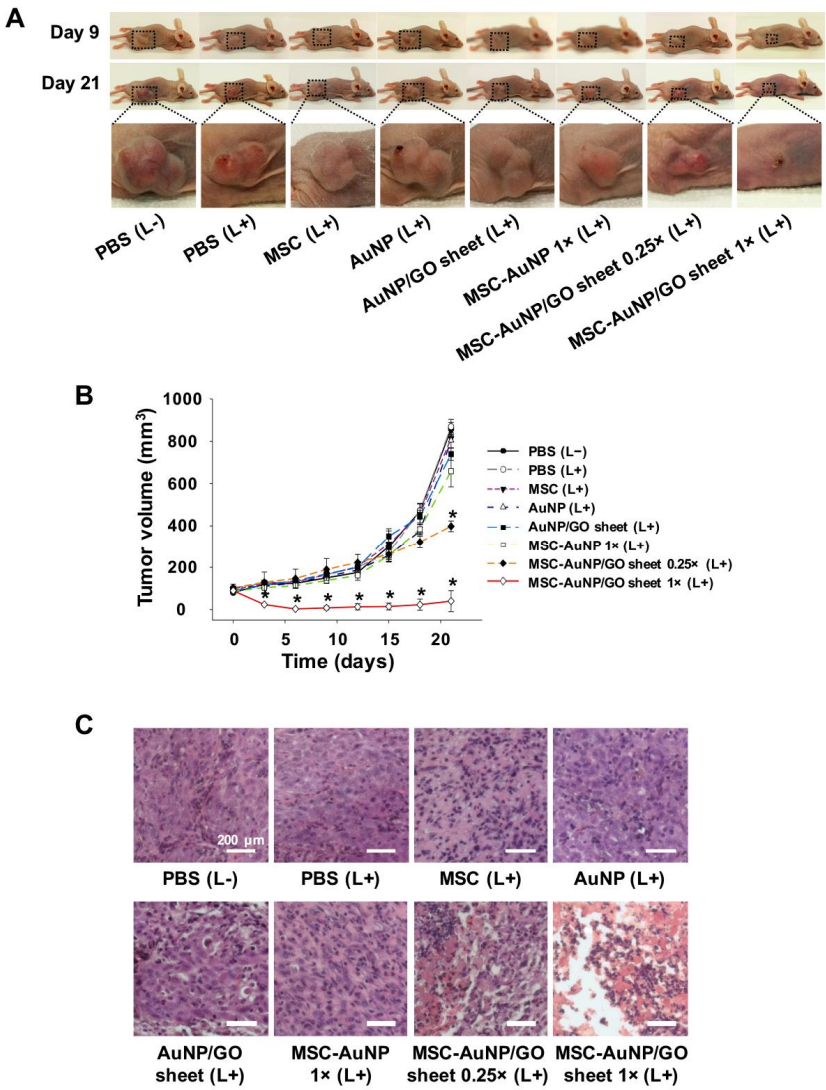

Figure 4.13. ***In vivo*** **tumor ablation efficacy.** (A) Representative mouse images of the laser irradiation groups and PBS (L−) group on day 9 and 21 after laser irradiation. Square boxes indicate the tumor regions. L+ refers to laser irradiation and L− refers to no laser irradiation. (B) Volume profiles of each tumor tissue over 21 days after laser irradiation (n = 5). Tumor tissues were irradiated with the NIR laser on day 0. * $p < 0.05$ *versus* any other group. (C) Hematoxylin and eosin staining images of thin sections of the tumor tissues at day 1. Scale bars = 200 μm.

Chapter 5.

Conclusions and future studies

This thesis presents the studies on applying tumor-tropic mesenchymal stem cells (MSCs) as a carrier for tumor-targeted delivery of gold nanoparticles (AuNPs) for effective photothermal cancer therapy.

Chapter 3 demonstrates that the tumor-targeting efficiency and photothermal effect of AuNP-mediated anti-cancer therapy can be greatly improved by employing PSAuNPs and MSCs. PSAuNPs loaded into MSCs cluster together likely in acidic endosomes. We show that PSAuNP-laden MSCs delivered AuNPs at a high efficiency (5.6 % ID/g tumors) to targeted tumor tissues due to the tumor-tropic properties of MSCs and the prevention of the exocytosis of large PSAuNP aggregates. The high tumor-targeting efficiency and the large PSAuNP aggregates led to a dramatically enhanced photothermal efficiency and increased anti-cancer therapeutic efficacy upon NIR laser irradiation on tumor-bearing mice.

Chapter 4 shows that AuNP/GO sheet-attached MSCs can effectively deliver a large amount of AuNPs into tumor tissues and induce high localized heat upon laser irradiation, resulting in improved photothermal therapeutic efficacy. AuNP/GO sheets were fabricated by coating two different sizes of AuNPs with α-synuclein protein and subsequently adsorbing onto micro-sized GO flakes. AuNP/GO sheets exhibited enhanced photothermal capability upon NIR laser irradiation compared to bare AuNPs, which was likely due to strong plasmon coupling between the AuNPs tightly packed in AuNP/GO sheets. AuNP/GO sheets stably adhered onto the MSC surface *via* integrin β1. AuNP/GO sheets attached on MSC carriers showed higher AuNP-loading efficiency in cells, which was attributed to lower cytotoxicity and AuNP removal from the AuNP-MSC complexes compared to AuNPs internalized into MSCs. When intravenously injected into tumor-bearing mice, AuNP/GO sheet-attached MSCs dramatically improve the tumor ablation efficacy by increasing the AuNP contents in tumor

tissues and improving the photothermal effect. This study demonstrates that delivering photothermal agents by attaching on tumor-tropic cells in the form of clustered sheets can improve photothermal therapeutic effect, which can be extended to delivery of other anti-cancer agents to tumor tissues.

The results described in this thesis collectively demonstrate that the combination of tumor-tropic MSCs and functionalized AuNPs as tumor-targeting carriers and photothermal agents, respectively, can improve the photothermal therapeutic efficacy by increasing the tumor-targeting efficiency and photothermal capability of AuNPs. The MSC-mediated nanoparticle delivery system can be further modified to maximize the tumor-targeting efficiency of nanoparticles. The tumor-tropic property of MSCs could be further fortified by inserting tumor-targeting moieties conjugated with hydrophobic chains into the plasma membrane or transfecting genes that encode tumor-targeting proteins. For the MSC-AuNP/GO sheet strategy, the α-synuclein protein could be recombined with tumor-targeting peptides such as RGD (Arg – Gly – Asp) and NGR (Asn – Gly – Arg). As hybrid sheets consisting of AuNPs coated with modified α-synuclein and GO flakes are likely to adhere to MSC surface, the tumor-targeting peptides would be exposed to tumor microenvironment, thus further increasing the tumor-targeting efficiency of nanoparticles.

Photothermal therapy can be combined with immunotherapy to eradicate both primary and metastatic cancers in a synergistic manner. A previous study has demonstrated that the combination of photothermal therapy and anti-CTLA-4 antibody therapy effectively eliminates primary tumor and prevents the progression of metastasis.[117] Photothermal ablation not only destructs primary tumor but also releases tumor-associated antigens, which promotes maturation of dendritic cells against targeted cancer cells.[117] The followed CTLA-4 blockade *via*

immunotherapy leads to infiltration of effective T cells into distant metastatic cancers, which inhibits the growth of remaining cancer cells.[117] Therefore, the combination treatment of photothermal therapy using MSC-PSAuNP or MSC-AuNP/GO sheet strategy and immunotherapy using anti-CTLA-4, anti-PD-1, or anti-PD-L1 antibody might successfully eliminate the primary tumor and treat the metastatic cancer *via* modulating the adaptive immune responses.

References

1. Zhang, Z.; Wang, J.; Chen, C., Near-Infrared Light-Mediated Nanoplatforms for Cancer Thermo-Chemotherapy and Optical Imaging. *Adv. Mater.* **2013,** *25*, 3869–3880.
2. Jaque, D.; Martinez Maestro, L.; del Rosal, B.; Haro-Gonzalez, P.; Benayas, A.; Plaza, J. L.; Martin Rodriguez, E.; Garcia Sole, J., Nanoparticles for Photothermal Therapies. *Nanoscale* **2014,** *6*, 9494–9530.
3. Weissleder, R., A Clearer Vision for *in Vivo* Imaging. *Nat. Biotechnol.* **2001,** *19*, 316–317.
4. Sapareto, S. A.; Dewey, W. C., Thermal Dose Determination in Cancer Therapy. *Int. J. Radiat. Oncol. Biol. Phys.* **1984,** *10*, 787-800.
5. Hildebrandt, B.; Wust, P.; Ahlers, O.; Dieing, A.; Sreenivasa, G.; Kerner, T.; Felix, R.; Riess, H., The Cellular and Molecular Basis of Hyperthermia. *Crit. Rev. Oncol. Hematol.* **2002,** *43*, 33-56.
6. Burke, A. R.; Singh, R. N.; Carroll, D. L.; Wood, J. C. S.; D'Agostino, R. B.; Ajayan, P. M.; Torti, F. M.; Torti, S. V., The Resistance of Breast Cancer Stem Cells to Conventional Hyperthermia and Their Sensitivity to Nanoparticle-Mediated Photothermal Therapy. *Biomaterials* **2012,** *33*, 2961–2970.
7. Jain, P. K.; Huang, X.; El-Sayed, I. H.; El-Sayed, M. A., Noble Metals on the Nanoscale: Optical and Photothermal Properties and Some Applications in Imaging, Sensing, Biology, and Medicine. *Acc. Chem. Res.* **2008,** *41*, 1578-1586.

8. Wust, P.; Hildebrandt, B.; Sreenivasa, G.; Rau, B.; Gellermann, J.; Riess, H.; Felix, R.; Schlag, P. M., Hyperthermia in Combined Treatment of Cancer. *Lancet Oncol.* **2002,** *3*, 487-497.

9. Choi, J.; Yang, J.; Jang, E.; Suh, J.-S.; Huh, Y.-M.; Lee, K.; Haam, S., Gold Nanostructures as Photothermal Therapy Agent for Cancer. *Anticancer Agents Med. Chem.* **2011,** *11*, 953-964.

10. Huang, X.; Neretina, S.; El-Sayed, M. A., Gold Nanorods: from Synthesis and Properties to Biological and Biomedical Applications. *Adv. Mater.* **2009,** *21*, 4880-4910.

11. Nam, J.; Won, N.; Jin, H.; Chung, H.; Kim, S., pH-Induced Aggregation of Gold Nanoparticles for Photothermal Cancer Therapy. *J. Am. Chem. Soc.* **2009,** *131*, 13639–13645.

12. Pissuwan, D.; Valenzuela, S. M.; Cortie, M. B., Therapeutic Possibilities of Plasmonically Heated Gold Nanoparticles. *Trends Biotechnol.* **2006,** *24*, 62-67.

13. Cobley, C. M.; Chen, J.; Cho, E. C.; Wang, L. V.; Xia, Y., Gold Nanostructures: a Class of Multifunctional Materials for Biomedical Applications. *Chem. Soc. Rev.* **2011,** *40*, 44-56.

14. Ghosh, S. K.; Pal, T., Interparticle Coupling Effect on the Surface Plasmon Resonance of Gold Nanoparticles: from Theory to Applications. *Chem. Rev.* **2007,** *107*, 4797-4862.

15. Su, K. H.; Wei, Q. H.; Zhang, X.; Mock, J. J.; Smith, D. R.; Schultz, S., Interparticle Coupling Effects on Plasmon Resonances of Nanogold Particles. *Nano Letters* **2003,** *3*, 1087-1090.

16. Loo, C.; Lin, A.; Hirsch, L.; Lee, M. H.; Barton, J.; Halas, N.; West, J.; Drezek, R., Nanoshell-Enabled Photonics-Based Imaging and Therapy of Cancer. *Technol. Cancer Res. Treat.* **2004,** *3*, 33–40.

17. Huang, X.; Jain, P. K.; El-Sayed, I. H.; El-Sayed, M. A., Plasmonic Photothermal Therapy (PPTT) Using Gold Nanoparticles. *Lasers Med. Sci.* **2008,** *23*, 217–228.

18. Link, S.; El-Sayed, M. A., Spectral Properties and Relaxation Dynamics of Surface Plasmon Electronic Oscillations in Gold and Silver Nanodots and Nanorods. *J. Phys. Chem. B* **1999,** *103*, 8410–8426.

19. Yu, M. X.; Zheng, J., Clearance Pathways and Tumor Targeting of Imaging Nanoparticles. *ACS Nano* **2015,** *9*, 6655-6674.

20. Liu, J. B.; Yu, M. X.; Zhou, C.; Yang, S. Y.; Ning, X. H.; Zheng, J., Passive Tumor Targeting of Renal-Clearable Luminescent Gold Nanoparticles: Long Tumor Retention and Fast Normal Tissue Clearance. *J. Am. Chem. Soc.* **2013,** *135*, 4978-4981.

21. Choi, H. S.; Liu, W.; Misra, P.; Tanaka, E.; Zimmer, J. P.; Ipe, B. I.; Bawendi, M. G.; Frangioni, J. V., Renal Clearance of Quantum dots. *Nat. Biotechnol.* **2007,** *25*, 1165-1170.

22. Wilhelm, S.; Tavares, A. J.; Dai, Q.; Ohta, S.; Audet, J.; Dvorak, H. F.; Chan, W. C. W., Analysis of Nanoparticle Delivery to Tumours. *Nat. Rev. Mater.* **2016,** *1*.

23. Nagy, J. A.; Chang, S. H.; Shih, S. C.; Dvorak, A. M.; Dvorak, H. F., Heterogeneity of the Tumor Vasculature. *Semin. Thromb. Hemost.* **2010,** *36*, 321-331.

24. Kobayashi, H.; Watanabe, R.; Choyke, P. L., Improving Conventional Enhanced Permeability and Retention (EPR) Effects; What Is the Appropriate Target? *Theranostics* **2014,** *4*, 81-89.

25. Jain, R. K., Molecular Regulation of Vessel Maturation. *Nat. Med.* **2003,** *9*, 685-693.

26. Dreher, M. R.; Liu, W. G.; Michelich, C. R.; Dewhirst, M. W.; Yuan, F.; Chilkoti, A., Tumor Vascular Permeability, Accumulation, and Penetration of Macromolecular Drug Carriers. *J. Natl. Cancer. I.* **2006,** *98*, 335-344.

27. Hobbs, S. K.; Monsky, W. L.; Yuan, F.; Roberts, W. G.; Griffith, L.; Torchilin, V. P.; Jain, R. K., Regulation of Transport Pathways in Tumor Vessels: Role of Tumor Type and Microenvironment. *P. Natl. Acad. Sci. USA* **1998,** *95*, 4607-4612.

28. Byrne, J. D.; Betancourt, T.; Brannon-Peppas, L., Active Targeting Schemes for Nanoparticle Systems in Cancer Therapeutics. *Adv. Drug Deliv. Rev.* **2008,** *60*, 1615-1626.

29. Choi, C. H.; Alabi, C. A.; Webster, P.; Davis, M. E., Mechanism of Active Targeting in Solid Tumors with Transferrin-Containing Gold Nanoparticles. *Proc. Natl. Acad. Sci. USA* **2010,** *107*, 1235-1240.

30. de Menezes, D. E. L.; Pilarski, L. M.; Allen, T. M., In Vitro and *in Vivo* Targeting of Immunoliposomal Doxorubicin to Human B-Cell Lymphoma. *Cancer Res.* **1998,** *58*, 3320-3330.

31. Zhou, Y.; Daryl, C.; Zou, H.; Hayes, M. E.; Adams, G. P.; Kirpotin, D. B.; Marks, J. D., Impact of Single-Chain Fv Antibody Fragment Affinity on Nanoparticle Targeting of Epidermal Growth Factor Receptor-Expressing Tumor Cells. *J. Mol. Biol.* **2007,** *371*, 934-947.

32. Farokhzad, O. C.; Jon, S.; Khademhosseini, A.; Tran, T. N.; Lavan, D. A.; Langer, R., Nanoparticle-Aptamer Bioconjugates: a New Approach for Targeting Prostate Cancer Cells. *Cancer Res.* **2004,** *64*, 7668-7672.

33. Bhattacharya, R.; Patra, C. R.; Earl, A.; Wang, S. F.; Katarya, A.; Lu, L.; Kizhakkedathu, J. N.; Yaszemski, M. J.; Greipp, P. R.; Mukhopadhyay, D.; Mukherjee, P., Attaching Folic Acid on Gold Nanoparticles Using Noncovalent Interaction via Different Polyethylene Glycol Backbones and Targeting of Cancer Cells. *Nanomedicine* **2007,** *3*, 224-238.

34. Montet, X.; Funovics, M.; Montet-Abou, K.; Weissleder, R.; Josephson, L., Multivalent Effects of RGD Peptides Obtained by Nanoparticle Display. *J. Med. Chem.* **2006,** *49*, 6087-6093.

35. Kirpotin, D. B.; Drummond, D. C.; Shao, Y.; Shalaby, M. R.; Hong, K. L.; Nielsen, U. B.; Marks, J. D.; Benz, C. C.; Park, J. W., Antibody Targeting of Long-Circulating Lipidic Nanoparticles Does Not Increase Tumor Localization but Does Increase Internalization in Animal Models. *Cancer Res.* **2006,** *66*, 6732-6740.

36. Hatakeyama, H.; Akita, H.; Ishida, E.; Hashimoto, K.; Kobayashi, H.; Aoki, T.; Yasuda, J.; Obata, K.; Kikuchi, H.; Ishida, T.; Kiwada, H.; Harashima, H., Tumor Targeting of Doxorubicin by Anti-MT1-MMP Antibody-Modified PEG Liposomes. *Int. J. Pharm.* **2007,** *342*, 194-200.

37. Choi, M. R.; Stanton-Maxey, K. J.; Stanley, J. K.; Levin, C. S.; Bardhan, R.; Akin, D.; Badve, S.; Sturgis, J.; Robinson, J. P.; Bashir, R.; Halas, N. J.; Clare, S. E., A Cellular Trojan Horse for Delivery of Therapeutic Nanoparticles into Tumors. *Nano Lett.* **2007,** *7*, 3759-3765.

38. Madsen, S. J.; Baek, S. K.; Makkouk, A. R.; Krasieva, T.; Hirschberg, H., Macrophages as Cell-Based Delivery Systems for Nanoshells in Photothermal Therapy. *Ann. Biomed. Eng.* **2012,** *40*, 507-515.

39. Choi, M. R.; Bardhan, R.; Stanton-Maxey, K. J.; Badve, S.; Nakshatri, H.; Stantz, K. M.; Cao, N.; Halas, N. J.; Clare, S. E., Delivery of Nanoparticles to Brain Metastases of Breast Cancer Using a Cellular Trojan Horse. *Cancer Nanotechnol.* **2012,** *3*, 47-54.

40. Mooney, R.; Roma, L.; Zhao, D.; Van Haute, D.; Garcia, E.; Kim, S. U.; Annala, A. J.; Aboody, K. S.; Berlin, J. M., Neural Stem Cell-Mediated Intratumoral Delivery of Gold Nanorods Improves Photothermal Therapy. *ACS Nano* **2014,** *8*, 12450-12460.

41. Huang, X.; Zhang, F.; Wang, H.; Niu, G.; Choi, K. Y.; Swierczewska, M.; Zhang, G.; Gao, H.; Wang, Z.; Zhu, L.; Choi, H. S.; Lee, S.; Chen, X., Mesenchymal Stem Cell-Based Cell Engineering with Multifunctional Mesoporous Silica Nanoparticles for Tumor Delivery. *Biomaterials* **2013,** *34*, 1772–1780.

42. Dwyer, R. M.; Potter-Beirne, S. M.; Harrington, K. A.; Lowery, A. J.; Hennessy, E.; Murphy, J. M.; Barry, F. P.; O'Brien, T.; Kerin, M. J., Monocyte Chemotactic Protein-1 Secreted by Primary Breast Tumors Stimulates Migration of Mesenchymal Stem Cells. *Clin. Cancer. Res.* **2007,** *13*, 5020-5027.

43. Ringe, J.; Strassburg, S.; Neumann, K.; Endres, M.; Notter, M.; Burmester, G. R.; Kaps, C.; Sittinger, M., Towards in Situ Tissue Repair: Human Mesenchymal Stem Cells Express Chemokine Receptors CXCR1, CXCR2 and CCR2, and Migrate upon Stimulation with CXCL8 but Not CCL2. *J. Cell. Biochem.* **2007,** *101*, 135-146.

44. Ponte, A. L.; Marais, E.; Gallay, N.; Langonne, A.; Delorme, B.; Herault, O.; Charbord, P.; Domenech, J., The *in Vitro* Migration Capacity of Human Bone Marrow Mesenchymal Stem Cells: Comparison of Chemokine and Growth Factor Chemotactic Activities. *Stem Cells* **2007,** *25*, 1737–1745.

45. Fiedler, J.; Roderer, G.; Gunther, K. P.; Brenner, R. E., BMP-2, BMP-4, and PDGF-bb Stimulate Chemotactic Migration of Primary Human Mesenchymal Progenitor Cells. *J. Cell. Biochem.* **2002,** *87*, 305-312.

46. Ball, S. G.; Shuttleworth, C. A.; Kielty, C. M., Vascular Endothelial Growth Factor Can Signal Through Platelet-Derived Growth Factor Receptors. *J. Cell Biol.* **2007,** *177*, 489-500.

47. Kidd, S.; Spaeth, E.; Dembinski, J. L.; Dietrich, M.; Watson, K.; Klopp, A.; Battula, V. L.; Weil, M.; Andreeff, M.; Marini, F. C., Direct Evidence of Mesenchymal Stem Cell Tropism for Tumor and Wounding Microenvironments Using *in Vivo* Bioluminescent Imaging. *Stem Cells* **2009,** *27*, 2614-2623.

48. Studeny, M.; Marini, F. C.; Dembinski, J. L.; Zompetta, C.; Cabreira-Hansen, M.; Bekele, B. N.; Champlin, R. E.; Andreeff, M., Mesenchymal Stem Cells: Potential Precursors for Tumor Stroma and Targeted-Delivery Vehicles for Anticancer Agents. *J. Natl. Cancer Inst.* **2004,** *96*, 1593-1603.

49. Dwyer, R. M.; Kerin, M. J., Mesenchymal Stem Cells and Cancer: Tumor-Specific Delivery Vehicles or Therapeutic Targets? *Hum. Gene Ther.* **2010,** *21*, 1506-1512.

50. Porada, C. D.; Almeida-Porada, G., Mesenchymal Stem Cells as Therapeutics and Vehicles for Gene and Drug Delivery. *Adv. Drug Del. Rev.* **2010,** *62*, 1156-1166.

51. Devine, S. M.; Bartholomew, A. M.; Mahmud, N.; Nelson, M.; Patil, S.; Hardy, W.; Sturgeon, C.; Hewett, T.; Chung, T.; Stock, W.; Sher, D.; Weissman, S.; Ferrer, K.; Mosca, J.; Deans, R.; Moseley, A.; Hoffman, R., Mesenchymal Stem Cells are Capable of Homing to the Bone Marrow of Non-Human Primates Following Systemic Infusion. *Exp. Hematol.* **2001,** *29*, 244-255.

52. Zhang, S.; Gao, H.; Bao, G., Physical Principles of Nanoparticle Cellular Endocytosis. *ACS Nano* **2015,** *9*, 8655-8671.

53. Oh, N.; Park, J. H., Endocytosis and Exocytosis of Nanoparticles in Mammalian Cells. *Int. J. Nanomed.* **2014,** *9*, 51-63.

54. Chithrani, B. D.; Ghazani, A. A.; Chan, W. C. W., Determining the Size and Shape Dependence of Gold Nanoparticle Uptake into Mammalian Cells. *Nano Letters* **2006,** *6*, 662-668.

55. Chithrani, B. D.; Chan, W. C., Elucidating the Mechanism of Cellular Uptake and Removal of Protein-Coated Gold Nanoparticles of Different Sizes and Shapes. *Nano Lett.* **2007,** *7*, 1542–1550.

56. Yue, H.; Wei, W.; Yue, Z. G.; Wang, B.; Luo, N. N.; Gao, Y. J.; Ma, D.; Ma, G. H.; Su, Z. G., The Role of the Lateral Dimension of Graphene Oxide in the Regulation of Cellular Responses. *Biomaterials* **2012,** *33*, 4013-4021.

57. Talukdar, Y.; Rashkow, J. T.; Lalwani, G.; Kanakia, S.; Sitharaman, B., The Effects of Graphene Nanostructures on Mesenchymal Stem Cells. *Biomaterials* **2014,** *35*, 4863–4877.

58. Bae, Y. M.; Park, Y. I.; Nam, S. H.; Kim, J. H.; Lee, K.; Kim, H. M.; Yoo, B.; Choi, J. S.; Lee, K. T.; Hyeon, T.; Suh, Y. D., Endocytosis, Intracellular Transport, and Exocytosis of Lanthanide-Doped

Upconverting Nanoparticles in Single Living Cells. *Biomaterials* **2012,** *33*, 9080-9086.

59. Le Roy, C.; Wrana, J. L., Clathrin- and Non-Clathrin-Mediated Endocytic Regulation of Cell Signalling. *Nat. Rev. Mol. Cell Biol.* **2005,** *6*, 112-126.

60. Young, K. D., The Selective Value of Bacterial Shape. *Microbiol. Mol. Biol. Rev.* **2006,** *70*, 660-703.

61. Geiser, M., Update on Macrophage Clearance of Inhaled Micro- and Nanoparticles. *J. Aerosol. Med. Pulm. Drug Deliv.* **2010,** *23*, 207-217.

62. Park, J.; Kim, B.; Han, J.; Oh, J.; Park, S.; Ryu, S.; Jung, S.; Shin, J. Y.; Lee, B. S.; Hong, B. H.; Choi, D.; Kim, B. S., Graphene Oxide Flakes as a Cellular Adhesive: Prevention of Reactive Oxygen Species Mediated Death of Implanted Cells for Cardiac Repair. *ACS Nano* **2015,** *9*, 4987–4999.

63. Pickett, J. A.; Edwardson, J. M., Compound Exocytosis: Mechanisms and Functional Significance. *Traffic.* **2006,** *7*, 109-116.

64. Serda, R. E.; Mack, A.; van de Ven, A. L.; Ferrati, S.; Dunner, K., Jr.; Godin, B.; Chiappini, C.; Landry, M.; Brousseau, L.; Liu, X.; Bean, A. J.; Ferrari, M., Logic-Embedded Vectors for Intracellular Partitioning, Endosomal Escape, and Exocytosis of Nanoparticles. *Small* **2010,** *6*, 2691-2700.

65. Sakhtianchi, R.; Minchin, R. F.; Lee, K. B.; Alkilany, A. M.; Serpooshan, V.; Mahmoudi, M., Exocytosis of Nanoparticles from Cells: Role in Cellular Retention and Toxicity. *Adv. Colloid Interface Sci.* **2013,** *201-202*, 18-29.

66. Kim, C.; Tonga, G. Y.; Yan, B.; Kim, C. S.; Kim, S. T.; Park, M. H.; Zhu, Z.; Duncan, B.; Creran, B.; Rotello, V. M., Regulating Exocytosis of

Nanoparticles via Host-Guest Chemistry. *Org. Biomol. Chem.* **2015,** *13*, 2474-2479.

67. Kimling, J.; Maier, M.; Okenve, B.; Kotaidis, V.; Ballot, H.; Plech, A., Turkevich Method for Gold Nanoparticle Synthesis Revisited. *J. Phys. Chem. B* **2006,** *110*, 15700-15707.

68. Paik, S. R.; Lee, J. H.; Kim, D. H.; Chang, C. S.; Kim, J., Aluminum-Induced Structural Alterations of the Precursor of the Non-Aβ Component of Alzheimer's Disease Amyloid. *Arch. Biochem. Biophys.* **1997,** *344*, 325–334.

69. Bastus, N. G.; Comenge, J.; Puntes, V., Kinetically Controlled Seeded Growth Synthesis of Citrate-Stabilized Gold Nanoparticles of up to 200 nm: Size Focusing *versus* Ostwald Ripening. *Langmuir* **2011,** *27*, 11098–11105.

70. Hummers, W. S.; Offeman, R. E., Preparation of Graphitic Oxide. *J. Am. Chem. Soc.* **1958,** *80*, 1339–1339.

71. Ishiyama, M.; Miyazono, Y.; Sasamoto, K.; Ohkura, Y.; Ueno, K., A Highly Water-Soluble Disulfonated Tetrazolium Salt as a Chromogenic Indicator for NADH as Well as Cell Viability. *Talanta* **1997,** *44*, 1299-1305.

72. Qiu, Y.; Liu, Y.; Wang, L. M.; Xu, L. G.; Bai, R.; Ji, Y. L.; Wu, X. C.; Zhao, Y. L.; Li, Y. F.; Chen, C. Y., Surface Chemistry and Aspect Ratio Mediated Cellular Uptake of Au Nanorods. *Biomaterials* **2010,** *31*, 7606–7619.

73. Ivascu, A.; Kubbies, M., Rapid Generation of Single-Tumor Spheroids for High-Throughput Cell Function and Toxicity Analysis. *J. Biomol. Screening* **2006,** *11*, 922–932.

74. Euhus, D. M.; Hudd, C.; LaRegina, M. C.; Johnson, F. E., Tumor Measurement in the Nude Mouse. *J. Surg. Oncol.* **1986,** *31*, 229–234.

75. Gobin, A. M.; Lee, M. H.; Halas, N. J.; James, W. D.; Drezek, R. A.; West, J. L., Near-Infrared Resonant Nanoshells for Combined Optical Imaging and Photothermal Cancer Therapy. *Nano Lett.* **2007,** *7*, 1929-1934.

76. von Maltzahn, G.; Park, J. H.; Agrawal, A.; Bandaru, N. K.; Das, S. K.; Sailor, M. J.; Bhatia, S. N., Computationally Guided Photothermal Tumor Therapy Using Long-Circulating Gold Nanorod Antennas. *Cancer Res.* **2009,** *69*, 3892-3900.

77. Ayala-Orozco, C.; Urban, C.; Knight, M. W.; Urban, A. S.; Neumann, O.; Bishnoi, S. W.; Mukherjee, S.; Goodman, A. M.; Charron, H.; Mitchell, T.; Shea, M.; Roy, R.; Nanda, S.; Schiff, R.; Halas, N. J.; Joshi, A., Au Nanomatryoshkas as Efficient Near-Infrared Photothermal Transducers for Cancer Treatment: Benchmarking against Nanoshells. *ACS Nano* **2014,** *8*, 6372-6381.

78. Hiramatsu, H.; Osterloh, F. E., A Simple Large-Scale Synthesis of Nearly Monodisperse Gold and Silver Nanoparticles with Adjustable Sizes and with Exchangeable Surfactants. *Chem. Mater.* **2004,** *16*, 2509-2511.

79. Huotari, J.; Helenius, A., Endosome Maturation. *EMBO J.* **2011,** *30*, 3481-3500.

80. Scott, C. C.; Vacca, F.; Gruenberg, J., Endosome Maturation, Transport and Functions. *Semin. Cell. Dev.Biol.* **2014,** *31*, 2-10.

81. Luzio, J. P.; Pryor, P. R.; Bright, N. A., Lysosomes: Fusion and Function. *Nat. Rev. Mol. Cell Biol.* **2007,** *8*, 622-632.

82. van Weert, A. W.; Dunn, K. W.; Geuze, H. J.; Maxfield, F. R.; Stoorvogel, W., Transport from Late Endosomes to Lysosomes, but Not Sorting of

Integral Membrane Proteins in Endosomes, Depends on the Vacuolar Proton Pump. *J. Cell. Biol.* **1995,** *130*, 821-834.

83. Aniento, F.; Gu, F.; Parton, R. G.; Gruenberg, J., An Endosomal Beta COP Is Involved in the pH-Dependent Formation of Transport Vesicles Destined for Late Endosomes. *J. Cell Biol.* **1996,** *133*, 29-41.

84. Baravalle, G.; Schober, D.; Huber, M.; Bayer, N.; Murphy, R. F.; Fuchs, R., Transferrin Recycling and Dextran Transport to Lysosomes Is Differentially Affected by Bafilomycin, Nocodazole, and Low Temperature. *Cell Tissue Res.* **2005,** *320*, 99-113.

85. Jain, P. K.; Lee, K. S.; El-Sayed, I. H.; El-Sayed, M. A., Calculated Absorption and Scattering Properties of Gold Nanoparticles of Different Size, Shape, and Composition: Applications in Biological Imaging and Biomedicine. *J. Phys. Chem. B* **2006,** *110*, 7238-7248.

86. Govorov, A. O.; Richardson, H. H., Generating Heat with Metal Nanoparticles. *Nano Today* **2007,** *2*, 30-38.

87. Schaeublin, N. M.; Braydich-Stolle, L. K.; Schrand, A. M.; Miller, J. M.; Hutchison, J.; Schlager, J. J.; Hussain, S. M., Surface Charge of Gold Nanoparticles Mediates Mechanism of Toxicity. *Nanoscale* **2011,** *3*, 410–420.

88. Nam, J.; La, W. G.; Hwang, S.; Ha, Y. S.; Park, N.; Won, N.; Jung, S.; Bhang, S. H.; Ma, Y. J.; Cho, Y. M.; Jin, M.; Han, J.; Shin, J. Y.; Wang, E. K.; Kim, S. G.; Cho, S. H.; Yoo, J.; Kim, B. S.; Kim, S., pH-Responsive Assembly of Gold Nanoparticles and "Spatiotemporally Concerted" Drug Release for Synergistic Cancer Therapy. *ACS Nano* **2013,** *7*, 3388-3402.

89. Wang, Y. C.; Black, K. C. L.; Luehmann, H.; Li, W. Y.; Zhang, Y.; Cai, X.; Wan, D. H.; Liu, S. Y.; Li, M.; Kim, P.; Li, Z. Y.; Wang, L. H. V.; Liu,

Y. J.; Xia, Y. A., Comparison Study of Gold Nanohexapods, Nanorods, and Nanocages for Photothermal Cancer Treatment. *ACS Nano* **2013,** *7*, 2068-2077.

90. Panariti, A.; Miserocchi, G.; Rivolta, I., The Effect of Nanoparticle Uptake on Cellular Behavior: Disrupting or Enabling Functions? *Nanotechnol. Sci. Appl.* **2012,** *5*, 87-100.

91. Hong, I. S.; Lee, H. Y.; Kang, K. S., Mesenchymal Stem Cells and Cancer: Friends or Enemies? *Mutat. Res.-Fundam. Mol. Mech. Mutag.* **2014,** *768*, 98-106.

92. Ho, I. A. W.; Toh, H. C.; Ng, W. H.; Teo, Y. L.; Guo, C. M.; Hui, K. M.; Lam, P. Y. P., Human Bone Marrow-Derived Mesenchymal Stem Cells Suppress Human Glioma Growth Through Inhibition of Angiogenesis. *Stem Cells* **2013,** *31*, 146-155.

93. Lu, Y. R.; Yuan, Y.; Wang, X. J.; Wei, L. L.; Chen, Y. N.; Cong, C.; Li, S. F.; Long, D.; Tan, W. D.; Mao, Y. Q.; Zhang, J.; Li, Y. P.; Cheng, J. Q., The Growth Inhibitory Effect of Mesenchymal Stem Cells on Tumor Cells *in Vitro* and *in Vivo*. *Cancer Biol. Ther.* **2008,** *7*, 245-251.

94. Xu, W. T.; Bian, Z. Y.; Fan, Q. M.; Li, G.; Tang, T. T., Human Mesenchymal Stem Cells (hMSCs) Target Osteosarcoma and Promote its Growth and Pulmonary Metastasis. *Cancer Lett.* **2009,** *281*, 32-41.

95. Zhu, W.; Xu, W. R.; Jiang, R. Q.; Qian, H.; Chen, M.; Hu, J. B.; Cao, W. K.; Han, C. X.; Chen, Y. C., Mesenchymal Stem Cells Derived from Bone Marrow Favor Tumor Cell Growth *in Vivo*. *Exp. Mol. Pathol.* **2006,** *80*, 267-274.

96. Wang, C.; Xu, L. G.; Liang, C.; Xiang, J.; Peng, R.; Liu, Z., Immunological Responses Triggered by Photothermal Therapy with

Carbon Nanotubes in Combination with Anti-CTLA-4 Therapy to Inhibit Cancer Metastasis. *Adv. Mater.* **2014,** *26*, 8154-8162.

97. Basel, M. T.; Balivada, S.; Wang, H. W.; Shrestha, T. B.; Seo, G. M.; Pyle, M.; Abayaweera, G.; Dani, R.; Koper, O. B.; Tamura, M.; Chikan, V.; Bossmann, S. H.; Troyer, D. L., Cell-Delivered Magnetic Nanoparticles Caused Hyperthermia-Mediated Increased Survival in a Murine Pancreatic Cancer Model. *Int. J. Nanomed.* **2012,** *7*, 297–306.

98. Kang, S.; Bhang, S. H.; Hwang, S.; Yoon, J. K.; Song, J.; Jang, H. K.; Kim, S.; Kim, B. S., Mesenchymal Stem Cells Aggregate and Deliver Gold Nanoparticles to Tumors for Photothermal Therapy. *ACS Nano* **2015,** *9*, 9678–9690.

99. Sabella, S.; Carney, R. P.; Brunetti, V.; Malvindi, M. A.; Al-Juffali, N.; Vecchio, G.; Janes, S. M.; Bakr, O. M.; Cingolani, R.; Stellacci, F.; Pompa, P. P., A General Mechanism for Intracellular Toxicity of Metal-Containing Nanoparticles. *Nanoscale* **2014,** *6*, 7052–7061.

100. Tang, F. Q.; Li, L. L.; Chen, D., Mesoporous Silica Nanoparticles: Synthesis, Biocompatibility and Drug Delivery. *Adv. Mater.* **2012,** *24*, 1504–1534.

101. Goedert, M., Alpha-Synuclein and Neurodegenerative Diseases. *Nat. Rev. Neurosci.* **2001,** *2*, 492–501.

102. Lee, J.; Bhak, G.; Lee, J. H.; Park, W.; Lee, M.; Lee, D.; Jeon, N. L.; Jeong, D. H.; Char, K.; Paik, S. R., Free-Standing Gold-Nanoparticle Monolayer Film Fabricated by Protein Self-Assembly of α-Synuclein. *Angew. Chem. Int. Ed.* **2015,** *54*, 4571–4576.

103. Lee, W. C.; Lim, C. H.; Shi, H.; Tang, L. A.; Wang, Y.; Lim, C. T.; Loh, K. P., Origin of Enhanced Stem Cell Growth and Differentiation on Graphene and Graphene Oxide. *ACS Nano* **2011,** *5*, 7334–7341.

104. Shi, X. T.; Chang, H. X.; Chen, S.; Lai, C.; Khademhosseini, A.; Wu, H. K., Regulating Cellular Behavior on Few-Layer Reduced Graphene Oxide Films with Well-Controlled Reduction States. *Adv. Funct. Mater.* **2012,** *22*, 751–759.

105. Moussa, S. A., G.; El-Shall, M. S.; Shehata, A.; AbouZeid, K. M.; Mohamed, M. B., Laser Assisted Photocatalytic Reduction of Metal Ions by Graphene Oxide. *J. Mater. Chem.* **2011,** *21*, 9608 - 9619.

106. Zedan, A. F. M., S.; Terner, J.; Atkinson, G.; El-Shall, M. S., Ultrasamll Gold Nanoparticles Anchored to Graphene and Enhanced Photothermal Effects by Laser Irradiation of Gold Nanostructures in Graphene Oxides Solutions. *ACS Nano* **2013,** *7*, 627 - 636.

107. Kim, C. H.; Bhak, G.; Lee, J.; Sung, S.; Park, S.; Paik, S. R.; Yoon, M. H., Controlled Charge Trapping and Retention in Large-Area Monodisperse Protein Metal-Nanoparticle Conjugates. *ACS Appl. Mater. Interfaces* **2016,** *8*, 11898–11903.

108. Ghosh, S. K.; Pal, T., Interparticle Coupling Effect on the Surface Plasmon Resonance of Gold Nanoparticles: from Theory to Applications. *Chem. Rev.* **2007,** *107*, 4797-862.

109. Turitto, V. T., Blood-Viscosity, Mass-Transport, and Thrombogenesis. *Prog. Hemost. Thromb.* **1982,** *6*, 139–177.

110. Hynes, R. O., Integrins: Versatility, Modulation, and Signaling in Cell Adhesion. *Cell* **1992,** *69*, 11–25.

111. Han, X.; Gelein, R.; Corson, N.; Wade-Mercer, P.; Jiang, J.; Biswas, P.; Finkelstein, J. N.; Elder, A.; Oberdorster, G., Validation of an LDH Assay for Assessing Nanoparticle Toxicity. *Toxicology* **2011,** *287*, 99-104.

112. Kucia, M.; Reca, R.; Miekus, K.; Wanzeck, J.; Wojakowski, W.; Janowska-Wieczorek, A.; Ratajczak, J.; Ratajczak, M. Z., Trafficking of Normal Stem Cells and Metastasis of Cancer Stem Cells Involve Similar Mechanisms: Pivotal Role of the SDF-1-CXCR4 Axis. *Stem Cells* **2005,** *23*, 879–894.

113. Zhang, G. D.; Yang, Z.; Lu, W.; Zhang, R.; Huang, Q.; Tian, M.; Li, L.; Liang, D.; Li, C., Influence of Anchoring Ligands and Particle Size on the Colloidal Stability and *in Vivo* Biodistribution of Polyethylene Glycol-Coated Gold Nanoparticles in Tumor-Xenografted Mice. *Biomaterials* **2009,** *30*, 1928–1936.

114. Arnida; Janat-Amsbury, M. M.; Ray, A.; Peterson, C. M.; Ghandehari, H., Geometry and Surface Characteristics of Gold Nanoparticles Influence Their Biodistribution and Uptake by Macrophages. *Eur. J. Pharm. Biopharm.* **2011,** *77*, 417–423.

115. Wang, K.; Ruan, J.; Song, H.; Zhang, J.; Wo, Y.; Guo, S.; Cui, D., Biocompatibility of Graphene Oxide. *Nanoscale Res. Lett.* **2010,** *6*, 8.

116. Chen, F.; Cai, W., Nanomedicine for Targeted Photothermal Cancer Therapy: Where Are We Now? *Nanomedicine* **2015,** *10*, 1-3.

117. Wang, C.; Xu, L.; Liang, C.; Xiang, J.; Peng, R.; Liu, Z., Immunological Responses Triggered by Photothermal Therapy with Carbon Nanotubes in Combination with Anti-CTLA-4 Therapy to Inhibit Cancer Metastasis. *Adv. Mater.* **2014,** *26*, 8154-8162.

요약(국문초록)

암은 주요한 건강 문제이며, 전 세계적으로 사망의 주된 원인으로 꼽힌다. 나노 기술이 주목할 만한 진보를 보임에 따라 나노입자 기반의 암 치료법이 광범위하게 연구되고 있다. 최근, 암 치료를 위한 새로운 전략으로 광열 요법이 등장했다. 여러 광열 요원들 중에서 금 나노입자는 근적외선 레이저를 조사를 조사하였을 때 높은 광 – 열 변환 효율을 나타내기 때문에 광열 암 치료를 위한 연구에 많은 주목을 받고 있다. 그러나 금 나노입자의 현저히 낮은 종양 표적화 효율을 개선하는 것에는 여전히 어려움이 있다. 이에 따라, 본 연구에서는 금 나노입자를 암 조직으로 전달하는 운반체로서 종양 주성을 가진 중간엽 줄기세포를 응용한 효과적인 광열 암 치료법을 제시한다.

먼저, 제 3 장에서는 산성도 감응성 금 나노입자를 중간엽 줄기세포에 내재시켜 암 조직으로 전달하는 연구를 진행하였다. 종양 주성을 가진 중간엽 줄기세포는 세포 내 약산성 환경인 엔도좀에서 산성도 감응성 금 나노입자를 응집시키고, 스스로 암 조직으로 이동하며, 광열 치료에 응용될 수 있다. 세포를 매개로 한 물질 전달 과정에서 세포 내에 얼마나 많은 물질을 담을 수 있는가가 매우 중요한데, 응집된 산성도 감응성 금 나노입자는 세포 외 유출 현상을 억제함으로써 산성도에 반응하지 않는 개별의 금 나노입자에 비해 높은 세포 내 함량을 보였다. 종양이 유도된 마우스에 산성도 감응성 금 나노입자를 함유한 중간엽 줄기세포를 정맥 주사하였더니, 산성도 비감응성 금

나노입자를 정맥 주사한 것에 비해 종양 표적 효율이 증가하였고, 레이저를 조사하였을 때 발열량이 증가하였으며, 이로써 매우 향상된 항암 효과를 확인할 수 있었다.

제 4 장에서는 금 나노입자와 그래핀옥사이드로 구성된 하이브리드 시트를 중간엽 줄기세포의 표면에 부착하여 종양 조직으로 전달하는 연구를 하였다. 세포 내로 전달된 나노입자는 세포 독성을 일으키고 세포 외 유출을 통해 세포 밖으로 빠져 나가기 때문에 나노입자를 세포 내에 담지하여 전달하는 데에는 한계가 있다. 따라서 본 연구에서는 세포 표면에 안정적으로 부착하고 뛰어난 광열 효과를 보이는 금 나노입자/그래핀옥사이드 시트를 도입하였다. 두 개의 금 나노입자 단일층 사이에 그래핀옥사이드가 끼어있는 삼중층 구조의 금 나노입자/그래핀옥사이드 시트를 형성하기 위해, 금 나노입자를 알파시누클레인 단백질로 코팅한 후 그래핀옥사이드 시트에 흡착시켰다. 종양 주성을 가진 중간엽 줄기세포에 금 나노입자/그래핀옥사이드 시트를 부착시키는 전략은 세포 독성과 세포 외 유출이라는 문제를 피함으로써 세포에 금 나노입자를 담지하는 효율을 향상시켰다. 또한, 마이크로 크기의 그래핀옥사이드 시트 상에 금 나노입자를 조밀하게 흡착시킴으로써 금 나노입자 간의 강한 플라즈몬 결합 현상을 일으키게 하여 광열 효과를 증가시켰다. 종양이 유도된 마우스에 금 나노입자/그래핀옥사이드 시트를 부착한 중간엽 줄기세포를 정맥 주사하였더니, 종양 조직으로 전달되는 금 나노입자의 양이 증가하고 레이저 조사 시 높은 열이 발생하여 광열 암 치료의 효능이 크게 향상되었다.

세포 기반의 트로이 목마 전략은 항암제를 암 조직으로 전달하는 효과적인 플랫폼이 될 수 있다. 뿐만 아니라, 물질과 세포 사이의 상호작용을 이용하여 치료 효과를 극대화 할 수 있다. 이러한 물질 또는 세포 기반의 항암 요법은 성공적인 암 치료를 위해 사용될 수 있을 것이다.

주요어: 광열 치료, 금 나노입자, 종양 주성, 종양 표적화, 중간엽 줄기세포

학 번: 2014-30251